Chaotic Advection by Submesoscale Processes in the Ocean

Dissertation

with the aim of achieving a doctoral degree
at the Faculty of Mathematics, Informatics and Natural Sciences
Department of Earth Sciences
University of Hamburg

submitted by

Daniel Mukiibi
from Ndeeba, Uganda

Hamburg
July, 2016.

Day of oral defense: 6^{th} July, 2016.

The following evaluators recommend the admission of the dissertation:
Prof. Dr. Gualtiero Badin
Dr. Nuno Serra

Abstract

Oceanic motions at spatial scales of $\mathcal{O}(100)$ km and above, are quasi-two dimensional (2D) while dynamics at scales of $\mathcal{O}(1)$ km - also called submesoscale, are known to be quasi-three dimensional (3D). Stirring processes at the submesoscale therefore require a 3D treatment, which is considered in this thesis. A comparison of 3D and 2D Lagrangian flow diagnostics - the Finite Time Lyapunov Exponents (FTLEs) is made. 3D FTLEs are computed from numerical simulations of a freely evolving oceanic mixed layer (ML) front in a zonal channel undergoing baroclinic instability. The 3D FTLEs show a complex structure, with features that are less defined than the 2D FTLEs, suggesting that stirring is not confined to the edges of vortices and along filaments, thus posing significant consequences on mixing. The magnitude of 3D FTLEs is found to be strongly determined by the vertical shear. Maximising curves of FTLEs, also called Lagrangian Coherent Structures (LCSs), are found to successfully detect submesoscale filaments and vortices in locations where the Eulerian diagnostics are featureless.

A scaling law relating the local FTLEs and the nonlocal density contrast used to initialize the ML front is derived assuming thermal wind balance. The derived scaling law converges to the values found from the simulations within the pycnocline, while it diverges from it in the ML where the instabilities show a large ageostrophic component. Also, probability distribution functions (PDFs) of 2D and 3D FTLEs are found to be non Gaussian at all depths of the channel. The non-Gaussianity of these PDFs suggests that parameterization schemes in existing numerical models should be improved.

Finally, the same analysis as for the idealised simulations, is repeated with a realistic ocean simulation dataset in two case study regions of the Atlantic Ocean in order to understand the influence of the various ocean forcing sources on the FTLEs, and to also investigate the seasonal cycle of 2D and 3D FTLEs. It is found that FTLEs show a clear seasonal cycle with large values in winter and low values in summer. The seasonal cycle of 2D FTLEs is found to be modulated by the eddy kinetic energy (EKE) both at the surface and ocean interior. At the ocean surface, 3D FTLEs are modulated by the vertical shear of horizontal velocities, which shows minimal change between winter and summer, while in the ocean interior, 3D FTLEs yield the same seasonal behaviour as 2D FTLEs. However, the primary determinant of the seasonal cycle of FTLEs is found to be the deepening of the mixed layer in winter, which leads to the increase of available potential energy on which baroclinic instabilities draw.

Zusammenfassung

Strömungen im Ozean mit Gröflenordnungen von über $\mathcal{O}(100)$ km sind quasi zweidimensional (2D) während Strömungen auf Skalen von $\mathcal{O}(1)$ km, auch Submesoskalen genannt, als dreidimensional (3D) anzusehen sind. Submesoskalige Durchmischungsprozesse werden daher in dieser Arbeit als 3D Prozesse betrachtet. Es wird der Vergleich von 3D und 2D lagrangeschen Flüssen - den endlichen zeitlichen Lyapunov Exponenten (FTLEs) durchgeführt. Die 3D FTLEs werden aus numerischen Simulationen einer sich frei entwickelnden Front einer Mischschicht (ML) in einem zonalen Kanals mit barokliner Instabilität berechnet. Die 3D FTLEs haben eine komplexe Struktur, mit weniger definierten Eigenschaften als bei den 2D FTLEs, was darauf hindeutet, dass Vermischungsprozesse nicht auf die Ränder von Wirbeln und entlang von Filamenten beschränkt sind. Dies wiederum hat einen entscheidenden Einfluß auf die Vermischung. Die Größe der 3D FTLEs wird dabei stark von der vertikalen Scherung bestimmt. Mit Hilfe der Maximierungskurven der FTLEs, die auch lagrangesche kohärente Strukturen (LCSs) genannt werden, können submesoskalige Filamente und Wirbel auch in den Regionen gefunden werden in denen eulersche Diagnosen ergebnislos bleiben.

Unter der Annahme der thermalen Windbalance wird ein Skalierungsgesetz abgeleitet, das die lokalen FTLEs und die nichtlokalen Dichtekontraste in Beziehung setzt um die ML-Front zu initialisieren. Das abgeleitete Skalierungsgesetz konvergiert zu den Werten aus Simulationen in der Pyknokline, während es sich in der ML davon entfernt, in welcher die Instabilitäten eine große ageostrophische Komponente haben. Zudem zeigt sich, dass die Wahrscheinlichkeitsverteilungsfunktionen (PDFs) von 2D und 3D FTLEs in keiner Tiefe gaussverteilt sind. Die Nicht-Gaussverteilung der PDFs legt nahe die Parametrisierungsschemata für passive tracer, wie sie in existierenden numerischen Modellen verwendet werden, zu verbessern.

Schließlich werden die gleichen Analysen wie für die idealisierten Simulationen für Datensätze von realistischen Ozean-Simulationen zweier Beispielregionen im Atlantik wiederholt, um den Einfluß verschiedener Antriebe auf die FTLEs zu verstehen, und um im weiteren den Jahresgang der 2D und 3D FTLEs zu untersuchen. Die FTLEs zeigen einen klaren Jahresgang mit großen Werten im Winter die zum Sommer hin abnehmen. Faktoren wie Schichtung (z.B. indirekt durch Auftrieb) und wirbelkinetische Energie tragen zur Modulation des Jahresganges der FTLEs sowohl an der Oberfläche als auch in tieferen Schichten des Ozeans bei. Die Hauptursache für den Jahresgang der FTLEs ist jedoch die Vertiefung der ML im Winter, die zu einem Anstieg der verfügbaren potentiellen Energie führt, von der barokline Instabilitäten zähren.

Contents

List of Figures

List of Tables

Chapter 1

Introduction

Observations (e.g. Shcherbina et al., 2015, and references therein) and high resolution numerical modeling studies (e.g. Thomas et al. (2008) and references therein) reveal the presence of a wide variety of ocean dynamical processes at scales smaller than the deformation radius, which have been referred to as submesoscale dynamics. Dynamics in this regime are characterized by Rossby ($\mathrm{R_o}$) and bulk Richardson ($\mathrm{R_i}$) numbers of $\mathcal{O}(1)$ (Thomas et al., 2008), differing thus from dynamics at mesoscale and large scales, where $\mathrm{R_o} << 1$ and $\mathrm{R_i} >> 1$.

One of the sources of submesoscale variability is given by mixed layer instabilities (MLIs) (Boccaletti et al., 2007; Fox-Kemper et al., 2008). Mixed layer (ML) fronts can be created, for example, by the passage of storms which leave areas of the ocean locally mixed (Price, 1981; Ferrari and Rudnick, 2000), by tidal mixing in the coastal regions (Badin et al., 2009) and in upwelling regions where deeper, colder waters are brought to the surface (Calil and Richards, 2010; Bettencourt et al., 2012). ML fronts are dynamically unstable: after an initial geostrophic adjustment (Tandon and Garrett, 1994, 1995; Young, 1994), they undergo baroclinic instability, yielding ageostrophic MLIs with growth rates of the order of days (Haine and Marshall, 1998; Molemaker and McWilliams, 2005) and leading to ML restratification (Boccaletti et al., 2007; Fox-Kemper and Ferrari, 2008). The restratification of the surface ocean may be further affected by other forms of instabilities such as symmetric instabilities (Haine and Marshall, 1998; Taylor and Ferrari, 2009), while other dynamical factors like down-front wind stress have been found to slow down the restratification-mixing cycle of the upper ocean (Mahadevan et al., 2010). MLIs lead to the emergence of filamentary features. These filaments can create a form of nonlocal turbulence, in which the small scale motions are controlled by the large scale dynamics (e.g., Badin, 2014; Gula et al., 2014). Otherwise, the filaments can be formed by local frontogenesis, which takes the shape of elongated features (e.g., Mensa et al., 2013; Ragone and Badin, 2016). The filaments are characterized by intensified relative vorticity, vertical velocity and strain rate (Mahadevan, 2006; Thomas et al., 2008). The filaments further undergo secondary instabilities (e.g. Thomas et al. (2008); Gula et al. (2014)). The intensification of vertical velocities at submesocale has important effects on the budgets of buoyancy, mass and other tracers, for example facilitating the supply of nutrients and gases to the euphotic layers of the ocean thereby enhancing primary production in the ocean interior (Lévy et al., 2001).

Frontal dynamics can be important also for the transformation of water masses (Thomas and Joyce, 2010; Badin et al., 2010, 2013; Thomas et al., 2013a). Further, MLIs might be able to penetrate in the underlying pycnocline where they might be important for the lateral mixing of tracers (Badin et al., 2011).

The traditional techniques used in the definition and identification of coherent structures make use of Eulerian fields, defining them as localized, persisting regions with values of relative vorticity or strain rate larger than their surroundings (e.g., Calil and Richards, 2010). An alternative definition makes use of the Okubo-Weiss (OW) parameter, defined as the difference between the square of relative vorticity and horizontal strain (Okubo, 1970; Weiss, 1991). While the OW parameter sometimes correctly identifies coherent vortices (Boffetta et al., 2001; Harrison and Glatzmaier, 2012), and a strong correlation has been found to exist between zero level contours of the OW parameter and Lagrangian Coherent Structures (LCSs) (d'Ovidio et al., 2009), this technique is also observed to yield boundaries of vortices that are an underestimation of the actual sizes of the vortices (Haller and Yuan, 2000; Harrison and Glatzmaier, 2012). Further, and perhaps more seriously, the OW parameter is not an objective method to assess the flow coherence as it depends on the frame of reference in which the observations are made, and leads thus to an observer dependent assessment of flow coherency (Beron-Vera et al., 2013; Haller, 2015). In the current study, the OW parameter presents a further problem that is characteristic of ageostrophic instabilities: as stated previously, filamentary MLIs are characterized by intensified relative vorticity and strain rate in the same location, making the OW parameter are ill defined quantity.

Given these issues in studying chaotic stirring and in identifying the structures responsible for this stirring, in the current study, we concentrate on the Lagrangian approach to study the chaotic advection emerging from the MLIs using Finite Time Lyapunov exponents.

Lyapunov exponents are defined in the asymptotic limit of infinite time intervals which renders them inapplicable to geophysical situations where velocity fields are only known for finite time intervals. As an alternative, Lyapunov exponents can be calculated for finite intervals of time, leading to the concept of Finite Time Lyapunov Exponents (FTLEs) (Haller and Yuan, 2000; Haller, 2001; Shadden et al., 2005). Differently from Lyapunov exponents defined on a strange attractor, FTLEs are not a global dynamical property of the flow and thus depend on the initial conditions of the calculated trajectories, i.e. on the initial position and on the initial time of release of the particles. This apparent limitation results however in the property of FTLEs being able to capture local features of the flow, such as hyperbolic regions and stirring/adiabatic mixing barriers (Lapeyre, 2002; Wiggins, 2005). Because the Lyapunov exponents define lines of exponential separation of particles (e.g. passive tracers), they become an important measure for the stirring and dispersive properties of the flow. The tendency of the flow to fill the chaotic region results in a nonlocal form of turbulence, suggesting that these features might provide the correct representation for submesoscale turbulence. The theory assumes that the velocity field prescribed by the flow is already known in form of analytic functions (e.g., Haller, 2001, 2002; Shadden et al., 2005; Lekien et al., 2007; Sulman et al., 2013), numerical simulations (e.g., Rypina et al., 2007; Rypina and Pratt, 2010; Bettencourt et al., 2012) or observation data taken by satellites (Beron-Vera et al., 2008; Waugh and Abraham, 2008; Waugh et al., 2012; Harrison and Glatzmaier, 2012).

A closely related diagnostic of stirring is the Finite Size Lyapunov Exponent (FSLE). In the FSLE technique, the time τ it takes a pair of particles initially separated by a distance δ_i, to increase their separation to a distance δ_f is calculated (e.g., Artale et al., 1997; Aurell et al., 1997). If the final particle separation after time τ does not reach a predefined threshold γ, also called the amplification factor (e.g., d'Ovidio et al., 2004, 2009), the FSLE is assigned a value of zero in that location. The possibility of fine tuning the amplification factor γ, allows the application of FSLEs in the study of phenomenon over a broad range of spatial scales, ranging from mesoscales (e.g., Bettencourt et al., 2012, 2013) to large scale oceanic (Hernández-Carrasco et al., 2011; Hernández-Carrasco et al., 2012) and planetary (Joseph and Legras, 2002) motions. Further, Farnetani and Samuel (2003) have used FSLEs to study the deformation induced by the mantle flow at a subduction zone in the Earth's interior.

In a comparison between FTLEs and FSLEs, Boffetta et al. (2001) report that no one particular diagnostic is superior to the other but each is superior in representing flows under specific conditions. FSLEs are reported to reveal large scale structures better than FTLEs. The FTLEs are instead more suited for revealing small scale properties of chaotic advection in the atmosphere. They also report that Eulerian techniques like Okubo-Weiss parameter and its improvement, the Hua - Klein criterion, are insensitive to small scale transport barriers. In another study, Farnetani and Samuel (2003) report that FTLEs are superior to FSLEs in detecting deformations around a subduction zone induced by the mantle flow in the Earth's interior. More recently, in a study involving analytic and ocean velocity fields, Peikert et al. (2014) report that when the amplification factor is suitably selected, FSLEs and FTLEs are equivalent and thus yield similar results.

In addition to being used as diagnostics for quantifying stirring effected by a given flow, FTLEs and FSLEs have also been used to locate structures akin to stable and unstable manifolds of a classic dynamic system. These structures have been referrred to as Lagrangian Coherent Structures by Haller and Yuan (2000). Initally, LCSs were calculated as local maxima of FTLE fields (e.g., Haller, 2001; Shadden et al., 2005) yielding curves in 2D and/or surfaces in 3D flows (e.g., Lekien et al., 2007) with zero flux across them, thus representing barriers to mixing. Olascoaga et al. (2006) report a persistent transport barrier on the shelf of West Florida which is coincident with the FTLE ridge computed for the same flow. However, a close inspection of ridges of FTLEs showed that they sometimes yield LCSs where they do not exist (false positives) and fail to yield LCSs in locations where they are known to exist (e.g., Haller, 2011). The calculation of LCSs has thus since digressed from the consideration of FTLE ridges to the variational theory, in which LCSs are defined as explicitly parameterized material curves advected by the flow (e.g., Haller, 2011; Haller and Beron-Vera, 2012; Beron-Vera et al., 2013; Farazmand et al., 2014) and

(Haller, 2015, for a review). The variational theory has the advantage of unveiling both elliptic (e.g., vortices) and hyperbolic (e.g., filaments) LCSs, unlike the ridge based definition that emphasized only hyperbolic LCSs.

The material nature of LCSs means that they constrain the flow thereby effectively controlling the fluid motion, and hence their identification is of immense importance in understanding the transport and evolution of tracers in geophysical flows. Knowledge of location of LCSs, is thus important in understanding the dispersion patterns of tracers like pollutants as they form the template for tracer dispersion (e.g., Olascoaga and Haller, 2012; Beron-Vera, 2015). The intensity of FTLEs and FSLEs can be used to quantify the amount of stirring effected by a given flow field and time series of Eulerian diagnostics like eddy kinetic energy (EKE) and vorticity from which the strength of a flow can be inferred, have been found to show seasonal cycles similar to those of FTLEs and FSLEs (e.g., d'Ovidio et al., 2004; Waugh and Abraham, 2008; Hernández-Carrasco et al., 2012). Sasaki et al. (2014) have found that submesoscale dynamics in the North Atlantic show a clear seasonal cycle which is largely determined by frontal instabilities. These frontal instabilities are mainly of two types: 1) baroclinic MLIs which are dominant in winter when the ML is deep and are characterized by the enhancement of the conversion of available potential energy (APE) to kinetic energy (e.g., Boccaletti et al., 2007). 2) Symmetric instabilities which emerge when the Ertel potential vorticity becomes negative (e.g., Hoskins et al., 1978; Thomas et al., 2013b). In a more recent realistic ocean modelling study, Mensa et al. (2013) report that the seasonal cycle of submesoscale turbulence in the Gulf Stream is dominated entirely by MLIs, showing a higher intensity in winter and a weakening in summer. In this thesis, we take keen interest in investigating the seasonality of submesoscale turbulence using Lagrangian diagnostics, specifically the FTLEs. A comparison between time series of 3D and 2D FTLEs will be made and the factors that modulate their seasonal cycles will be explored.

1.1 Research questions

Few studies have considered three dimensional FTLEs for geophysical flows due to the fact that such flows are predominantly two dimensional. Among the exceptions is the study by Sulman et al. (2013), who considered the FTLEs and the resulting LCSs emerging from analytic 3D velocity fields. Their results show that appropriate approximations of 3D FTLEs should account for the vertical shear of horizontal velocities. In this thesis, we consider a more geophysically relevant flow obtained from the instability of a ML front, in which the dynamics are dominated by the presence of stratification and rotation. The resulting instabilities are characterized by enhanced vertical velocities and vertical shear. We will thus focus on the following questions:

- What is the chaotic stirring resulting from MLIs?
- What is the role of vertical velocities and vertical shear in determining the structure and magnitude of FTLEs?
- What are the differences between 3D and 2D FTLEs for MLIs?

- How does the skeleton of MLIs turbulence, responsible for the chaotic stirring, look like?
- How do our findings from the idealised setting of a ML front relate to a more realistic setting in which noise induced by surface winds and/or internal waves are likely to change the flow dynamics?
- Is it possible to characterize the seasonality of submesoscale turbulence of a realistically forced simulation using FTLEs?
- And finally, what are the differences between the seasonal cycles of 2D and 3D FTLEs?

1.2 Research objectives

The objective of this thesis is to use a Lagrangian approach to study the chaotic advection effected by baroclinic ML instabilities, arising from an adjusting ML front in an idealised setting. This is done by calculating FTLEs whose statistics are used to characterize the stirring influence of these instabilities.

The thesis also aims at extending the calculation of FTLEs in an oceanographic context, from considering 2D surfaces yielding a quasi-3D structure (e.g., Bettencourt et al. 2012, 2013 using FSLEs and, Garaboa-Paz et al. 2015 using FTLEs in the atmosphere) to a fully 3D structure and make a comparison with the 2D FTLEs which have been previously considered (e.g., Beron-Vera et al., 2008; Beron-Vera and Olascoaga, 2009; Prants, 2014). A comparison 3D and 2D FTLEs will also be made.

Further, an understanding of the vertical structure of the chaotic advection is sought in order to establish if ML turbulence eventually has an impact on the underlying pycnocline and hence the lateral stirring of tracers there. Badin et al. (2011) have previously found that MLIs may propagate into the ocean interior and influence the dispersion of tracers in the pycnocline.

The study also seeks to establish if MLIs can be detected as Lagrangian coherent structures thus overcoming the shortcomings of Eulerian diagnostics which are unable to correctly characterize submesoscale filaments.

Finally, we seek to understand the extent to which the findings of the idealised study are translated to a realistic ocean setting, datasets of two case study regions in the Atlantic Ocean are considered and the same analysis done in the idealised simulations is repeated. The datasets obtained are from a realistically forced simulation of the Atlantic Ocean and thus allow to study the seasonality of the submesoscale turbulence and the factors which characterize it.

1.3 Thesis Outline

From hereon, the thesis will be arranged as follows:

In Chapter 2, the theoretical background of chaotic advection is described. In particular, Sections 2.2 and 2.3 respectively outline how FTLEs and FSLEs can be numerically calculated given a Eulerian velocity field $\mathbf{u}(\boldsymbol{x}, t)$. Section 2.4 discusses the process of obtaining LCSs using the theory of geodesics which enables a systematic rendering of coherent structures by yielding elliptic (e.g., closed vortices) and hyperbolic (e.g., filaments) LCSs as explicitly parametrized curves.

In Chapter 3, a description of the numerical model used in the idealised study is given, with Subsection 3.1.1 outlining the boundary conditions and geometrical layout of the channel used. The initial conditions for the ML front are specified in Subsection 3.1.2. An outline of the model parameters used in the idealised simulations is also given. Section 3.2, describes the methodology of integrating particle trajectories and calculating FTLEs and FSLEs. In particular, Section 3.2.1 describes the numerical algorithm used to integrate particle trajectories and the numerical computation of FTLEs using the particle trajectories is given in Section 3.2.2. A detailed description of the various numerical simulations carried out and the different FTLE realizations cconsidered is given in Section 3.2.3. Section 3.3 presents results from the idealised simulations. Finally, a summary and discussion of results from the idealised simulations is given in Section 3.4. To mention, this chapter has been published under the title “Three dimensional chaotic advection by mixed layer baroclinic instabilities” (see Mukiibi et al., 2016b).

In Chapter 4, the analysis made in the idealised study is applied to velocity fields of two case study regions of the Atlantic Ocean. Section 4.1.1 describes the model configuration of the simulation from which the velocity fields of the case study regions were extracted. The remainder of this chapter presents the results of the realistically forced datasets and is concluded with the study of the seasonality of submesoscale turbulence in the case study regions. A large component of the findings in this chapter are a subject of another publication in preparation under the title “The seasonality of submesoscale turbulence deduced from finite time Lyapunov exponents” (see Mukiibi et al., 2016a).

Chapter 5 presents a general summary of the thesis and an outlook for future research in line with the findings of this thesis. In particular, Section 5.1 gives a general summary and conclusions drawn from the findings of the thesis. Section 5.2 gives an outlook for future possible research, stating how the findings of this thesis may be extended in future studies.

Appendix A gives an account of a mechanism for the development of large scale fronts studied using a reduced two-layer Quasi-geostrophic model. In specific, Section A.2 describes the reduced model used and also covers a linear stability analysis of the emerging equations of motion. It turns out from the linear stability analysis that the instability development mechanism is governed by the degree of dissipation in the system. For a dissipative system, the development of fronts is governed by the velocity shear and is studied in Section A.3.1. Section A.3.2 considers the almost inviscid case in which the frontal development is determined by the Froude number. The appendix A has been published in the 2014 Geophysical Fluid Dynamics (GFD) summer school proceedings held at Woods Hole Oceanographic Institution (WHOI) (Mukiibi, 2014).

Chapter 2

Theoretical Background

In this Chapter, the theoretical background of chaotic advection involving the process of obtaining particle trajectories and the consequent use of these trajectories to compute Finite Time Lyapunov Exponents (FTLEs) and Finite Size Lyapunov Exponents (FSLEs) is given. In Section 2.4, the relationship between FTLEs and Lagrangian coherent structures (LCSs) is described, first, mentioning the shortcomings of considering ridges of FTLEs as LCSs and second, calculating LCSs using the theory of geodesics.

2.1 Equations of motion

Consider the motion of particles with velocity $\mathbf{U}_{\text{particles}}$ and which are relatively light, such that they are subjected to changing their velocity following the background flow $\mathbf{U}_{\text{fluid}} = (u, v, w)$, in which they are contained. In changing their velocities to that of the fluid, the instantaneous particle velocities are then equal to the Eulerian velocity of the ambient fluid flow, that is,

$$\mathbf{U}_{\text{particles}}(t) = \mathbf{U}_{\text{fluid}}(x(t), y(t), z(t)) \ . \tag{2.1}$$

However, the velocities of individual particles at a location $\boldsymbol{x}(t) = (x, y, z)$ are also given by the rate of change of their position vectors, thus yielding the deterministic dynamical system

$$\frac{d}{dt}x(t) = u(x, y, z, t) \ , \tag{2.2}$$

$$\frac{d}{dt}y(t) = v(x, y, z, t) \ , \tag{2.3}$$

$$\frac{d}{dt}z(t) = w(x, y, z, t) \ , \tag{2.4}$$

where the lefthand and righthand sides of the system (2.2 - 2.4), respectively represent the Lagrangian and Eulerian velocities, with t being the time variable.
It is further assumed that the particles are light and inert such that they cannot do anything but to instantaneously adjust their velocities to that of the ambient flow. Consequently, this phenomenon has been alternatively, but intuitively termed as passive advection (Aref, 2002). For a steady two dimensional (2D) system (i.e in

which the component (2.4) is absent), the resulting dynamical system is integrable. However, if time variability is introduced, a 2D system may be rendered non integrable (e.g., Wiggins, 2005), eventually yielding chaotic particle trajectories. For a 3D system, non integrability is possible even for steady motions (e.g., Dombre et al., 1986; Haller, 2001) and in this case, the term suitable to describe the ensuing motion is chaotic advection (Aref, 1984, 2002). Several studies have also adopted a broader definition of chaotic advection, essentially referring to the process of exponential stretching and folding of fluid elements leading to the increment of gradients in tracer properties and eventually to irreversible mixing (e.g., Pratt et al., 2014).

2.2 Calculation of FTLEs

Consider the velocity field of a flow described by the first order system of ordinary differential equations (2.2 - 2.4) written in vectorial as

$$\frac{\mathrm{d}}{\mathrm{dt}}\boldsymbol{x} = \mathbf{u}(\boldsymbol{x}, t) \ , \tag{2.5}$$

where $\boldsymbol{x} = (x, y, z)$ are the three dimensional particle trajectories. The perturbation to a particle trajectory $\boldsymbol{x}(t)$ in the time interval $[t_1, t_2]$ is computed as $\boldsymbol{\delta}(t_2) = \boldsymbol{x}(t_2) - \boldsymbol{x}(t_1)$. The velocity field $\mathbf{u}(\boldsymbol{x}, t)$ can thus be considered as a map of the flow F which takes the initial position of the particle $\boldsymbol{x}(t_1)$ and returns its final position $\boldsymbol{x}(t_1 + t_2)$ at a later time $t_1 + t_2$ (Ottino, 1990a),

$$F_{t_1}^{t_2}|\boldsymbol{x}(t_1)\rangle \quad = \quad |\boldsymbol{x}(t_1 + t_2)\rangle \ , \tag{2.6}$$

where a bra-ket notation has been adopted (e.g., Shadden et al., 2005; Lekien et al., 2007). For uniqueness of solutions of the flow map, the unity operator of F is defined such that

$$F_{t_1}^{t_1}|\boldsymbol{x}(t_1)\rangle \quad = \quad |\boldsymbol{x}(t_1)\rangle \ . \tag{2.7}$$

Using a Taylor expansion about $|\boldsymbol{x}(t_1)\rangle$, a perturbation $\boldsymbol{\delta}(t_1)$ to a particle trajectory $\boldsymbol{x}(t_1)$ is evolved linearly by the flow map as

$$F_{t_1}^{t_2}|\boldsymbol{x}(t_1) + \boldsymbol{\delta}(t_1)\rangle = F_{t_1}^{t_2}|\boldsymbol{x}(t_1)\rangle + \boldsymbol{\delta}(t_1)\frac{\mathrm{d}}{\mathrm{d}\boldsymbol{x}}F_{t_1}^{t_2}|\boldsymbol{x}(t_1)\rangle + O(\delta^2) \ . \tag{2.8}$$

Assuming that the flow map defined by (2.8) is at leading order linear, the equation for the evolution of the perturbation of a particle trajectory is

$$F_{t_1}^{t_2}|\boldsymbol{\delta}(t_1)\rangle = |\boldsymbol{\delta}(t_1 + t_2)\rangle = \boldsymbol{\delta}(t_1)\frac{\mathrm{d}}{\mathrm{d}\boldsymbol{x}}F_{t_1}^{t_2}\,|\boldsymbol{x}(t_1)\rangle \ , \tag{2.9}$$

and its square norm is

$$\begin{aligned} \|\boldsymbol{\delta}(t_1 + t_2)\|^2 &= \langle\boldsymbol{\delta}(t_1 + t_2)|\boldsymbol{\delta}(t_1 + t_2)\rangle \ , \\ &= \left\langle \boldsymbol{\delta}(t_1)\frac{\mathrm{d}}{\mathrm{d}\boldsymbol{x}}F_{t_1}^{t_2}\boldsymbol{x}(t_1)|\boldsymbol{\delta}(t_1)\frac{\mathrm{d}}{\mathrm{d}\boldsymbol{x}}F_{t_1}^{t_2}\boldsymbol{x}(t_1)\right\rangle \ , \end{aligned} \tag{2.10}$$

where $||\cdot||$ is the three dimensional Euclidean norm. Thus, the square of the norm of the resulting perturbation in a particle trajectory after a time (t_1+t_2) is given by the expression

$$\|\boldsymbol{\delta}(t_1+t_2)\|^2 = \left\langle \boldsymbol{\delta}(t_1)\right| \left[\frac{\mathrm{d}}{\mathrm{d}\boldsymbol{x}}F_{t_1}^{t_2}\boldsymbol{x}(t_1)\right]^{\top} \left[\frac{\mathrm{d}}{\mathrm{d}\boldsymbol{x}}F_{t_1}^{t_2}\boldsymbol{x}(t_1)\right] \left|\boldsymbol{\delta}(t_1)\right\rangle \ , \tag{2.11}$$

where, $[\cdot]^{\top}$ is obtained by taking the complex conjugates of the entries of the matrix $[\cdot]$ and then taking its transpose. The matrix given by

$$\begin{aligned} \mathcal{D}_{t_1}^{t_2}(\boldsymbol{x}_1) &= \left[\frac{\mathrm{d}}{\mathrm{d}\boldsymbol{x}}F_{t_1}^{t_2}\boldsymbol{x}(t_1)\right]^{\top} \left[\frac{\mathrm{d}}{\mathrm{d}\boldsymbol{x}}F_{t_1}^{t_2}\boldsymbol{x}(t_1)\right] \ , \\ &= \left[\boldsymbol{\nabla}F_{t_1}^{t_2}(\boldsymbol{x}_1)\right]^{\top}\left[\boldsymbol{\nabla}F_{t_1}^{t_2}(\boldsymbol{x}_1)\right] \ , \end{aligned} \tag{2.12}$$

is the finite-time right Cauchy-Green deformation tensor. The left Cauchy-Green strain tensor is similarly defined as $\left[\boldsymbol{\nabla}F_{t_1}^{t_2}(x_1)\right]\left[\boldsymbol{\nabla}F_{t_1}^{t_2}(\boldsymbol{x}_1)\right]^{\top}$ (e.g., Arnold, 1973; Ottino, 1989; Truesdell and Noll, 2004). From its construction, the Cauchy-Green strain tensor $\mathcal{D}_{t_1}^{t_2}(\boldsymbol{x}_1)$ is a real positive definite tensor, with real eigenvalues and orthogonal eigenvectors. Equation (2.11) can therefore be written as

$$\begin{aligned} \|\boldsymbol{\delta}(t_1+t_2)\|^2 &= \left\langle \boldsymbol{\delta}(t_1)\right|\mathcal{D}_{t_1}^{t_2}(\boldsymbol{x}_1)\left|\boldsymbol{\delta}(t_1)\right\rangle \ , \\ &= C_i\langle\boldsymbol{\delta}(t_1)|\boldsymbol{\delta}(t_1)\rangle = C_i\|\boldsymbol{\delta}(t_1)\|^2 \ , \ i=1,\ldots,3 \end{aligned} \tag{2.13}$$

where C_i are the eigenvalues of the operator $\mathcal{D}_{t_1}^{t_2}(\boldsymbol{x}_1)$ and is defined such that it satisfies the relation

$$\mathcal{D}_{t_1}^{t_2}(\boldsymbol{x}_1)\left|\boldsymbol{\delta}(t_1)\right\rangle = C_i\left|\boldsymbol{\delta}(t_1)\right\rangle \ . \tag{2.14}$$

In a chaotic advection flow regime, initially infinitesimal perturbations in particle paths grow exponentially i.e

$$||\boldsymbol{\delta}(t_1+t_2)|| = ||\boldsymbol{\delta}(t_1)||\exp\left[\lambda^*(t_2-t_1)\right] \ , \tag{2.15}$$

from which the scalar $\lambda_{t_1}^{t_2*}(\boldsymbol{x}_1)$, the Lyapunov exponent (e.g., Arnold, 1973; Truesdell and Noll, 2004) is computed in the limits of infinite time and infinitesimal initial separation, that is,

$$\lambda_{t_1}^{t_2*}(\boldsymbol{x}_1) = \lim_{\delta(t_1)\to 0}\lim_{t_2\to\infty}\frac{1}{|t_2-t_1|}\log\left[\frac{||\boldsymbol{\delta}(t_1+t_2)||}{||\boldsymbol{\delta}(t_1)||}\right] \ . \tag{2.16}$$

Since velocity fields $\mathbf{u}(t)$ defined in (2.5) are only available for finite periods of time and are also computed in numerical models at finite resolutions, the asymptotic limits in (2.16) are loosened and the resulting scalar $\lambda_{t_1}^{t_2}(\boldsymbol{x}_1)$ has been referred to as the Finite Time Lyapunov Exponent (FTLE) (e.g., Haller, 2000; Wiggins, 2005; Shadden et al., 2005). Combining (2.13) and (2.16) with the loosened asymptotics, the FTLEs $\lambda_{t_1}^{t_2}(\boldsymbol{x}_1)$ can thus be calculated from the expression

$$\lambda_{t_1}^{t_2}(\boldsymbol{x}_1) = \frac{1}{|t_2 - t_1|}\log\left[\frac{||\boldsymbol{\delta}(t_1+t_2)||}{||\boldsymbol{\delta}(t_1)||}\right] = \frac{1}{|t_2 - t_1|}\log\left[C_{max}\right]^{1/2} \ , \tag{2.17}$$

where C_{max} is the largest of the eigenvalues C_i of the operator $\mathcal{D}_{t_1}^{t_2}(\boldsymbol{x}_1)$ defined in (2.12). From (2.17), it becomes apparent that the scalar field $\lambda_{t_1}^{t_2}(\boldsymbol{x}_1)$ is a measure of the rate of particle separation in the time interval $[t_1, t_2]$ whose magnitude is dependent upon the length of the time interval $\tau = t_2 - t_1$ and the particle separartion $\boldsymbol{\delta}(t_1 + t_2)$. The magnitude sign is emphasised in the denominator of (2.17) since calculation of $\lambda_{t_1}^{t_2}(\boldsymbol{x}_1)$ can be considered for both $t_2 > t_1$ (yielding forward in time FTLEs) and $t_2 < t_1$ (yielding backward in time FTLEs) (see Fig. 2.1). One of the several strengths of the Lagrangian measure $\lambda_{t_1}^{t_2}(\boldsymbol{x}_1)$ is apparent from this computation scheme, in that it reconstructs the history, and predicts the futures of the synthetic particles over the entire time interval $t_1 < t < t_2$, rather than giving a simplistic Eulerian snapshot of the flow.

It is also important to note that there are two possible schemes of computing forward and backward in time FTLEs. In the first scheme, the forward and backward integrations sample the same time window (hence dynamics) $[t_1, t_2]$ but consider different initial conditions (Fig. 2.1a). In the second, both integrations have common initial conditions at $t_0 \in [t_1, t_2]$ but sample different windows hence dynamics of the finite time dynamical system (Fig. 2.1b). In this thesis, the first scheme is considered since we are interested in understanding the statistics of the flow in the entire integration time window $[t_1, t_2]$. It has also been shown that both forward and backward in time FTLEs can be obtained in a uni-direction simulation (e.g., Haller and Sapsis, 2011; Farazmand and Haller, 2013) which reduces the computation cost and time required to obtain FTLEs. Further, several studies have reported various efforts toward the development of efficient and cost effective algorithms used in the numerical computation of FTLEs (e.g., Lekien and Marsden, 2005; Sadlo and Peikert, 2007; Brunton and Rowley, 2010; Leung, 2011) which has led to the FTLEs being a quick and widely accepted tool in the diagnosis of unsteady flows (see; Haller, 2015, for related literature).

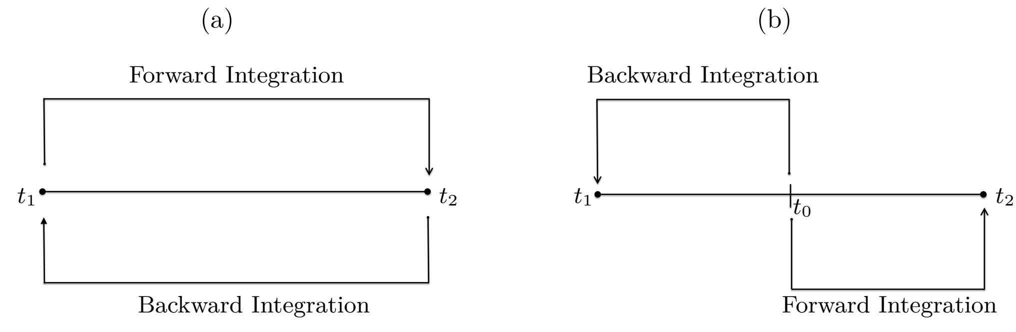

Figure 2.1: Diagramatic illustration of the integration windows that could be selected when integrating particle trajectories. (a) Both forward and backward integrations consider the same dynamics but different initial conditions. (b) Forward and backward integrations have the same initial conditions at time t_0 but sample different dynamics of the flow.

The eigenvector associated to C_{max} corresponds to the direction along which maximum separation of initially, infinitesimally close particles occurs. Equation (2.17) shows that the scalar field λ is a measure of the rate of particle separation in the time interval $[t_1, t_2]$. Equation (2.17) also shows that the length of the time interval of integration $[t_1, t_2]$ determines the magnitude of the FTLEs following an inverse relation. Longer integration times yield finer and more detailed FTLE fields (e.g., Lapeyre, 2002; Shadden et al., 2005; Mathur et al., 2007; Harrison and Glatzmaier, 2012). However, from a geophysical point of view, it is also important to select the length of the time interval of integration based on the flow dynamics. A meaningful time interval should be long enough to cover the life span of the longest dynamics in the flow domain, ensuring that all the stirring influences of vortices and filaments are fully captured in the calculation of the FTLEs.

2.3 Calculation of FSLEs

Considering the first equality of (2.17) in a slightly different form as

$$\lambda_s = \frac{1}{|t_2 - t_1|} \log \left[\frac{||\boldsymbol{\delta}(t_1 + t_2)||}{||\boldsymbol{\delta}(t_1)||} \right] = \frac{1}{\tau(\boldsymbol{x}_1, \boldsymbol{\delta}(t_1), \gamma)} \log[\gamma] \;, \tag{2.18}$$

$$\text{with} \quad \tau = t_2 - t_1 \text{ and } \gamma = \frac{||\delta(t_1 + t_2)||}{||\delta(t_1)||} = C_0 \equiv \text{constant.}$$

The scalar λ_s is the finite size Lyapunov exponent (FSLE), and the ratio γ of particle separation at a later time $(t_1 + t_2)$ to their initial separation $\delta(t_1)$ at time t_1 has been referred to as the amplification factor (e.g., Artale et al., 1997; Aurell et al., 1997; Boffetta et al., 2001; d'Ovidio et al., 2004; Cencini and Vulpiani, 2013). The numerical computation of λ_s involves tracking of particle pairs and obtaining the time $\tau = t_2 - t_1$ after which the final separation of a given particle pair is a preset factor γ larger than their initial separation at time t_1. It is also noted that in addition to the initial separation of particle pairs and the length of the time interval, FSLEs are also dependent on the amplification factor γ i.e $\lambda_s = \lambda_s(\boldsymbol{x}(t_1); \delta(t_1), \gamma)$. The dependence of FSLEs on the amplification factor γ makes FSLEs a suitable diagnostic tool in the study of flow phenomenon over a broad range of spatial scales, facilitated by the possibility of fine tuning γ to emphasize flow features of interest (e.g., Boffetta et al., 2001; Joseph and Legras, 2002; d'Ovidio et al., 2004; Karrasch and Haller, 2013).

In the application of FSLEs to detect coherent structures, a heuristic analogy of ridges of FTLE fields to those of FSLEs fields is made due to the visual similarity of the two fields (e.g., d'Ovidio et al., 2004; Bettencourt et al., 2012, 2013). While detection of coherent structures has since digressed from consideration of ridges of FTLE fields (see; Haller, 2015, for a review), in itself, the analogy between ridges of FTLE and FSLE fields was mathematically shown to hold but under strict constraints due to irregularities in the FSLE field which include (Karrasch and Haller, 2013):

- Ill-posedness of FSLE fields

While FTLEs are always defined for any initial conditions and integration time $t \in [t_1, t_2]$, FSLEs remain undefined in locations where final particle separations $\delta(t_1 + t_2) < \gamma\delta(t_1)$ (as follows from (2.18)). This effect spreads to more locations in the domain as γ is made larger since fewer particle pairs would attain separations $\geq \gamma\delta(t_1)$.

- Insensitivity of FSLEs to later changes in the flow

  It is noted that once the particle pair separation reaches $\gamma\delta(t_1)$ and the time $\tau(\boldsymbol{x}_1, \boldsymbol{\delta}(t_1), \gamma)$ is captured, the FSLE field ignores any further changes in the particle trajectories. This is in contrast to the FTLE field which captures the dynamics of the flow for the entire time interval $[t_1, t_2]$.

- Sensitivity of FSLEs to temporal resolution

  The jump-discontinuities in the preceding point above indirectly imply that FSLE fields are dependent on the temporal resolution of the velocity field. Since time is discretised in outputs of numerical models, this effect therefore imposes a constraint to the use of FSLEs requiring that velocity fields are computed at high temporal resolution.

- Spurious ridges

  Like it has been shown that the flux across ridges of FTLEs can be large (see the following section) (e.g., Haller, 2001), ridges of FSLEs are no exception to this flaw and thus cannot be considered to be material surfaces.

The reader is directed to Karrasch and Haller (2013) for a detailed discussion and examples of the above shortcomings of FSLEs. In case the above issues of FSLEs are carefully handled, the analogy of ridges of FSLEs and FTLEs is meaningful and has been used with success to studies of stirring for both analytic (e.g., Bettencourt et al., 2013; Karrasch and Haller, 2013) and geophysical flows (e.g., Joseph and Legras, 2002; d'Ovidio et al., 2004, 2009; Bettencourt et al., 2012; Garaboa-Paz et al., 2015). In this thesis, LCSs will be extracted as explicitly parametrized curves infered from invariants of the Cauchy-Green strain tensor defined in (2.12) following findings of recent studies. A discussion of the most recent techniques in computing LCSs is given in the following section.

2.4 Extraction of LCSs

Lagrangian Coherent Structures (LCSs) due to a given flow field $\mathbf{u}(\boldsymbol{x}, t)$, are the most repelling, attracting and/or shearing material surfaces which form the skeleton of observed flow patterns due to the deforming fluid elements under the action of the flow (e.g., Haller and Yuan, 2000; Haller, 2015). This definition outlines that LCSs be material in nature i.e made of the same elements as the fluid itself and thus can only be advected and deformed by the flow map but do not admit any flux of fluid across them. Previously, several studies sought LCSs as hypersurfaces along which stretching and/or compression of fluid patches is maximal over the time interval of interest (e.g., Haller and Yuan, 2000; Haller, 2001). Shadden et al. (2005) and Lekien et al. (2007) derive a mathematical framework in which LCSs are extracted as second derivative ridges (or trenches, see, e.g., Beron-Vera et al. (2010)) of FTLE fields.

In this framework, a ridge of a scalar field $\mho$ is defined as a curve (in two dimensions) and/or surface (in three dimensions) along which there's minimal variation in the values of $\mho$ but maximum variation in the directions transverse to it (e.g., Schultz et al., 2010; Fuchs et al., 2012; Schindler et al., 2012). This implies that an object straddling along this curve or surface is always at the highest local altitude to the neighbouring regions and stepping away from it in a transverse direction, the object would be stepping to a relatively low altitude. Surfaces and curves delineated by FTLE ridges were thus computed and assumed to be akin to stable and unstable manifolds (Ottino, 1989, 1990a; Wiggins, 2005) of a classic dynamical system; essentially dividing the flow domain into dynamically distinct regions with no flux between each other (e.g., Haller, 2001; Lekien et al., 2007). Assuming a heuristic analogy between FSLE and FTLE ridges, several studies have considered ridges of FSLE fields as LCSs in both atmospheric (e.g., Boffetta et al., 2001; Joseph and Legras, 2002; Garaboa-Paz et al., 2015) and oceanic flows (e.g., d'Ovidio et al., 2004, 2009; Bettencourt et al., 2012, 2013). The reader is directed to a review by Cencini and Vulpiani (2013) for a detailed listing of literature on the application of FSLEs to coherent structure identification.

However, recently it has been shown that second derivative ridges of FTLE fields predict existence of LCSs in locations where they actually do not exist and fail to yield LCSs in locations where they are known to exist (e.g., Haller, 2011; Farazmand and Haller, 2012). Further studies have claimed that the argument of using second derivative ridges as LCSs is too simplistic and cannot be used for coherent structure detection in generic flows (see e.g., Norgard and Bremer 2012 and Peikert et al. 2013 for a counter argument). Rutherford et al. (2010) also report that ridges of FTLE fields are not suited for LCS detection in rapidly rotating flows. The forementioned shortcomings of extraction of LCSs as ridges of FTLE fields have however been addressed in recent studies by defining LCSs as explicitly parameterized curves derived from invariants of the deformation field (e.g., Haller, 2011; Olascoaga and Haller, 2012; Farazmand et al., 2014; Beron-Vera et al., 2013; Blazevski and Haller, 2014). The variational theory of LCS extraction (Haller, 2011) specifically targets LCSs as material curves advected by the flow map $F_{t_1}^{t_2}$ and also offers the option of obtaining both hyperbolic (i.e normally attracting and repelling) and elliptic (e.g vortex boundaries) type LCSs as opposed to the FTLE ridge definition, which emphasizes

LCSs of hyperbolic type (Farazmand and Haller, 2012) and (see Haller, 2015, for a review).

2.4.1 Geodesic theory of LCSs
Elliptic LCSs

The term Lagrangian in the accronym LCS, requires that LCSs are material curves and/or surfaces $\mathcal{M}(t_1)$ present in the fluid starting at the initial time t_1, and whose later positions are defined by the flow map as

$$F_{t_1}^{t_2}\mathcal{M}(t_1) = \mathcal{M}(t_2) \ . \tag{2.19}$$

However, to ensure that the resulting surfaces $\mathcal{M}(t_2)$ have zero flux, it is constrained further that the normal repulsion of neighbouring fluid elements, must remain atleast an order of magnitude larger than pertubations of the neighbouring fluid elements. Further, variations of the surface $\mathcal{M}(t_2)$ are advected by the linearised flow map according to (2.9), and thus, a unit normal n_0 on $\mathcal{M}(t_1)$ is not necessarily normal to $\mathcal{M}(t_2)$ (Haller, 2011). Also, since $\mathcal{M}(t_2)$ is not necessarily flat, the metric to quantify distances in such arbitrary surfaces is not constant, changing its form according to the shape of $\mathcal{M}(t_2)$. The length of a line segment in surfaces of arbitrary shape can be given in terms of geodesics. A geodesic on a surface is a curve connecting two given points, such that any nearby curve with the same end points is longer (Pokorny, 2012). As an example, the geodesics on a sphere would be circles connecting 2 given points and are thus primarily functionals of the arclength over the surface of the sphere. The variational theory of LCSs provides the necessary and sufficient conditions for the existence of LCSs in terms of the invariants of the Cauchy-Green deformation tensor, and in an objective (i.e frame independent) way (e.g., Haller, 2011; Farazmand and Haller, 2012). The eigenvalues λ_i and eigenvectors ξ_i of the Cauchy-Green strain tensor $\mathcal{D}_{t_1}^{t_2}(\boldsymbol{x}_1)$ defined in (2.12) satisfy the relations,

$$\mathcal{D}\xi_i = \lambda_i \xi_i \ , \ \xi_2 = \Omega \xi_1 \ , \tag{2.20}$$

with $0 < \lambda_1 < \lambda_2$, $i = 1, 2$, and $\Omega = \begin{bmatrix} 0 & -1 \\ 1 & 0 \end{bmatrix}$.

Elliptic LCSs are sought as positions of closed material lines that prevail as Lagrangian coherent vortices over a time interval $[t_-, t_+] \in [t_1, t_2]$. These material line positions have been shown to be closed stationary curves of the averaged strain functional (Haller and Beron-Vera, 2012, 2013)

$$Q(\sigma) = \frac{1}{\sigma} \int_0^\sigma \frac{\sqrt{\langle r'(s), \mathcal{D}_{t_-}^{t_+}(r(s)) r'(s) \rangle}}{\sqrt{\langle r'(s), r'(s) \rangle}} \, \mathrm{d}s \ , \tag{2.21}$$

obtained by averaging the tangential strain along parameterized curves $r(s)$ over the time interval $[t_-, t_+]$ with $s \in [0, \sigma]$. Further, the stationary curves of $Q(\sigma)$ in (2.21) were shown to be closed orbits of the vector field

$$\eta_\pm^\lambda = \sqrt{\frac{\lambda_2 - \lambda^2}{\lambda_2 - \lambda_1}} \, \xi_1(\mathbf{x}_1) \pm \sqrt{\frac{\lambda^2 - \lambda_1}{\lambda_2 - \lambda_1}} \, \xi_2(\mathbf{x}_1) \ , \tag{2.22}$$

with the vector field family (2.22) satisfying the differential equation

$$r'(s) = \eta_{\pm}^{\lambda} \ , \tag{2.23}$$

where λ serves as a parameter. Equation (2.23) coincides with the null geodesics of the Lorentzian metric (e.g., Beron-Vera et al., 2013; Blazevski and Haller, 2014)

$$g_{\lambda}(u, v) = \langle u, E_{\lambda} v \rangle \ , \qquad \lambda > 0, \quad \text{where} \tag{2.24}$$

$$E_{\lambda}(\mathbf{x}_1) = \frac{1}{2}\left(\mathcal{D}_{t_-}^{t_+}(\mathbf{x}_1) - \lambda^2 I\right) \ , \tag{2.25}$$

is the generalised Green-Lagrange strain tensor, that measures the deviation of an infinitesimal deformation from a uniform spherical expansion by a factor λ. The null geodesics resulting from (2.23) are tangent to the set of vectors in (2.22). For a range of values of λ, solutions to (2.23) are a family of closed orbits with each orbit increasing its arclength by the respective factor of λ and hence such solutions have been called "λ-lines" (e.g., Onu et al., 2015).

2.4.2 Hyperbolic LCSs

Hyperbolic LCSs are defined as stationary curves of the averaged shear functional over the interval $[t_-, t_+] \in [t_1, t_2]$

$$Q(\sigma) = \frac{1}{\sigma}\int_0^{\sigma} \frac{\langle r'(s), \mathcal{D}_{t_-}^{t_+}(r(s)) r'(s)\rangle}{\sqrt{\langle r'(s), \mathcal{D}_{t_-}^{t_+}(r(s)) r'(s)\rangle \langle r'(s), r'(s)\rangle}} \mathrm{d}s \ , \tag{2.26}$$

which also coincides with the null geodesics of the Lorentzian metric (Farazmand et al., 2014)

$$g(u, v) = \langle u, G v\rangle \ , \tag{2.27}$$

with

$$G_{t_-}^{t_+}(\mathbf{x}_1) = \frac{1}{2}\left(\mathcal{D}_{t_-}^{t_+}(\mathbf{x}_1)\Omega - \Omega\mathcal{D}_{t_-}^{t_+}(\mathbf{x}_1)\right) \ , \tag{2.28}$$

and Ω defined in (2.20). The geodesic problem in (2.27) yields a set of differential equations

$$\mathbf{r}_1' = \xi_1(r) \ , \ \mathbf{r}_2' = \xi_2(r) \ , \tag{2.29}$$

from which Repelling and Attracting LCSs are respectively computed as explicitly parameterized curves, with the parameter r being the arc length along the LCS. For a detailed discussion of the geodesic extraction of LCSs, the reader is directed to (Haller, 2015, and references therein) and to (Onu et al., 2015) for a numerical implementation of the derivations discussed above. The latter study is also acknowledged for developing LCS-Tool, a computational engine for computing LCSs from two dimensional unsteady flows, which was used in the current study.

Chapter 3

Idealised Simulations

In this chapter, the numerical model configuration, initial and boundary conditions are described. A description of the various simulations carried out and a list of parameters used in all numerical simulations is also given. Section 3.2 outlines the methodology of obtaining particle trajectories and the procedure of calculating the deformation tensor. The different numerical experiments conducted are described in subsection 3.2.3. Results of the idealised simulations are presented in Section 3.3 and finally, a summary and discussion of the results is provided in Section 3.4. Noteworthy, the contents of this chapter have been published (see Mukiibi et al., 2016b).

3.1 Model set-up

An ML front in a channel configuration is considered, using a numerical primitive equation model, the Massachusetts Institute of Technology general circulation model (MITgcm) (Marshall et al., 1997a,b). In this thesis, we use the MITgcm in hydrostatic mode since Mahadevan (2006) reports that non-hydrostatic effects are not relevant at submesoscales as is the case in our simulations. A similar model configuration as in Boccaletti et al. (2007) is adopted. The domain spans 192 km both in the zonal and meridional directions and is 300 m deep. The zonal and meridional resolutions are both set at 500 m while the vertical resolution is uniformly set as 5 m.

3.1.1 Boundary conditions

The channel is re-entrant with periodic boundary conditions along the zonal direction, so that fluid that exits at $x = 192$ km is re-admitted back into the channel at $x = 0$ km while fluid that exits at $x = 0$ km is also re-admitted into the channel at $x = 192$ km i.e $\mathbf{u}(x = 0) = \mathbf{u}(x = 192 \text{ km})$. The meridional walls of the channel are rigid and impermeable with free slip boundary conditions. The bottom of the channel is set with no topography and with free slip boundary conditions. The top of the channel satisfies free surface boundary conditions. Model parameters used in the numerical simulations are presented in Table 3.1.

Table 3.1: Table of model parameters used in all simulations.

Parameter	Symbol	Value
Coriolis parameter	f	1.0284×10^{-4} s^{-1}
Beta ($\frac{df}{dy}$)	β	$\times 10^{-11}$ s^{-1} m^{-1}
Gravitational acceleration	g	9.81 m s^{-2}
Horizontal length of the channel	L_x	192 km
Meridional length of the channel	L_y	192 km
Depth of the channel	H_{tot}	300 m
Mixed layer depth	H_{ML}	100 m
Spatial resolution	(dx, dy, dz)	(500, 500, 5) m
Lateral biharmonic viscosity	ν_H	2×10^5 m^4 s^{-1}
Vertical eddy viscosity	ν_v	1×10^{-4} m^2 s^{-1}
Lateral biharmonic diffusivity of heat	K_T	1×10^2 m^4 s^{-1}
Lateral biharmonic diffusivity of salt	K_S	1×10^2 m^4 s^{-1}
Vertical diffusivity of temperature	K_{Tz}	1×10^{-5} m^2 s^{-1}
Vertical diffusivity of salt	K_{Sz}	1×10^{-5} m^2 s^{-1}

3.1.2 Initial conditions

The channel is initialized with a ML front, in which a density gradient is aligned in the zonal (East - West) direction and is 100 m deep (see Fig. 3.1). The ML front is

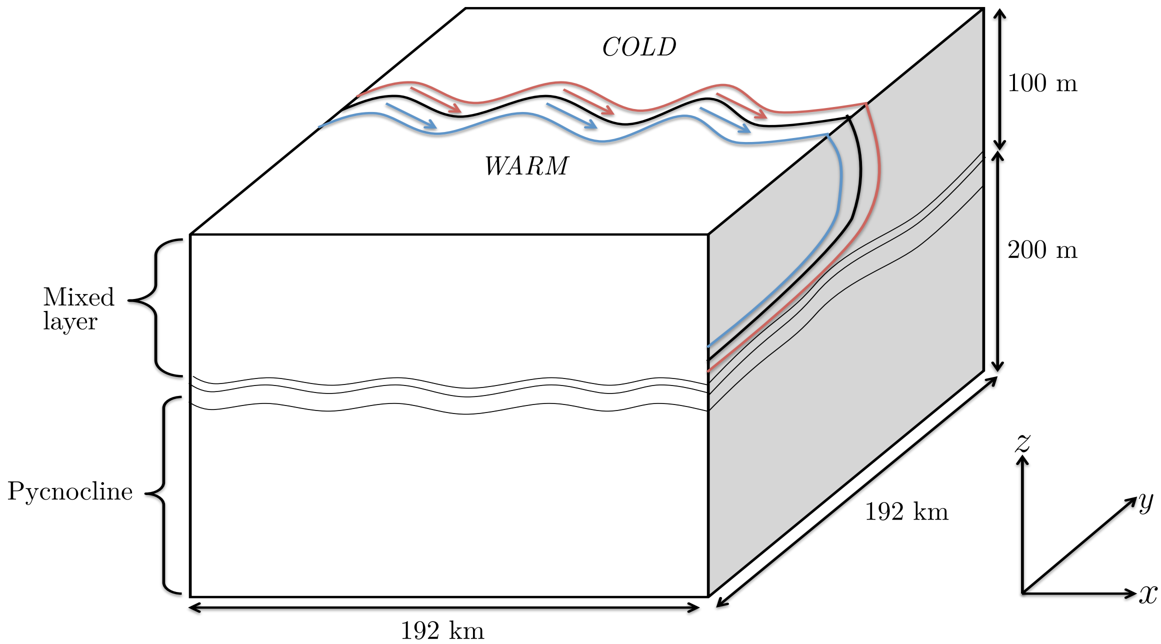

Figure 3.1: Diagramatic illustration of the channel geometry represented by the numerical model. The domain measures 192km × 192km × 300m. The configuration has a mixed layer front in the middle of the domain.

positioned at $y = L_y/2$ i.e 96 km north of the southern boundary of the channel. The southern part of the channel contains lighter, warm and more saline waters at the

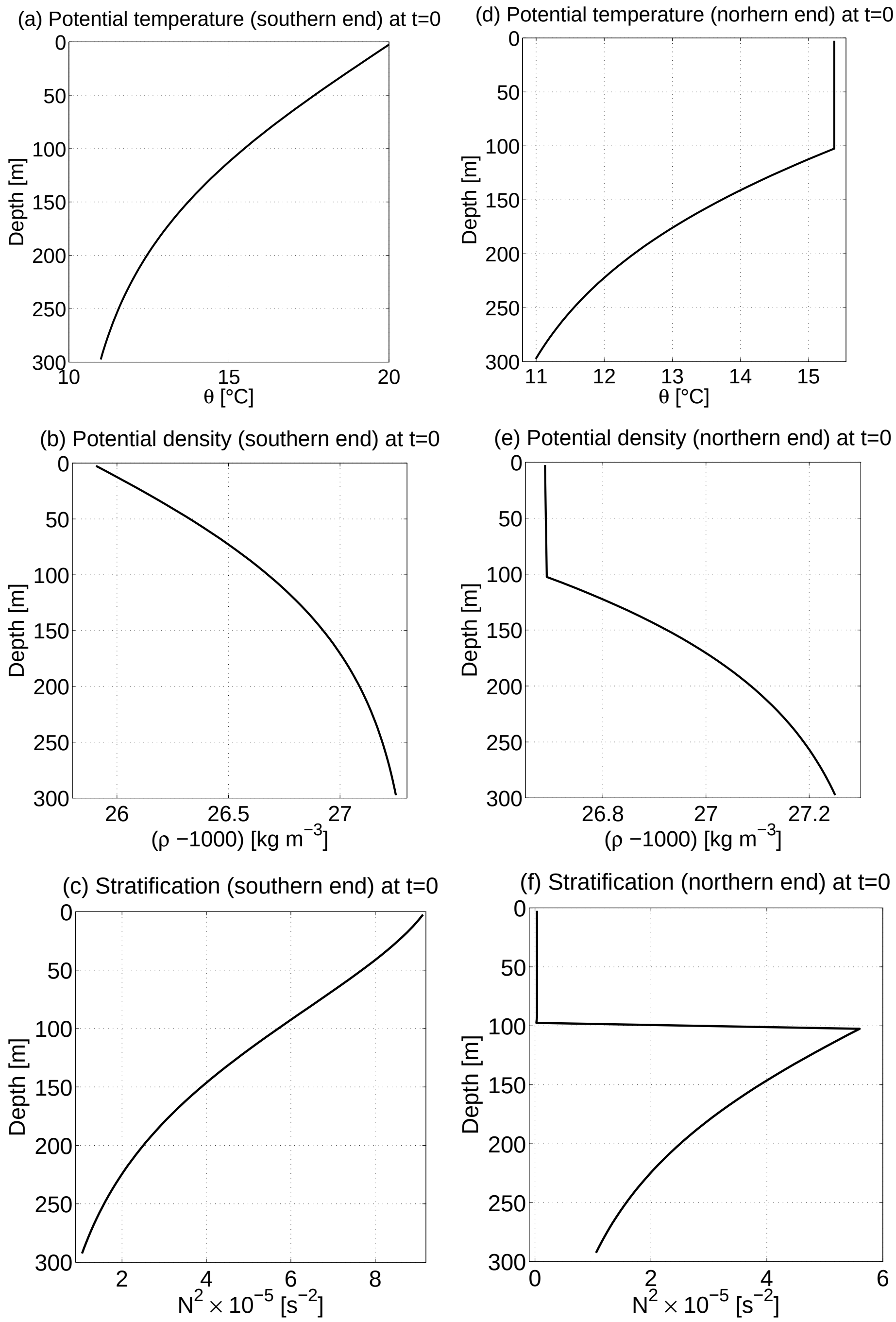

Figure 3.2: Vertical profiles of (a, b) Potential temperature , (b, e) potential density and (c, f) buoyancy frequency at the start of the numerical simulation (i.e $t = 0$) in the southern and northern end of the channel.

surface, while the northern part of the channel is initialized with heavier, cold waters at the surface (Figs. 3.2a,b,d,e). The ML lies upon an initially quiescent pycnocline with flat isopycnals. The temperature and salinity profiles used in the reference numerical simulation, set an initial uniform buoyancy frequency in the ML which, following an hyperbolic tangent function, decreases with depth in the pycnocline

(Fig. 3.2f). On the southern end of the ML, the initial stratification profile is such that it decreases exponentially with depth (Fig. 3.2c).
The front is implemented by analytic expressions of temperature T and salinity S of the form

$$\mathrm{T} = 20.0 - 10.0 \times \tanh\left(\frac{z - z_o}{200}\right) \text{ and} \tag{3.1}$$

$$\mathrm{S} = 36.5 - 10.0 \times \tanh\left(\frac{z - z_o}{200}\right) , \tag{3.2}$$

respectively. T is given in units of [°C] while S is defined in units of [psu]. The variable z (in units of [m]) is the vertical height from the channel surface defined such that

$$z = \begin{cases} 0 \,; & \text{at the channel surface,} \\ 300 \,; & \text{at the channel bottom.} \end{cases} \tag{3.3}$$

The dynamically unstable ML front is allowed to adjust without any restoration under geostrophic adjustment(e.g., Tandon and Garrett, 1994, 1995), that is, with no external source of energy to the system. The initially, nearly vertical isopycnals in the ML provide the energy (in the form of available potential energy (APE)) upon which the developing baroclinic instability draws (e.g., Stone, 1966; Molemaker and McWilliams, 2005); eventually slumping the initially vertical isopycnals to the horizontal thus yielding a stably stratified fluid (e.g., Boccaletti et al., 2007; Fox-Kemper et al., 2008). In reality, various sources of energy come into play as the front adjusts, acting either to reinforce and/or oppose the adjustment process, thus making the stratification - restratification cycle a bit more complex than we consider in the current idealised study. A noteworthy source of forcing that influences the adjustment cycle of fronts is the wind stress and in particular its orientation. Lee et al. (2006) report that upfront wind enhances restratification and accelerates the adjustment of any existing fronts. Down-front winds instead carry denser waters above lighter water, arresting the adjustment process of fronts and further enhancing the APE reservoir from which baroclinic instabilities that restratify the ML draw (e.g., Thomas and Lee, 2005; Mahadevan et al., 2010). Other sources of energy that come into play include but are not limited to: frontogenesis arising from the interaction of mesoscale eddies leading to secondary instabilities which accelerate the restratification of the upper ocean (Spall, 1995; Lapeyre et al., 2006) and bouyancy forcing on the ocean surface emerging from heat loss (or gain) and precipitation (or evaporation).

It should be noted that, as the model is based on primitive equations, the vertical velocity is only diagnosed from the divergence of the horizontal velocities. However, for the set-up and scales analyzed in this study, the most important part of the vertical velocity is captured by the divergence of the horizontal flow. Mahadevan (2006) and Mahadevan and Tandon (2006) report that with sufficient spatial resolution, the vertical velocities can be accurately calculated.

3.2 Methodology

3.2.1 Computation of particle trajectories

A time interval $\tau = t_2 - t_1$ during which the particle motion is investigated is selected. The lower limit t_1 is selected at an instant after the initial spin-up of the model, when the flow is well developed to reveal the stirring influence of the instability. On the channel surface, the front starts to show meanders after ~ 10 days which roll into eddies in the next ~ 10 days and eventually becoming completely unstable (Fig. 3.3 a,b,c). By day 25, vortices of various sizes are observed to break away from the main frontal region and the instabilities cover larger areas of the channel (Fig. 3.3 d,e,f). The value of t_2 is made as large as possible depending on the computational resources available, but less than the time at which the instabilities reach the meridional boundaries of the channel. The velocity field in the time window τ is then written out every 15 minutes. A regular grid of particles is set at each grid point in the domain, for a total of 8,609,516 particles.

The particle trajectories are integrated using a Runge-Kutta fourth order scheme. For spatial interpolations of the velocity field, a tricubic scheme is adopted while a linear scheme is used for temporal interpolations. Computation of trajectories is not considered for particles on the boundaries of the channel. FTLEs are calculated using both forward and backward integration in time, where the backward integration is performed in the interval $[t_2, t_1]$. A note of caution is here obligatory: the forward and backward integration allows to use the same flow, however it relies on different initial conditions. This choice has been made in order to compare the statistics of the FTLEs, however no comparison of snapshots of the field should be attempted.

3.2.2 Numerical computation of FTLEs

In the current study, we consider the operator, $\left(\frac{\mathrm{d}}{\mathrm{d}\boldsymbol{x}} F_{t_1}^{t_2} \boldsymbol{x}(t_1) = \frac{\mathrm{d}}{\mathrm{d}\boldsymbol{x}} \boldsymbol{x}(t_1 + t_2)\right)$ to be the 3×3 matrix $\mathbf{D}$ whose entries are numerically obtained as finite differences (e.g., Haller, 2001, 2015). For a particle located away from the channel boundaries, there are six nearest neighbors, laying along the three cardinal directions i.e North (N) - South (S), East (E) - West (W) and Top (T) - Bottom (B) (Fig. 3.4). Components of the deformation tensor are computed as

$$\mathbf{D} = \begin{pmatrix} \left(\dfrac{x_2^E - x_2^W}{x_1^E - x_1^W}\right) & \left(\dfrac{x_2^N - x_2^S}{y_1^N - y_1^S}\right) & \left(\dfrac{x_2^T - x_2^B}{z_1^T - z_1^B}\right) \\ \left(\dfrac{y_2^E - y_2^W}{x_1^E - x_1^W}\right) & \left(\dfrac{y_2^N - y_2^S}{y_1^N - y_1^S}\right) & \left(\dfrac{y_2^T - y_2^B}{z_1^T - z_1^B}\right) \\ \left(\dfrac{z_2^E - z_2^W}{x_1^E - x_1^W}\right) & \left(\dfrac{z_2^N - z_2^S}{y_1^N - y_1^S}\right) & \left(\dfrac{z_2^T - z_2^B}{z_1^T - z_1^B}\right) \end{pmatrix}, \tag{3.4}$$

where $\boldsymbol{x}_1 = \boldsymbol{x}(t_1)$ and $\boldsymbol{x}_2 = \boldsymbol{x}(t_2)$ are the particle positions at times t_1 and t_2 respectively. The FTLEs λ are then obtained from (2.17), where C_{max} is the maximum of the eigenvalues of $\mathcal{D}_{t_1}^{t_2}(\boldsymbol{x}_1) = \left(\mathbf{D}^\top \mathbf{D}\right)$.

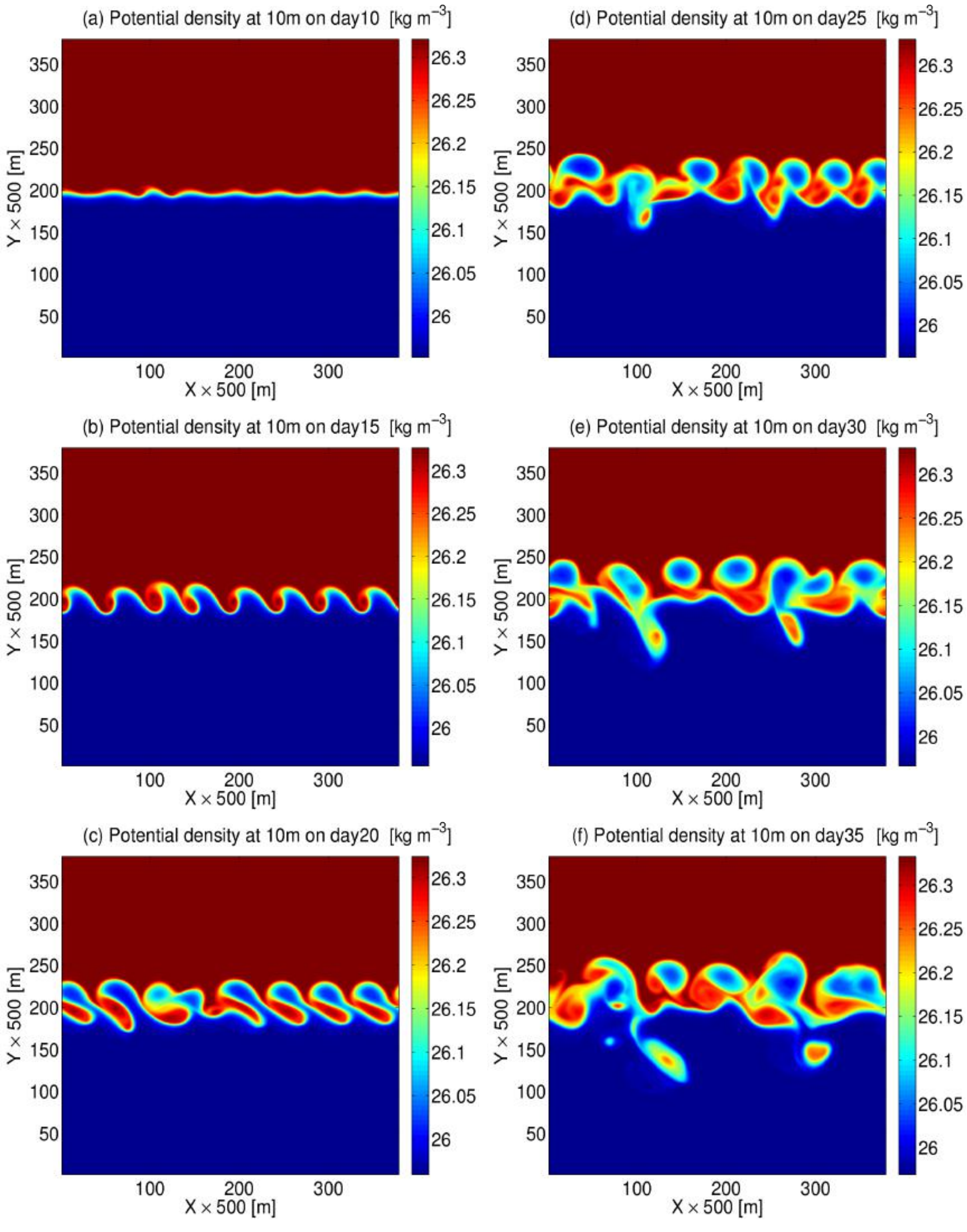

Figure 3.3: Snapshots of the potential density anomaly ($\sigma_t = \rho - 1000$) at the depth of 10 m taken at times (a) 10, (b) 15, (c) 20, (d) 25, (e) 30 and (f) 35 days. Colorbars are in units of kg m^{-3}.

3.2.3 Numerical experiments

A set of five numerical experiments have been conducted with different values of the initial surface density contrast $\Delta\rho$ (Table 3.2). For a ML of depth H_{ML}, the

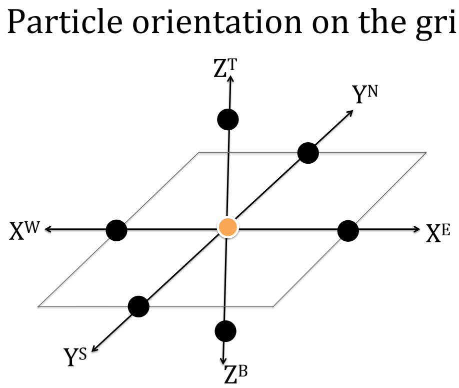

Figure 3.4: Particle positions on the model grid. Each particle has six nearest neighbors aligned along each of the cardinal directions.

deformation radius R_d can be estimated from the relation

$$R_d = \frac{M^2}{f^2} H_{ML} \ , \tag{3.5}$$

where, for a ML front aligned along the zonal direction, $M^2 = \partial b / \partial y$ is the buoyancy gradient across the front, with the buoyancy

$$b = -g \frac{\Delta \rho}{\rho_s} \ , \tag{3.6}$$

where g is the gravitational acceleration, ρ is the fluid density and ρ_s is the reference density. In the pycnocline, the deformation radius is calculated as

$$R_d = \frac{N_{max}}{f} H_{tot} \ , \tag{3.7}$$

where N_{max} is the maximum value of the buoyancy frequency and H_{tot} is the channel depth. Since the resulting instabilities in each of the experiments have different growth rates and deformation radii, the time window used to calculate the FTLEs (Table 3.2) differs accordingly to the time required for the instabilities to reach the meridional boundaries of the channel. The experiment with $\Delta\rho = 0.4$ kg m^{-3} is taken as the reference experiment. To investigate the contribution of the various components of the deformation tensor $\mathbf{D}$ to the rate of particle separation , four realizations of $\mathbf{D}$ are considered. To investigate the role of vertical velocities, the vertical displacement terms $\dfrac{\partial z_2}{\partial x_1}$ and $\dfrac{\partial z_2}{\partial y_1}$ are set to zero, leading to

$$\mathbf{D}_1(\boldsymbol{x}_1, t_1, t_2) = \begin{pmatrix} \dfrac{\partial x_2}{\partial x_1} & \dfrac{\partial x_2}{\partial y_1} & \dfrac{\partial x_2}{\partial z_1} \\ \dfrac{\partial y_2}{\partial x_1} & \dfrac{\partial y_2}{\partial y_1} & \dfrac{\partial y_2}{\partial z_1} \\ 0 & 0 & 1 \end{pmatrix} . \tag{3.8}$$

Table 3.2: Numerical experiments conducted and the time windows during which particle trajectories are computed. The experiment with $\Delta\rho = 0.4$ kgm^{-3} is considered as the reference experiment.

$\Delta\rho$	Time window (days) $[t_1, t_2]$	Deformation radii [km] ML	Deformation radii [km] Pycnocline
0.1	285 - 330	1.00	21.75
0.2	165 - 210	1.45	21.70
0.4	**60 - 80**	**2.06**	**21.55**
0.6	45 - 60	2.16	21.35
0.8	45 - 60	3.91	21.05

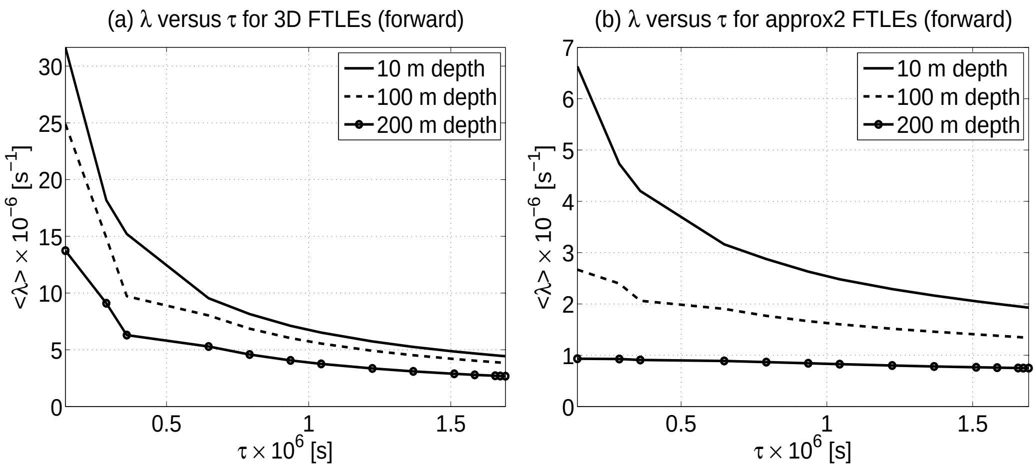

Figure 3.5: Time evolution of the area averages of (a) 3D FTLEs and (b) approx2 FTLEs at 10 m (continuous line), 100 m (dashed line) and 200 m (dot dashed line) in the reference simulation.

To deduce the contribution of vertical shear to the overall rate of particle separation, the terms $\dfrac{\partial x_2}{\partial z_1}$ and $\dfrac{\partial y_2}{\partial z_1}$ are set to zero yielding

$$\mathbf{D}_2(\boldsymbol{x}_1, t_1, t_2) = \begin{pmatrix} \dfrac{\partial x_2}{\partial x_1} & \dfrac{\partial x_2}{\partial y_1} & 0 \\ \dfrac{\partial y_2}{\partial x_1} & \dfrac{\partial y_2}{\partial y_1} & 0 \\ \dfrac{\partial z_2}{\partial x_1} & \dfrac{\partial z_2}{\partial y_1} & 1 \end{pmatrix} . \tag{3.9}$$

Setting the joint contribution of vertical displacements and vertical shear to zero, yields a reduction to a two dimensional system in which particle separation is effected only by the horizontal strain

$$\mathbf{D}_3(\boldsymbol{x}_1, t_1, t_2) = \begin{pmatrix} \dfrac{\partial x_2}{\partial x_1} & \dfrac{\partial x_2}{\partial y_1} & 0 \\ \dfrac{\partial y_2}{\partial x_1} & \dfrac{\partial y_2}{\partial y_1} & 0 \\ 0 & 0 & 1 \end{pmatrix} . \tag{3.10}$$

Finally, setting the horizontal strain and vertical displacement terms to zero, yields

$$\mathbf{D}_4(\boldsymbol{x}_1, t_1, t_2) = \begin{pmatrix} 1 & 0 & \dfrac{\partial x_2}{\partial z_1} \\ 0 & 1 & \dfrac{\partial y_2}{\partial z_1} \\ 0 & 0 & 1 \end{pmatrix} , \tag{3.11}$$

from which the contribution of vertical shear to particle separation is determined.

The resulting FTLE approximations from the above approximations of the Cauchy-Green deformation tensor will be denoted as follows

$$\text{3D FTLEs} = \frac{1}{2|\tau|}\log C , \tag{3.12}$$

$$\text{approx1 FTLEs} = \frac{1}{2|\tau|}\log C_1 , \tag{3.13}$$

$$\text{approx2 FTLEs} = \frac{1}{2|\tau|}\log C_2 , \tag{3.14}$$

$$\text{approx3 FTLEs} = \frac{1}{2|\tau|}\log C_3 , \tag{3.15}$$

$$\text{approx4 FTLEs} = \frac{1}{2|\tau|}\log C_4 , \tag{3.16}$$

where C, C_1, C_2, C_3 and C_4 are respectively the maximum of the eigenvalues of the operators $\mathbf{D}^{\mathrm{T}}\mathbf{D}$, $\mathbf{D}_1^{\mathrm{T}}\mathbf{D}_1$, $\mathbf{D}_2^{\mathrm{T}}\mathbf{D}_2$, $\mathbf{D}_3^{\mathrm{T}}\mathbf{D}_3$ and $\mathbf{D}_4^{\mathrm{T}}\mathbf{D}_4$. The absolute value ($|\cdot|$) of τ in (3.12 - 3.16) is emphasized since the sign of τ changes from being positive for forward FTLEs to negative for backward FTLEs. **Fig.** 3.8b,c show the variation of area averages of FTLEs with the integration time τ for the 3D and approx2 FTLEs respectively. The integrated values of the FTLEs are observed to converge at all depths in about 470 hours, corresponding to $\sim$ 19.6 days. Badin et al. (2011) reported that in this time, the separation of passive tracer was still exponential and thus in a chaotic advection regime. As we are interested in the statistical properties of stirring, using a shorter interval would yield a large change in the shape of the PDFs and the spectra for small changes in the interval length, while with this choice, the statistics appear to be quasi-stationary, in the limits of the time evolving flow associated with the freely decaying front.

3.3 Results

3.3.1 Eulerian fields

At the surface, MLIs are visible in the form of filaments along which the vertical component of relative vorticity and strain rate, respectively defined as

$$\xi = \frac{\partial v}{\partial x} - \frac{\partial u}{\partial y} \quad \text{and} \tag{3.17}$$

$$\mathcal{S} = \left({\mathcal{S}_n}^2 + {\mathcal{S}_s}^2\right)^{1/2} , \tag{3.18}$$

where

$$\mathcal{S}_n = \left(\frac{\partial v}{\partial x} + \frac{\partial u}{\partial y}\right) \text{ and } \mathcal{S}_s = \left(\frac{\partial u}{\partial x} - \frac{\partial v}{\partial y}\right) , \tag{3.19}$$

are respectively the normal and shear components of the strain rate, are intensified. Isolated vortices that break away from the main frontal regions are observed as regions with cores of high relative vorticity surrounded by high values of strain rate (Fig. 3.6 a, b). For example, a dipolar structure is observed in the lower left corner of the domain. While the structure appears to be an isolated vortex, closer inspection, changing for example the range of the color bar, allows to recognize its dipolar nature. In the channel interior, the filamentary structures disappear leaving regions with diffused values of vorticity and strain rate (Fig. 3.6 d,e). The existence of these non-zero regions of vorticity and strain rates underlying regions with intense action of MLIs confirms findings of previous studies that MLIs can penetrate into the pycnocline where they may be important for the lateral mixing of tracer (e.g., Badin et al., 2011). Another Eulerian diagnostic quantity, the Okubo-Weiss (OW) parameter ω (Okubo, 1970; Weiss, 1991), which is essentially a measure of the relative strength between the strain rate $\mathcal{S}$ and the relative vorticity ξ defined as

$$\begin{aligned} \omega &= \mathcal{S}^2 - \xi^2 , \\ &= \S^2 + 4\left(\frac{\partial u}{\partial y}\frac{\partial v}{\partial x} - \frac{\partial u}{\partial x}\frac{\partial v}{\partial y}\right) = \S^2 - 4\det(\nabla_{\mathrm{h}}\mathbf{u}) , \end{aligned} \tag{3.20}$$

where

$$\S = \nabla_{\mathrm{h}}\mathbf{u} = \frac{\partial u}{\partial x} + \frac{\partial v}{\partial y} , \quad \text{and} \quad \det(\nabla_{\mathrm{h}}\mathbf{u})$$

are the horizontal flow divergence and determinant of the velocity gradient tensor respectively. The expression of the OW parameter in the form of (3.20) reveals that it contains information about the horizontal divergence of the flow (e.g., Provenzale, 1999; Petersen et al., 2006; Mensa et al., 2013) making it thus an ideal diagnostic for out-of-balance motions (Molemaker and McWilliams, 2005) such as the those arising due to MLIs.

The OW parameter identifies vortical structures as vorticity dominated cores (with $\xi > \mathcal{S}$) surrounded by regions of high strain rate (with $\xi < \mathcal{S}$). Filamentary structures are however difficult to characterize from the OW parameter field, since both their vorticity and strain rate are intensified, yielding regions with alternating positive

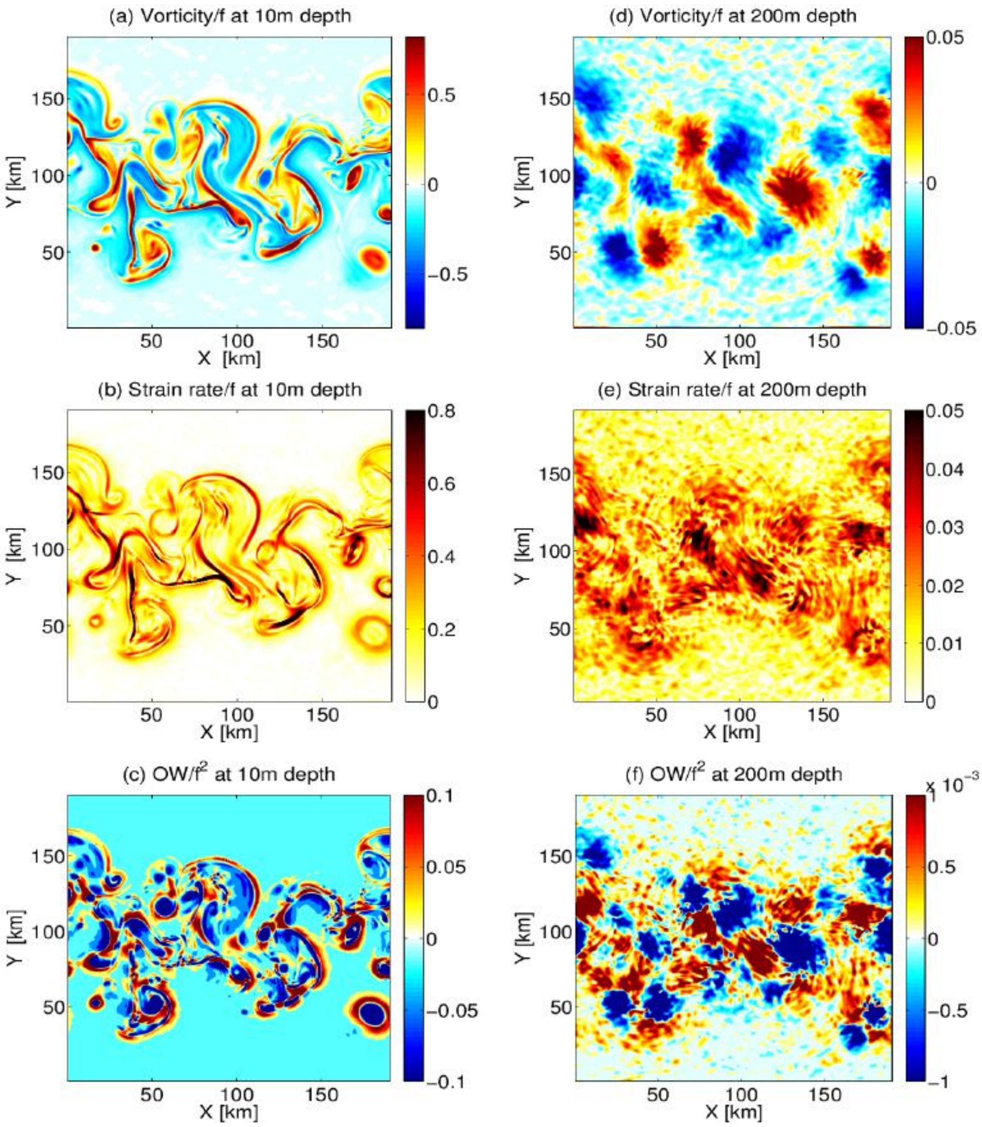

Figure 3.6: Left column: Normalised (a) relative vorticity (b) strain rate and (c) OW parameter at 10 m depth computed at day 60. Right column: normalised (d) relative vorticity, (e) strain rate and (f) OW parameter at 200 m depth computed at day 60.

and negative values of the OW parameter (Fig. 3.6c). One example is given by the surface ageostrophic filament extending at $x \sim 40$ km and $y \sim 40-90$ km, which has a strong signature in both the vorticity and strain rate fields, but that disappears in the OW field (Fig. 3.6a,b,c).

Another important aspect in the evaluation of the performance of diagnostic quantities of flow coherence is objectivity. A flow diagnostic is considered objective if it is independent of the frame of the observer thus yielding similar results under time dependent rotations and translations (e.g., Truesdell and Noll, 2004). Objectivity is a test that many coherent structure detection algorithms fail and has thus been a subject of recent and ongoing research (see Peacock et al., 2015, and references therein). The OW parameter, like the relative vorticity and strain rate are all not objective (e.g., Haller, 2005; Ouellette, 2012) and thus yield inconsistent coherent structures under coordinate transformations. While heuristic non objective measures of flow coherence are often easy to compute, they may yield both false positive and false negatives in the frame under consideration (e.g., Haller, 2011), thereby mis-representing the dynamical coherence of the flow. The issue of false flow coherence becomes more difficult in diagnosing flows for which the correct coherent structures are not a priori known (see Haller, 2015, for further discussion). The non objectivity and failure to detect filaments by the Eulerian fields is further motivation for the choice to adopt a Lagrangian approach in studying the stirring properties of MLIs.

3.3.2 Finite Time Lyapunov Exponents

Comparison of Fig. 3.7 and Fig. 3.6 shows that the forward 3D FTLE fields have a much more complex structure than the Eulerian fields at all depths. Isolated vortices are characterized by high values of FTLEs on both their interior and boundaries. The reason for the presence of regions with high values of FTLEs within the vortices is due to the unbalanced nature of the vortices, which have a spiraling structure associated to the divergence of the flow, resulting in a fine FTLEs structure also in their interior.

Filaments in the main frontal region are instead characterized by regions with high values of FTLEs alternating with regions of low values of FTLEs in a very fine structure. This shows that in the frontal region, characterized by an interplay of MLIs and their filamentary structures, secondary instabilities act to fold, stretch and entangle the Lagrangian structure of turbulence. Eventually, for times longer than the integration time used, the FTLEs would merge to create a chaotic region. Noticeable, stirring is much more complex than revealed by Eulerian measures. 3D FTLEs are finer at the ML base than at the surface (Fig. 3.7b), with filaments and vortex boundaries with a more distinct appearance. In the channel interior, filamentary structures are detected by the FTLE field in locations where the Eulerian fields are rather featureless (Fig. 3.7c). The different appearance of the FTLEs at the sea surface from the FTLEs at base of the ML and in the interior is related to the fact that at depth the flow is weaker and thus acts to tangle less the FTLEs, with the entanglement decreasing at depth with the strength of the flow.

The horizontally averaged 3D FTLEs (Fig. 3.8a, black line) show that the 3D FTLEs have larger values in the ML, with a local maximum in the middle of the ML, in agreement with the observation from numerical simulations that MLIs produce stronger fluxes in the middle of the ML (Fox-Kemper et al., 2008), and have a fast decrease below the ML base, showing however non zero values at all depths. Analysis of the vertical structure of horizontally averaged forward FTLEs from the different approximations (Fig. 3.8a) shows that 3D (black line), approx1 (black dotted line) and approx4 (gray dot dashed line) FTLEs are indistinguishable at all depths. The same result holds for approx2 (gray line) and approx3 (gray dotted line) FTLEs, which are coincident at all depths, indicating that the vertical velocity does not play a significant role in determining the size of FTLEs, but that the magnitude of the

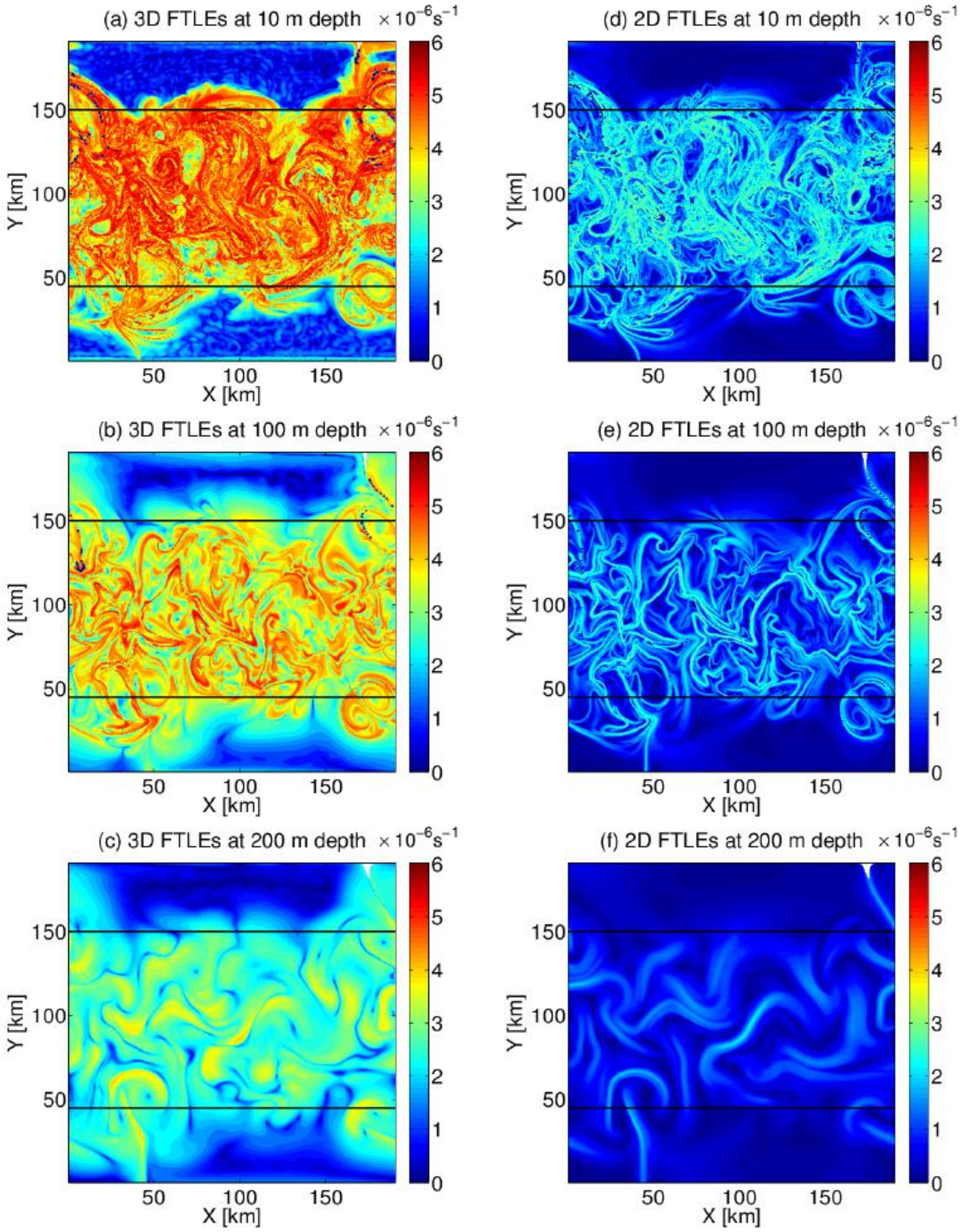

Figure 3.7: Forward 3D FTLEs (left column) and forward 2D FTLEs (right column) at depths of 10 m (a,d), 100 m (b, e) and 200 m (c, f) in the reference simulation at day 60. The black horizontal lines demarcate the region for which further analysis of FTLEs is considered.

FTLEs is dominated by the vertical shear. The analysis of the vertical structure of horizontally averaged FTLEs from the different approximations for the backward integration (Fig. 3.8b) yields the same results as the forward integration.

Due to the coincidence of the 3D, approx1 and approx4, as well as of approx2 and approx3 FTLEs, in the remaining only the results from 3D and approx2 FTLEs will be presented, with the approx2 FTLEs henceforth referred to as 2D FTLEs.

2D FTLEs show ridges, which in first approximation are defined as local maxima (and minima of the negative) of the FTLE field, in the same location of the ridges of the 3D FTLEs field (Fig. 3.7 d,e,f). The ridges found for the 3D and 2D cases are in the same location as they are associated to the local intensification of vertical shear and horizontal strain, which are in turn associated to the localized ageostrophic instabilities. Note that the ridges of the FTLEs do not denote LCSs, as it is now recognised that ridges have non zero flux across them (Haller, 2015). The values of the 2D FTLEs are however about half of the values of the 3D FTLEs. Further, the 2D FTLEs seem to show a smaller degree of entanglement of the FTLE field in the frontal region. The large difference in the size of FTLEs along locations of maximal and weak stretching of fluid patches yields well defined FTLE fields at all depths. Vortex boundaries, narrow regions separating dipoles of vortices and frontal structures are characterized by large values of FTLEs (Fig. 3.7f).

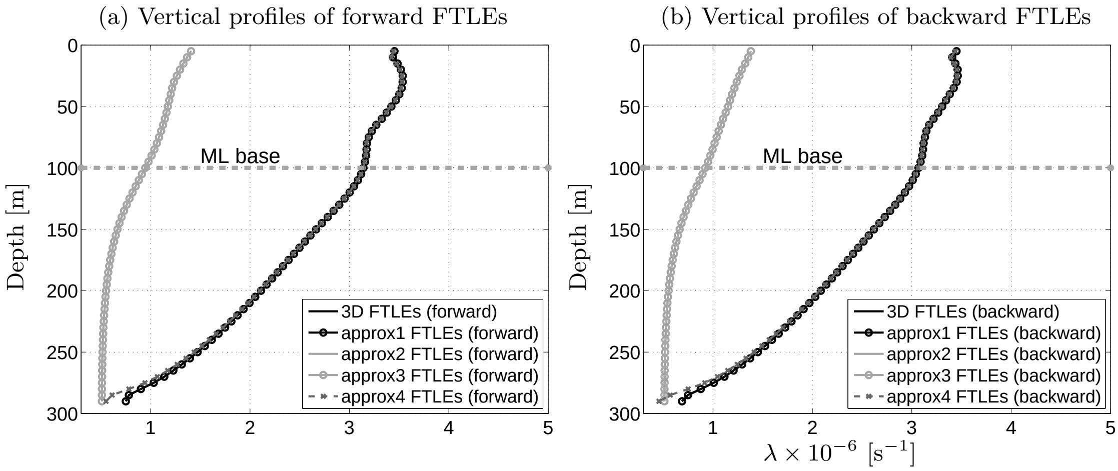

Figure 3.8: Vertical profiles of the averaged (a) forward FTLEs and (b) backward FTLEs for the different approximations of FTLEs in the reference simulation at day 60. Thin dashed gray line represents the mixed layer base at 100 m depth.

The vertical profiles of 2D FTLEs reveal that in addition to only being approximately half the values of 3D FTLEs, 2D FTLEs are surface intensified while their values quickly decrease below the ML (Fig. 3.8a). This surface intensification of 2D FTLEs is also revealed by the observation that, for all τ, the difference between the area averaged 2D FTLEs at different depths are larger than the difference between the area averaged 3D FTLEs at different depths (Fig. 3.5a,b). At 200 m depth, the values of 2D and 3D FTLEs have reduced by $\sim 80\%$ and $\sim 40\%$ of their respective values at the ML base (Fig. 3.8a). The slow decrease of 3D FTLE values from the base of the ML to the channel interior, shows that the vertical shear is able to sustain high rates of particle separation at depth.

3D FTLEs are thus able to "penetrate" in the channel interior, filling the volume of the channel (Fig. 3.9) where they show curtain-like structures that form the template for stirring in the channel. These curtain-like structures have also been found in previous studies that have considered 3D (Lekien et al., 2007) and quasi 3D velocity fields (Bettencourt et al., 2012). Further, area averages of forward in time

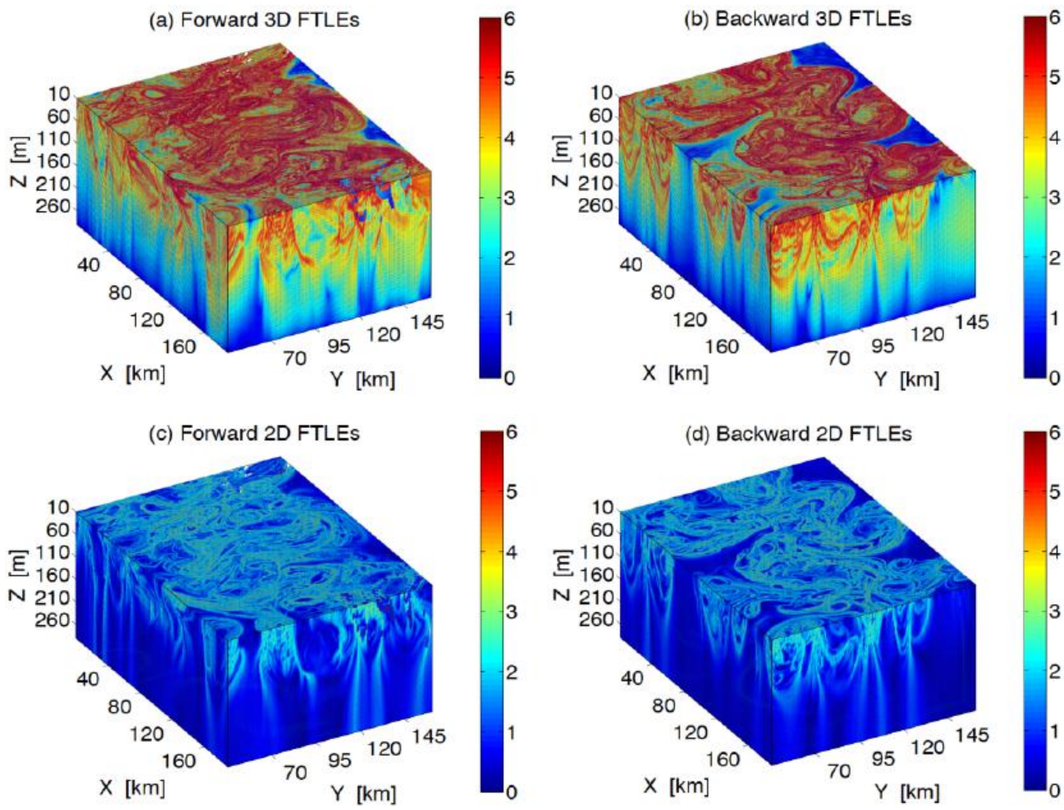

Figure 3.9: Left column: Forward in time (a) 3D and (c) 2D FTLEs. Right column: Backward in time (b) 3D and (d) 2D FTLEs. All quantities have units of $10^{-6}\mathrm{s}^{-1}$. Only the region shown between black lines in Fig. 3.7 is presented.

FTLEs are found to exhibit values comparable to their corresponding backward in time FTLE approximations at all depths (not shown). It should be noted however that the forward and backward FTLEs have been calculated using different initial conditions, so no comparison between the backward FTLEs, which are calculated in the time interval $[t_2, t_1]$, and the Eulerian fields, which are defined at time t_1, should be attempted.

The relationship between the local value of the FTLEs and the vertical shear suggests the existence of a scaling relationship between the two quantities, which will be studied next.

3.3.3 Scaling relationship between the FTLEs and the vertical shear

Consider a system in geostrophic and hydrostatic balance, so that the thermal wind relation

$$\frac{\partial \mathbf{U}_g}{\partial z} = \frac{g}{f\rho_s}\hat{k} \times \nabla\rho \ , \tag{3.21}$$

holds, where $\mathbf{U}_g$ is the geostrophic current and g is the graviational acceleration. Approximating the derivatives using finite differences, (3.21) yields

$$\Lambda_i = \frac{\Delta\ \mathbf{U}_g}{\Delta z}\Delta t = \frac{g\Delta t}{f\rho_s \Delta x_i}\left(\Delta\rho\right) \ , \tag{3.22}$$

where Δt is the time step of integration for the particle trajectories. Further, considering the flow gradient tensor in general terms as

$$\boldsymbol{\nabla} F_{t_1}^{t_2} \approx \begin{pmatrix} \Gamma_1 & \Gamma_2 & \Lambda_1 \\ \Gamma_3 & \Gamma_4 & \Lambda_2 \\ \omega_1 & \omega_2 & 1 \end{pmatrix} \ , \tag{3.23}$$

where Γ_i and ω_i are the components of the horizontal shear of the horizontal and vertical currents multiplied by Δt, respectively. The corresponding Cauchy-Green strain tensor (2.12) takes the form

$$\boldsymbol{\Delta} \approx \begin{pmatrix} \mathcal{A} & \mathcal{D} & \mathcal{E} \\ \mathcal{D} & \mathcal{B} & \mathcal{F} \\ \mathcal{E} & \mathcal{F} & \mathcal{C} \end{pmatrix} \ , \tag{3.24}$$

where,

$$\begin{aligned} \mathcal{A} &= \Gamma_1^2 + \Gamma_3^2 + \omega_1^2 \ ; \quad & \mathcal{D} &= \Gamma_1\Gamma_2 + \Gamma_3\Gamma_4 + \omega_1\omega_2 \ ; \\ \mathcal{B} &= \Gamma_2^2 + \Gamma_4^2 + \omega_2^2 \ ; \quad & \mathcal{E} &= \Gamma_1\Lambda_1 + \Gamma_3\Lambda_2 + \omega_1; \\ \mathcal{C} &= \Lambda_1^2 + \Lambda_2^2 + 1 \ ; \quad & \mathcal{F} &= \Gamma_2\Lambda_1 + \Gamma_4\Lambda_2 + \omega_2 \ ; \end{aligned} \tag{3.25}$$

The characteristic equation of the tensor $\boldsymbol{\Delta}$ in (3.24) is

$$(\mathcal{A}-\sigma)\left[(\mathcal{B}-\sigma)(\mathcal{C}-\sigma) - \mathcal{G}^2\right] - \mathcal{D}\left[\mathcal{D}(\mathcal{C}-\sigma) - \mathcal{F}\mathcal{E}\right] + \mathcal{E}\left[\mathcal{D}\mathcal{F} - \mathcal{E}(\mathcal{B}-\sigma)\right] = 0 \ , \tag{3.26}$$

where σ_i are the sought eigenvalues. In what follows, different approximations of the parameters in (3.25) are made that lead to the FTLE realizations made earlier in (3.13 - 3.16). For all approximations, except for approx4, we assume $\Gamma_i = \Gamma,\ \Lambda_i = \Lambda,\ \omega_i = \omega$.

- If $\omega = 0$ and the other terms in (3.23) are retained, we recover approx1. The solutions of the characteristic equation (3.26) are $[0, 4\Gamma^2, 2\Lambda^2 + 1]$.
- Assuming that $\omega \neq 0$, $\Lambda = 0$, yields approx2. The solutions of the characteristic equation are thus $[0, 1, 4\Gamma^2 + 2\omega]$.
- Assuming $\omega = 0,\ \Lambda = 0$, yields approx3. The solutions of the characteristic equation are $[0, 1, 4\Gamma^2]$.
- Finally, assuming $\Gamma_1 = \Gamma_4 = 1$, $\Gamma_3 = \Gamma_2 = \omega = 0$, yields approx4. The solutions of the characteristic equation are $[1, 1, 2\Lambda^2 + 1]$.

In geophysical flows, $\Lambda >> \Gamma$, so that the maximum eingenvalue of approx1 and approx4 is the same and corresponds to $2\Lambda^2 + 1$. Since $2\omega^2 \ll 4\Gamma^2$, approx2 and approx3 also yield he same maximum eigenvalue, that is $4\Gamma^2$.

This explains why the numerically computed values of FTLEs are similar for approx1 and approx4 (hereafter called $\lambda_{3\mathrm{d}}$) and for approx2 and approx 3 (hereafter called $\lambda_{2\mathrm{d}}$), as visible from Fig. 3.8d. In summary,

$$\lambda_{3\mathrm{d}} \sim \frac{1}{2\tau} \log\left(2\Lambda^2 + 1\right) , \tag{3.27}$$

$$\lambda_{2\mathrm{d}} \sim \frac{1}{2\tau} \log\left(4\Gamma^2\right) . \tag{3.28}$$

A comparison of the magnitudes of the $\lambda_{3\mathrm{d}}$ and $\lambda_{2\mathrm{d}}$ yields

$$\frac{\lambda_{3\mathrm{d}}}{\lambda_{2\mathrm{d}}} \sim \log_{4\Gamma^2}\left(2\Lambda^2 + 1\right), \tag{3.29}$$

so that $\lambda_{3\mathrm{d}} \geq \lambda_{2\mathrm{d}}$ if $2\Lambda^2+1 \geq 4\Gamma^2$. The vertical profiles of the horizontally averaged $2\Lambda^2 + 1$ and $4\Gamma^2$ are shown in Fig. 3.10, which shows that indeed $2\Lambda^2 + 1 \geq 4\Gamma^2$ at all depths, from which $\lambda_{3\mathrm{d}} \geq \lambda_{2\mathrm{d}}$ holds.

Substituting (3.22) in (3.27) leads to,

$$\lambda_{3\mathrm{d}} \sim \frac{1}{2\tau}\log\left[2\left(\frac{g\Delta t}{f\rho_s \Delta x_i}\right)^2 (\Delta\rho)^2 + 1\right] . \tag{3.30}$$

Equation (3.30) gives a scaling law between the local FTLEs and the nonlocal density contrast used to initialize the ML front.

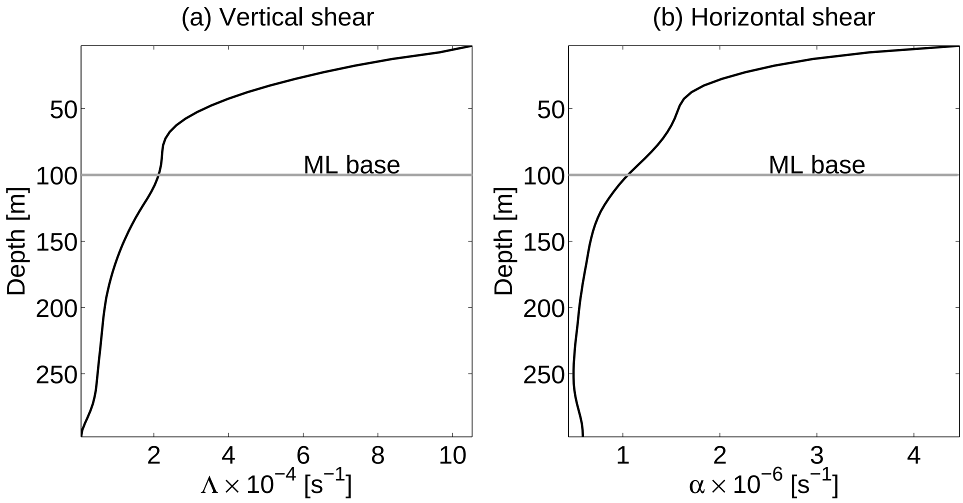

Figure 3.10: Vertical profiles of the (a) vertical and (b) horizontal shears at day 60 in the reference simulation. The thick gray line indicates the mixed layer base at 100 m depth.

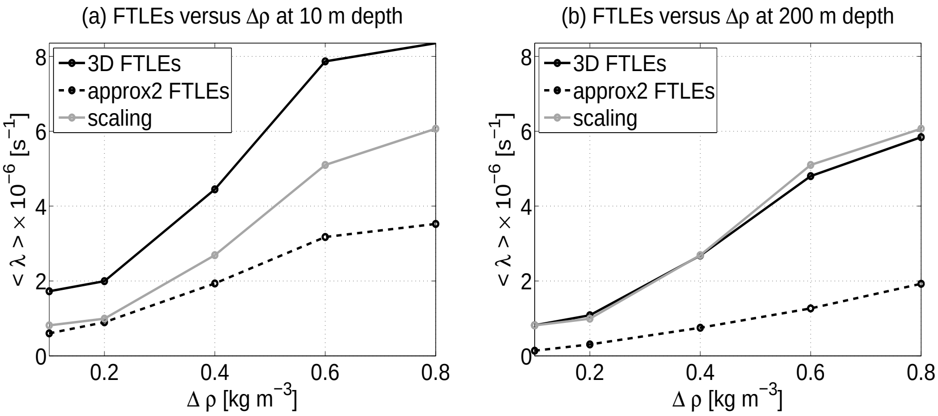

Figure 3.11: Area average of FTLEs versus $\Delta\rho$ for 3D (continuous black line) and approx2 (dashed black lines) FTLEs at the depth of (a) 10 m and (b) 200 m. In gray, the same quantity is shown as derived from the scaling law (3.30).

It should be noted that the scaling relation here proposed can be reinterpreted as a relationship between the slope of tracer filaments and the density contrast $\Delta\rho$. Considering a tracer filament with concentration φ, the aspect ratio between the horizontal and vertical scales of a tracer filament under the action of horizontal strain and vertical shear, for long time scales yields (Haynes and Anglade, 1997; Haynes, 2001)

$$\frac{\partial\varphi/\partial z}{\nabla_{\mathrm{h}}\varphi} \sim \frac{\Lambda}{\Gamma} \ , \tag{3.31}$$

where $\nabla_{\mathrm{h}} = \mathbf{i}\partial/\partial x + \mathbf{j}\partial/\partial y$. The same result was found by Smith and Ferrari (2009) only assuming a forward potential enstrophy cascade. In this case,

$$\frac{\partial\varphi/\partial z}{\nabla_{\mathrm{h}}\varphi} \sim \frac{N}{f} \ , \tag{3.32}$$

holds (Charney, 1971), as observed in high resolution quasi geostrophic simulations and confirmed from observations of passive tracer dispersion in the North Atlantic (Smith and Ferrari, 2009). In the current case,

$$\frac{\partial\varphi/\partial z}{\nabla_{\mathrm{h}}\varphi} \sim \frac{\Delta x_i}{\Delta z} \sim \frac{\alpha}{f}\Delta\rho \ , \tag{3.33}$$

that can be reduced to (3.32) assuming, without loss of generality, a filament aligned in the zonal direction and using the relationship, valid for the ML (Tandon and Garrett, 1994, 1995; Young, 1994)

$$\left(\frac{1}{f}\frac{\partial b}{\partial y}\right)^2 \sim \frac{\partial b}{\partial z} = N^2 \ . \tag{3.34}$$

The domain integrated values of the FTLEs λ as a function of $\Delta\rho$ shows that, in the ML, the scaling law lies between the 3D and approx2 FTLEs (Fig. 3.11a), while it converges to the values of the 3D FTLEs in the pycnocline (Fig. 3.11b). The large discrepancy between the prediction of the scaling law and the numerical 3D FTLEs in the surface layers is explained by the fact that in the ML, the particle trajectories are dominated by ageostrophic velocities, which are not captured by the thermal wind balance approximation considered in (3.21). The discrepancy is larger for large values of $\Delta\rho$, corresponding to MLIs with higher values of Rossby numbers and enhanced vertical transport. In the pycnocline instead, the ageostrophic component of the flow is weak yielding a convergence of the scaling law to the 3D FTLEs.

3.3.4 FTLEs Statistics

Ridges emerging from backward FTLEs represent regions to which fluid parcels converge and which are advected by the flow (e.g., Shadden et al., 2005; Mathur et al., 2007; Lekien et al., 2007). It is then possible to consider the backward FTLEs as proxies for a conservative passive tracer, with the FTLE values corresponding to the tracer concentration. Under this assumption it is interesting to look at the backward FTLEs statistics, namely the probability distribution functions (PDFs) and the wavenumber spectra, in order to characterize the behavior of the FTLEs. In particular, current parameterizations of passive tracer dispersion by mixed layer instabilities assume the validity of downgradient diffusive schemes (Fox-Kemper et al., 2008), which in turn would imply a Gaussian distribution for the passive tracer, with a Eulerian power spectra following a power law k^{-1}, where k is the horizontal wavenumber. While a Gaussian distribution is not expected to hold for the backward FTLEs, it is interesting to calculate their statistics and to compare them between the 3D and 2D case, in order to establish the role of 3D stirring in the distribution of passive tracers. All the quantities are calculated for the region of the domain where the instabilities are well developed, shown as the region enclosed by black lines in Fig. 3.7.

Probability Distribution Functions

The PDFs of the backward FTLEs calculated for different values of τ show convergence in time, in agreement with the convergence in time of the horizontally averaged FTLEs (Fig. 3.12). The PDFs of the backward 3D FTLEs at 10 m depth, show large deviations from the Gaussian distribution calculated with the same mean and standard deviation, exhibiting positive values of skewness and long tails toward lower FTLE values (Fig. 3.12a). In comparison, the Gaussian distribution would yield a zero value of skewness. The PDFs are also characterized by low values of kurtosis. In comparison, the Gaussian distribution would yield a value of kurtosis of 3. The PDFs of the backward 3D FTLEs (Fig. 3.12b) show a ”shouldering” structure (Beron-Vera et al., 2008), which is indicative of a mixed phase space structure of the flow with different attractors and in which different regions experience non uniform stirring rates from the instabilities. While the different shoulders are insufficient to qualify the PDFs of 3D FTLEs as multimodal (e.g., Szezech et al., 2005; Harle and Feudel, 2007), they point to the fact that the stirring in the domain is nonhomogeneous. The deviation from the Gaussian distribution at 10 m depth is visible also in the PDFs of the 2D FTLEs (Fig. 3.12b), which show non zero values of skewness and relatively flat peaks corresponding to values of kurtosis larger than 3 (Fig. 3.12d).

The analysis of the vertical profiles of the skewness and kurtosis of the PDFs of the backward FTLEs, reveals that the distributions of FTLEs are non Gaussian at all depths (Fig. 3.13). In particular, the skewness of the 3D FTLEs (black lines) shows local maxima at the sea surface and in the pycnocline, and a local minimum within the ML. The skewness of the backward in time 2D FTLEs (gray line) shows instead negative values in the ML, increasing to positive values in the interior, with the zero crossing line corresponding to depths just beneath the base of the ML.

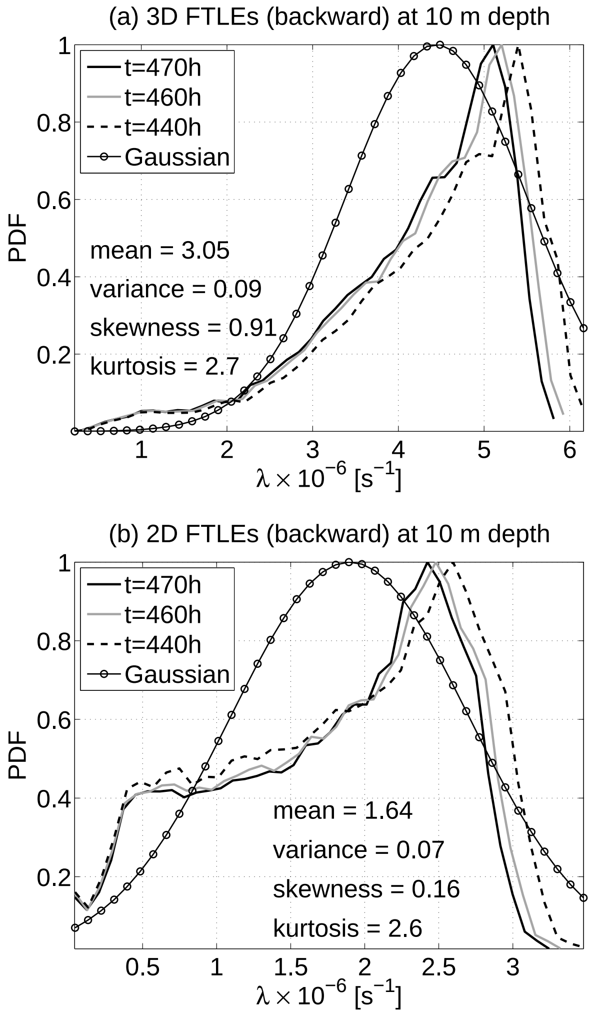

Figure 3.12: PDFs of (a) 3D and (b) 2D FTLEs calculated with backward in time integration at 10 m depth. The FTLEs are calculated using particle integration times of 440 hours (dashed lines), 460 hours (full gray lines) and 470 hours (full black lines). Dotted lines represent the Gaussian distributions with the same mean and standard deviation of the PDFs calculated with the particle integration time of 470 hours.

Negative skewed PDFs, as observed in Fig. 3.12 at 10 m depth, reveal that most locations in the flow domain experience rates of particle separation greater than the observed average value, with the latter case reflecting a relatively more vigorous stirring influence of the flow. The skewness profiles in Fig. 3.13a show thus that the full 3D stirring leads to higher stirring at all depth than inferred from the 2D and other approximations. The relatively distinct ridges of the 2D FTLE approximations, particularly in the ML, are reflective of this distribution in which most of the particles experience low stirring rates while a few of them (that lie along ridges) experience higher rates of stirring hence larger values of FTLEs.

The kurtosis of the 3D FTLEs (Fig. 3.13b, black line) shows values that are lower than 3 at all depth, corresponding to PDFs that are more peaked than the Gaussian

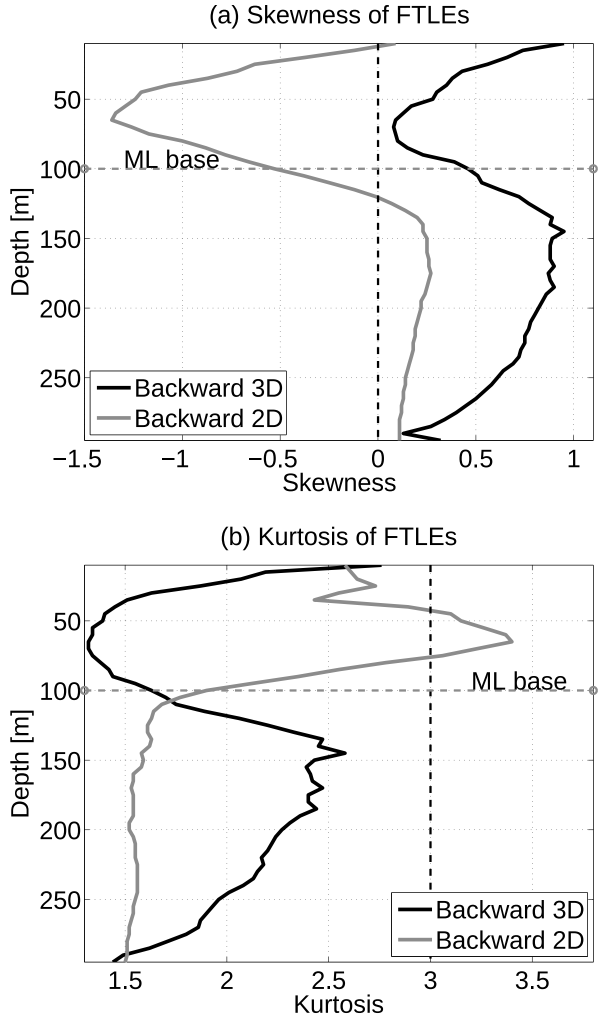

Figure 3.13: (a) Vertical profiles of the third order moment (skewness) of the PDFs of backward in time 3D FTLEs (black line) and 2D FTLEs (gray line) at day 60 in the reference simulation. The skewness of the Gaussian distribution, equal to zero is shown as a thin black line. (b) Vertical profiles of the fourth order moment (kurtosis) of the PDFs of the backward in time 3D FTLEs (black line) and 2D FTLEs (gray line). The kurtosis of the Gaussian distribution is 3 (thin black line).

distribution. A local minimum is observed at the center of the ML and local maxima are observed at the sea surface and within the pycnocline. The kurtosis of the backward in time 2D FTLEs (gray line) shows instead a very different distribution, taking values larger than 3 within the ML, but lower values at the sea surface and in the pycnocline. The low values of kurtosis of PDFs imply that the distributions are relatively flat near the mean value, and thus there is no single dominant phase but an interwining of multiple phases that contribute to the overall particle separation. In contrast, PDFs with higher values of kurtosis would imply the existence of a dominant phase in a pool of other relatively weaker ones.

Non symmetric PDFs, skewed toward low FTLE values have been observed also in previous studies of 2D FTLEs (e.g., Abraham and Bowen, 2002; Voth et al., 2002; Beron-Vera and Olascoaga, 2009; Waugh et al., 2012; Harrison and Glatzmaier, 2012).

FTLEs Spectra

Considering the backward FTLEs as a passive tracer, it is interesting to look at the slopes of the tracer variance, in order to characterize if they show a local or nonlocal behavior. In particular, considering a Eulerian wave number spectra of kinetic energy,

$$E(k) \sim k^{-\alpha} \ , \tag{3.35}$$

and the corresponding tracer spectra $T(k)$, local dynamics are characterized by $1 \leq \alpha < 3$, for which the tracer spectra shows a

$$T(k) \sim k^{\frac{\alpha-3}{2}-1} \ , \tag{3.36}$$

dependence (e.g., Bennett, 1984). In this regime, the dispersion of particles is dominated by the action of instabilities with size comparable to the separation of the particles. The particular case $T(k) \sim k^{-2}$ is characteristic of frontal dynamics. For nonlocal dynamics, $\alpha \geq 3$ and $T(k) \sim k^{-1}$.

The wavenumber spectra are calculated in the zonal direction, i.e. along lines of constant latitude, and then averaged. As for the PDFs, the calculation is performed only in the region occupied by the MLIs, shown between black lines in Fig. 3.7.
In the ML, the kinetic energy (KE) spectra shows slopes of $\alpha = 3$ at scales smaller than the first baroclinic deformation radius, and much steeper slopes at submesoscale, which are thus dominated by dissipation (Fig. 3.14a). Both the 3D and 2D backward FTLEs spectra show a -1 slope at all scales (Fig. 3.14b,c), which is in agreement with the slope of the KE spectra and which is a signature of local dispersion created by the mesoscale instabilities. Slopes at smaller scales should instead be interpreted carefully, as at these scales the finite resolution of the model and the numerical dissipation prevent the possible formation of an inertial range. Notice that the 3D and 2D FTLEs spectra display the same pattern of peaks, as a direct consequence of the fact that 3D and 2D FTLEs have ridges in the same locations.

In the pycnocline, the kinetic energy spectrum at scales below the first baroclinic deformation radius shows an inertial range with slope of $\alpha = 3$, or steeper (Fig. 3.14d). Analysis of the spectra for the backward in time 3D FTLE field reveals however slopes of $\sim$ -2 at 200 m depth (Fig. 3.14e). The 2D FTLE field at 200 m depth reveals also a $\sim$ -2 slope at scales smaller than the first baroclinic deformation radius, until $\sim$ 10 km, and steeper slopes at smaller scales (Fig. 3.14f). The spectra slopes of -2 correspond to frontal structures and are in agreement with results from observations from different basins of the World Ocean which show similar slope (e.g., Ferrari and Rudnick, 2000; Cole et al., 2010; Cole and Rudnick, 2012; Callies and Ferrari, 2013; Kunze et al., 2015) or even less steep (Klymak et al., 2015) both at the surface and in the ocean interior. Spectra slopes of -2 were found also from high resolution numerical simulations of the California Current System (Capet et al., 2008).

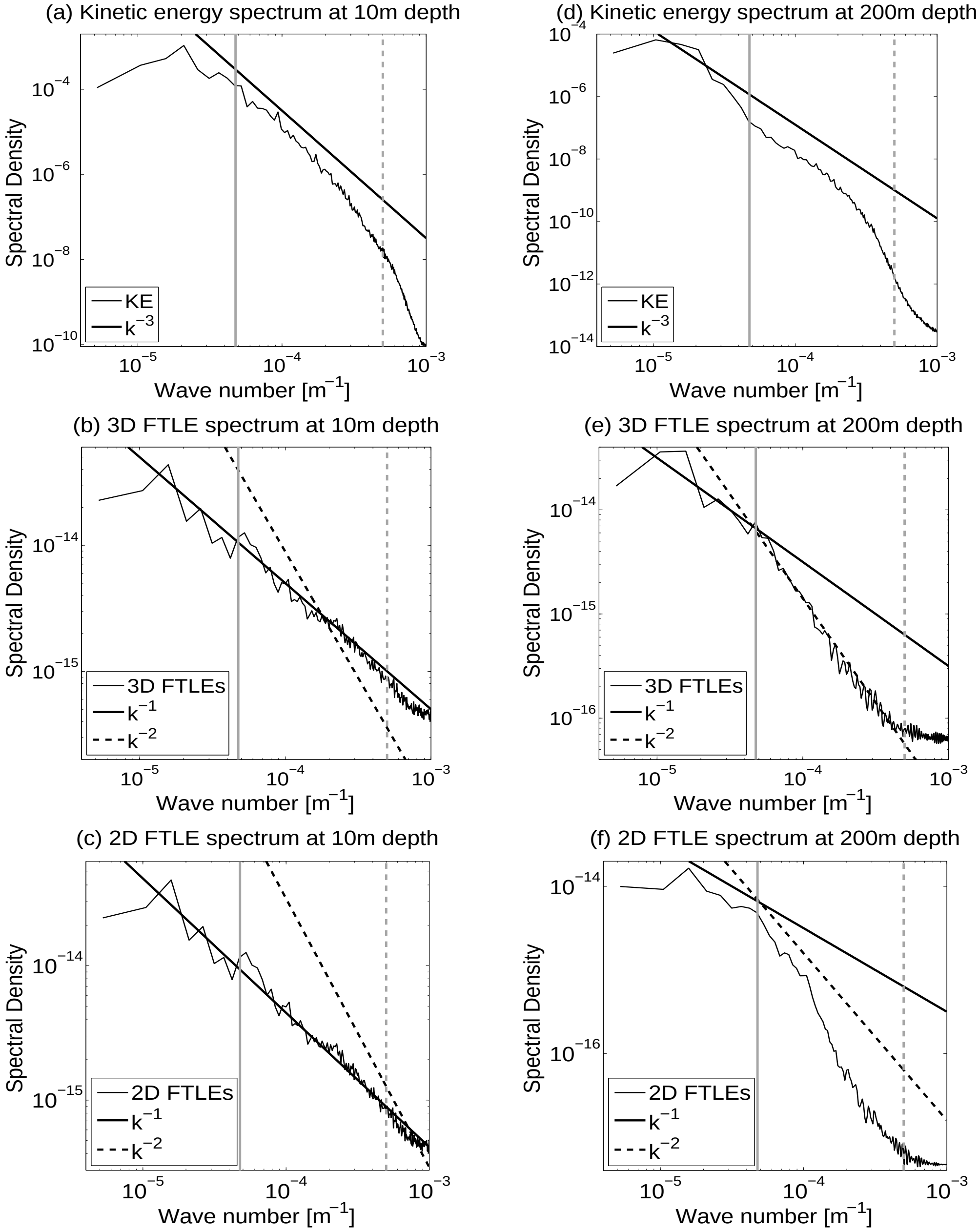

Figure 3.14: Spectra of (a,d) Kinetic energy, (b,e) backward in time 3D FTLEs and (c,f) backward in time 2D FTLEs at 10 m and 200 m depth respectively. The value of the first baroclinic deformation radius (R_d) in the reference simulation is ∼2.06 km (broken gray lines) in the ML and ∼21 km (continuous gray lines) in the pycnocline.

The spectra suggest that the passive tracer, here characterized from backward in time FTLEs, retains a -2 slope, characteristic of frontal structures (Boyd, 1992), also at depth, in agreement with the observation that MLIs are able to penetrate in the underlying pycnocline, where they are responsible for horizontal mixing, as observed in numerical simulations by Badin et al. (2011) and in the analytical and semi-analytical solution of Badin (2013) and Ragone and Badin (2016). It should be noted that this interpretation is challenged by the observations of kinetic energy spectra by Callies et al. (2015), which suggest instead the predominance of balanced dynamics. Callies et al. (2015) do not, however, examine tracer spectra. Satisfactory scientific explanations on what gives rise to the -2 slope for tracer spectra in the interior are still missing.

The -1 slope in the wavenumber spectra at 10 m depth is comparable with the results by Beron-Vera and Olascoaga (2009), which found the same slope, representative of local diffusion, at the sea surface. The transition between -1 slope close to the sea surface to -2 slope at depth can be explained considering that close to the sea surface the flow is more energetic and is responsible for a stronger entanglement of the FTLEs, which results in a larger variance of FTLEs at smaller scales. At depth, FTLEs are less entangled and the spectra displays a smaller variance at small scales.

It should be noted that the comparison between the results of this study and the results found from observations or from numerical simulations with realistic geometry and forcing is however only of qualitative nature, due to the lack of forcing in the setting here considered.

3.3.5 Scale dependence of stirring

To further characterize the adiabatic mixing in the ocean interior created by MLIs we have calculated the Finite Size Lyapunov Exponents (FSLEs) (Aurell et al., 1997; Artale et al., 1997), which are calculated using the expression in (2.18). Equation (2.18) should be compared with (2.17). In (2.18), γ is a fixed separation between particles with initial separation δ, and $\tau(\delta)$ is the time required to attain this separation. The analysis of FSLEs has been successfully applied to the study of stirring and turbulence in the atmosphere (e.g., Joseph and Legras (2002)) and in the ocean (d'Ovidio et al., 2004, 2009; Garcia-Olivares et al., 2007; Schroeder et al., 2011, 2012; Özgökmen et al., 2012; Griffa et al., 2013; Mensa et al., 2013).

FSLEs are closely related to metrics from information theory and they do not only measure the predictability time of the dynamics at different spatial scales, but also measure the degree of randomness and information content (Gaspard and Wang, 1993; Costa et al., 2005). Further, they can give an information for the evolution of the fluctuations for non-infinitesimal perturbations (Aurell et al., 1997). For a review on FSLEs, see Cencini and Vulpiani (2013).

As FSLEs show a dependence on the largest Lyapunov exponent for small initial separation and a decay of the FSLEs with a power law corresponding to a diffusive behavior of the particles for larger initial scales of separation (Artale et al., 1997; Boffetta et al., 2000), they can be used to characterize dynamics that possess a multi-scale nature. This is reflected in the resulting dispersion regimes, with the chaotic advection regime (or "Lyapunov regime"), which is obtained for particle separation which is smaller than the separation of the flow features responsible for the dispersion, characterized by constant λ_s; the Richardson regime (Richardson, 1926), which is obtained for particle separation which is comparable to the separation of the flow features responsible for the dispersion, characterized by $\lambda_s \sim \delta^{-2/3}$; and the diffusive regime, which is obtained for particle separation which is larger than the separation of the flow features responsible for the dispersion, characterized by $\lambda_s \sim \delta^{-1}$ (Artale et al., 1997; Boffetta et al., 2000).

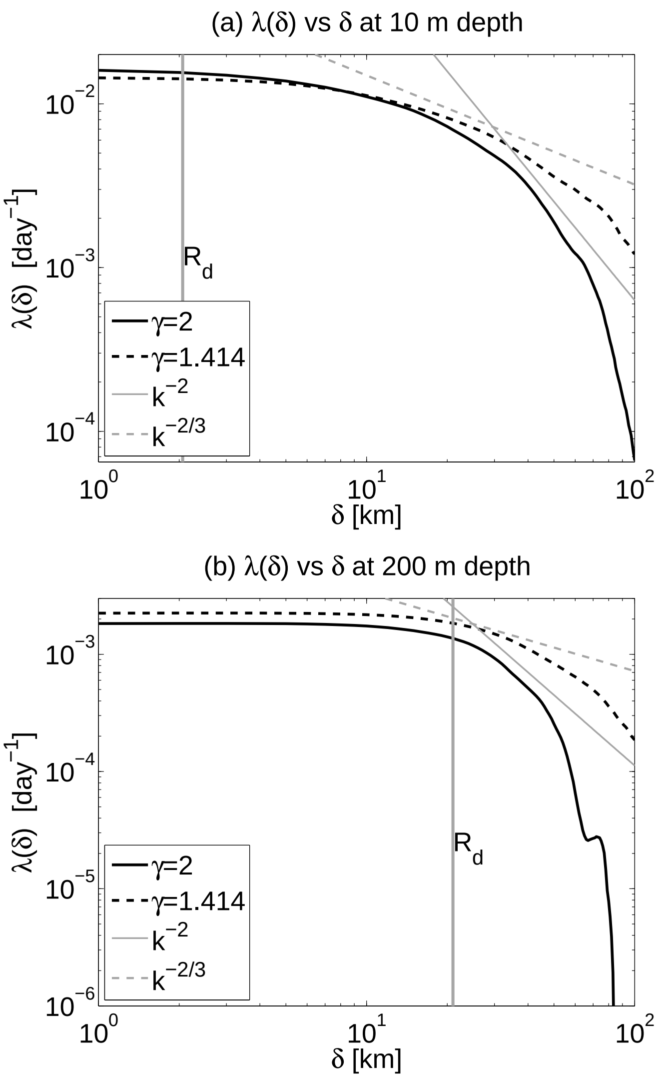

Figure 3.15: FSLEs as a function of the initial separation δ of the particles at (a) 10 m and (b) 200 m depth. Black full and dashed line indicate threshold separations of $\gamma = 2$ and $\gamma = \sqrt{2}$ respectively. Lines with slope $-2/3$ and -2, corresponding to the Richardson and diffusive regime respectively, are reported in gray for comparison. Vertical gray lines indicate the deformation radius.

An alternative regime for scales smaller than the typical size of oceanic eddies was proposed by Özgökmen et al. (2012), which suggested that if submesoscale eddies are responsible for local transport, at these scales λ_s is not constant but shows an increasing trend as the scale decreases, which is also named “Hypothesis II” (in contraposition to “Hypothesis I”, corresponding to the Lyapunov regime). While FSLEs seem to be unable to capture LCSs (Karrasch and Haller, 2013), in this

Section they will be used to study the scale dependence of chaotic advection.

The domain averaged value of λ_s as a function of the initial separation of the particles δ at the depth of 10 m is shown in Fig. 3.15a. The value of λ_s was calculated from the 2D FSLEs using the two standard values of $\gamma = \sqrt{2}$ (dashed line) and $\gamma = 2$ (full line), which corresponds to separation doubling between the particles. As suggested by Boffetta et al. (2000), different values of γ can be used to detect different regimes.

The dependence of λ_s on δ at 10 m depth shows a decay of the values of λ_s for scales larger than the deformation radius (Fig. 3.15a). The threshold value of $\gamma = \sqrt{2}$ yields a signature of a Richardson regime between $\sim$ 10 km and $\sim$ 30 km, followed by a diffusive regime at larger scales, detected by the threshold $\gamma = 2$. For scales larger than $\sim$ 30 km, the dependence of λ_s on δ shows a saturation, with values of λ_s rapidly decreasing as δ increases. For scales smaller than the deformation radius, both values of γ suggest the presence of a Lyapunov regime. It should be noted that due to the small size of the deformation radius, we are left with not enough points to make a correct assessment of the lack of a "Hypothesis II" regime in the ML.

At 200 m depth, the dependence of λ_s on δ shows signature of a Richardson regime between the deformation radius and $\sim$ 30 km, and a diffusive regime between $\sim$ 30 km and $\sim$ 60 km. At larger scales, the trend shows a saturated regime. This result is in agreement with the results found by Badin et al. (2011) using passive tracers, which observed a Richardson regime until $\sim$ 40 km within the pycnocline. For scales smaller than the deformation radius, instead, no "Hypothesis II" regime is visible, suggesting that, despite the fact that MLIs are able to excite mixing in the interior, they do not give a local signature in the dispersion regime.

3.3.6 Lagrangian Coherent Structures

The chaotic stirring acting on the passive tracer and described in the previous sections is determined by the skeleton of the turbulence underlying the flow. In order to characterize this skeleton of the turbulence, we proceed in calculating the LCSs of the flow under consideration. In the current study, we compute hyperbolic and elliptic LCSs along two dimensional horizontal surfaces implemented with the LCS Tool - a geodesic LCS detection software for two dimensional unsteady flows (Onu et al., 2015). The integration of stretch and strain line LCSs in (2.29) is terminated when the arclength parameter $r \geq 50$ km in order to ensure a good resolution of the emerging structures. Due to limitations in the computational resources, the LCSs are calculated using the velocity field with 3 hours output, i.e. with a much coarser time resolution than the previous computation, which instead made use of a 15 minutes output.

The results for the extraction of the LCSs at 10 m are shown in Fig. 3.16a and, in doubled resolution for the region demarcated between the black lines in Fig. 3.16a, in Fig. 3.16b. Red, blue and green lines indicate respectively Repelling, Attracting and Elliptic LCSs. The FTLEs field is indicated with gray shades. Notice that, due to the different time resolution of the velocity field, the FTLEs field appears smoother than in Fig. 3.7. Frontal structures are observed to be delineated by a complex combination of Repelling and Attracting LCSs, from which a dense network of LCSs spreads over the surrounding regions. The frontal region is also characterized by a web of heteroclinic connections, which form the skeleton of the chaotic flow. As noted from previous studies, the relation between ridges of the FTLE field and the LCSs computed from the variational theory is not one-to-one, although ridges of FTLEs may indicate a nearby LCS (Haller, 2011; Beron-Vera et al., 2013). While ridges of the FTLE field capture most of the important flow features (especially when computed at high resolution (Fig. 3.16b)), it is important to note that the parameterized LCSs offer a more complex structure that cannot be deduced from the ridges of the FTLE field. It should also be noted that the hyperbolic LCSs are dependent on the spatial resolution, with a more convoluted and intricate network of hyperbolic LCSs emerging at higher resolution, with a higher correlation between the FTLE ridges and the hyperbolic LCSs emerging.

Elliptic LCSs that delineate vortex boundaries, obtained for $\lambda = 1$, are represented as closed green curves. Repelling and Attracting LCSs have been truncated so as to start from the boundaries of the elliptic LCSs. The analysis of the Elliptic LCSs confirms the presence of the dipolar structure detaching from the ML front in the lower left corner of the domain, and of another elliptic structure detached from the frontal region in the lower right side of the domain.

Also in the pycnocline, a complex web of Repelling and Attracting LCSs emerges from the flow. Several regions are observed to be ”spreading centres” of Repelling and Attracting LCSs. Future work will have to determine if these centres evolve into isolated vortices as the flow evolves. The tendency of the geodesically extracted LCSs to predict and reveal flow features and dynamics that are not observed from FTLE fields, allows for a deeper understanding of the Lagrangian skeleton of turbulence

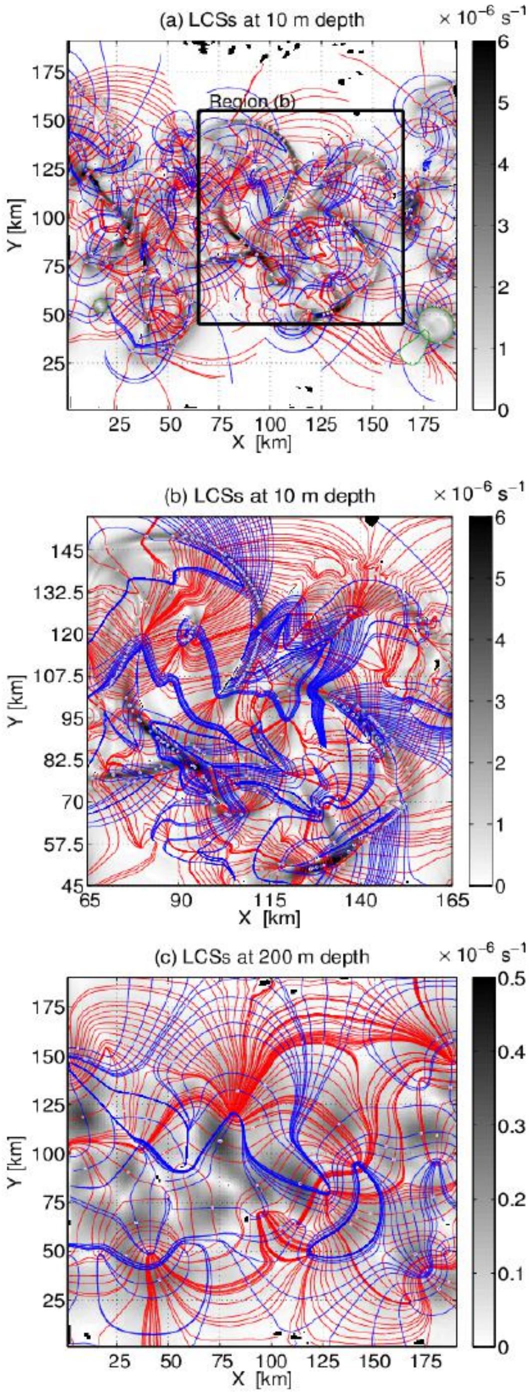

Figure 3.16: (a) Repelling (red), Attracting (blue) and Elliptic (green) LCSs computed from day 60 to day 80 for the reference run. 2D FTLEs computed for the same period are shown in the background as gray shades. (b) 2D FTLEs and geodesic LCSs in the region demarcated in a black square in panel (a) are computed at double resolution. (c) 2D FTLEs and geodesic LCSs at 200 m depth.

(Mathur et al., 2007; Peacock and Haller, 2013; Beron-Vera, 2015). This Lagrangian skeleton leads to the formation of ordered patterns in the flow, and its understanding requires more than the identification of curves of maximal fluid trajectory separation.

3.4 Summary and Discussion

In this Chapter, the 3D FTLEs of ML instabilities have been characterized. Results show that the structure and size of the 3D FTLEs are determined predominantly by the vertical shear of horizontal velocities. 3D FTLE fields exhibit a complex distribution in which high rates of particle separation are not just confined to regions along filaments and vortex boundaries, but are also found in the regions surrounding these high activity features. Regions that are rather quiescent, as observed from Eulerian fields, reveal a complex structure of FTLEs, confirming findings of previous studies which show that a regular flow pattern can yield chaotic particle trajectories (e.g., Aref, 1984; Ottino, 1990b; Aref, 2002; Wiggins, 2005). The complexity of the 3D FTLEs field resembles the multifractal distribution of FTLEs found from observations of chaotic stirring by Abraham and Bowen (2002). Further, the vertical shear is found to sustain high rates of particle separation in the domain interior. As a consequence, 3D FTLEs decrease slower with depth than 2D FTLEs, which are instead found to be surface intensified and to decrease quickly in magnitude in the pycnocline. It should be noted that 3D and 2D FTLEs display the same spatial distribution of ridges.

The dominating role of vertical shear in the magnitude of the FTLEs is a direct consequence of the nature of MLIs, which is characterized by a stratified and rotating flow in a quasi-balanced state and in which vertical velocities, although larger than their corresponding mesoscale instabilities, is still approximately three orders of magnitude smaller than the horizontal velocities. Analysis of other oceanic flows in which vertical velocities might play an important role, such as coastal upwelling regions, in which vertical velocities are one order of magnitude smaller than the horizontal velocities, reveals a still dominating effect of vertical shear (Bettencourt et al., 2012). It would be interesting to extend the analysis here proposed to other kind of flows, such as idealized flows (e.g., Pratt et al., 2013; Rypina et al., 2015) Langmuir turbulence (e.g., Van Roekel et al., 2012), in which vertical velocities are comparable to the horizontal velocities and the emerging turbulence is no longer quasi two dimensional.

The observation that 3D FTLEs are dominated by vertical shear allows to determine a scaling relation between the amplitude of the FTLEs and the initial density contrast of the ML front. While this relationship well agrees with the values of the 3D FTLEs in the interior of the domain, in the ML it shows a deviation from the simulations, which can be attributed to the presence of ageostrophic ML instabilities.

Backward in time FTLEs can be considered as proxies to a conservative passive tracer, with the FTLE values corresponding to the tracer concentration. Under this assumption it is possible to compare the FTLEs statistics with the statistics expected from passive tracers. PDFs of both 3D and 2D FTLEs are found to be non Gaussian at all depths exhibiting non zero values of skewness and relatively low values of kurtosis. 3D FTLES are skewed toward higher FTLE values with long tails toward low values of FTLEs, while PDFs of 2D FTLEs are instead skewed toward low values of FTLEs with long tails toward higher values of FTLEs. Wavenumber spectra show a slope of -2 in the pycnocline, corresponding to frontal structures and in agreement with results from observations made in various basins of the world ocean, reporting similar spectra slopes for tracers both in the ML and inside the pycnocline(e.g., Ferrari and Rudnick, 2000; Cole et al., 2010; Cole and Rudnick, 2012; Callies and Ferrari, 2013; Kunze et al., 2015; Klymak et al., 2015). The lack of Gaussianity and the slopes of the spectra confirms the observation that the FTLEs possess elongated frontal shapes. Using the backward in time FTLEs as proxies for passive tracers, the lack of Gaussianity poses a constraint for the use of diffusive parametrizations, which constrain the stirring effect of MLIs within the ML (Fox-Kemper et al., 2008).

By computing FSLEs at different spatial resolutions, the scale dependence of the stirring effected by MLIs has been studied. With the amplification factor $\gamma = \sqrt{2}$ at the surface, a Richardson regime is observed for distances between 10 and 30 km, while a diffusive regime is observed at large scales with the amplification factor $\gamma = 2$. For scales larger than 30 km, λ rapidly decreases for increasing values of δ and eventually saturates. At scales smaller than the deformation radius, a Lyapunov regime is observed for both $\gamma = \sqrt{2}$ and $\gamma = 2$. In the channel interior, λ shows signature of a Richardson regime between the deformation radius and ~ 30 km, and a diffusive regime between ~ 30 km and ~ 60 km. At larger scales, the trend shows a saturated regime. At scales smaller than the deformation radius, λ is found to be saturated thus yielding no "Hypothesis II" regime (Özgökmen et al., 2012). Absence of a "Hypothesis II" regime implies that although MLIs propagate into the channel interior, they are unable to yield a local signature in the particle dispersion regimes.

Finally, LCSs are calculated using the variational theory which allows for a distinction between elliptic (e.g vortices) and hyperbolic (e.g filaments) LCSs. Isolated vortices are identified as elliptic LCSs from which a complex web of ALCSs and RLCSs emerge. The entanglement of ALCSs and RLCSs is more complex in the ML due to the large stretching and folding of fluid elements from the MLIs. At high resolution, more hyperbolic LCSs are observed. In the pycnocline, several regions are observed as spreading centres of ALCSs and RLCSs. It is also observed that the relation between LCSs and FTLE ridges is not a one-to-one, which is in agreement with previous studies (e.g., Haller, 2011) which have reported that FTLE ridges may show LCSs in locations where they don't exist and conceal them in locations where they exist. The observed complex structures of LCSs associated to MLIs can be important for the characterization of mixing and the transfer of nutrients and other passive tracers in the ocean surface, as well as provide the landscape for the growth of different phytoplankton species (d'Ovidio et al., 2010).

Chapter 4

Realistic Ocean Simulation

In this chapter, an analysis of the ocean dataset (hereafter called the parent dataset) obtained from a realistic numerical simulation of the Atlantic Ocean is presented. Two case study areas are chosen: one in the North Eastern region of the Atlantic ocean, capturing part of the North Atlantic drift current (e.g., Fofonoff, 1981) and another in the relatively low activity central Atlantic Ocean. We perform the same analysis as for the idealised simulations using velocity fields of the two case study regions and compute FTLEs following the methodology in Chapter 3.2. By analysing the time series of both Eulerian and Lagrangian diagnostics of the flow for four years (i.e 2006, 2007, 2010 and 2011), we study the seasonality of submesoscale turbulence in the two contrasting case study regions.

4.1 Model set-up

A simulation of the Atlantic Ocean north of 33° S, including the Mediterranean Sea, Nordic seas and the Arctic Ocean was conducted using the Massachusetts Institute of Technology general circulation model (MITgcm) in hydrostatic mode (Marshall et al., 1997a,b). The MITgcm was run with a horizontal spatial resolution of $\Delta x = \Delta y \sim 4$ km corresponding to a resolution of 1/24° at the equator. The vertical resolution is $\Delta z = 5$ m in the topmost 40 levels and increase linearly with depth for a total of 100 levels. The model bottom topography, which is realistic in this simulation, is extracted from the 2-Minute Gridded Global Relief Data [ETOPO2] (Smith and Sandwell, 1997). At the ocean surface, the model is forced with momentum and buoyancy fluxes obtained by using bulk formula and the atmospheric state of the ECMWF/ERA-Interim reanalysis (Dee et al., 2011). Parameterization of vertical mixing is implemented with a K- profile parameterization (KPP) formulation (Large et al., 1994), with background coefficients of vertical viscosity and diffusivity respectively set at 10^{-4} m^{2}s^{-1} and 10^{-5} m^{2}s^{-1}. For horizontal viscosity, the biharmonic coefficient was set at 3×10^9 m^{4}s^{-1}. Since biased spurious trends are known to emerge in long temporal integrations, the ocean surface salinity is relaxed to the monthly climatological values of the World Ocean Atlas 2005 (see Boyer et al., 2005).

To allow for a quick spin up of the model, the initial conditions in the parent simulation are selected as the output of the final state of a similar simulation initialised by the World Ocean Atlas (Boyer et al., 2005) and integrated at 8 km resolution for

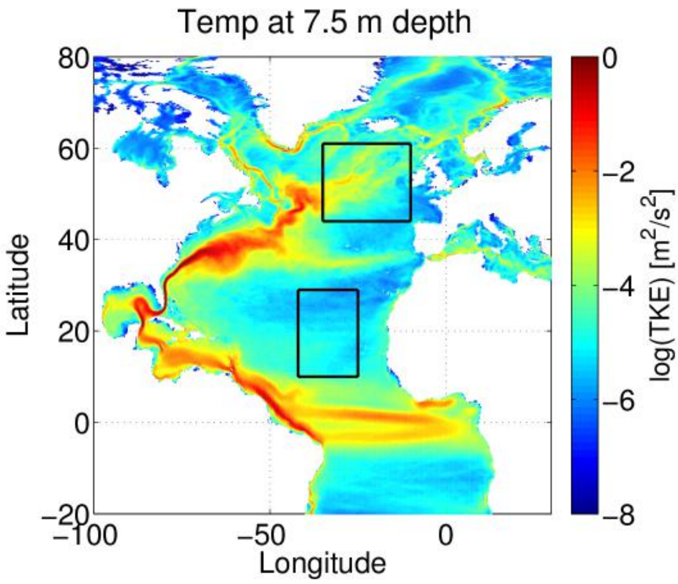

Figure 4.1: Total kinetic energy in the Atlantic ocean at the 7.5 m depth in logarithmic scale, averaged for the period between 2003 and 2011 . The dashed boxes enclose the case study regions.

the period 1948 to 2003. The parent simulation is then integrated for a period of 10 years starting 2002 to 2011, with fields being written at a daily frequency. For a more detailed description of the parent simulation, see Section 2.2 of Sena-Martins et al. (2015).

4.1.1 Case study regions

In this thesis, we use temperature, salinity and velocity fields from the above parent simulation in two case study areas, namely;

- A region in the North Eastern Atlantic Ocean bounded between latitudes 44° N and 61° N and between longitudes 35° W and 09° W (Fig. 4.1), which also encloses part of the Northern branch of the Gulf Stream, the North Atlantic drift, which crosses to Western and Northern Europe (e.g., Luyten, 1977; Stommel, 1958a,b). The energetic surface circulation in this region maintains a significantly strong flow in the ocean interior, characterised by meanders and a net flow towards the northeastern part of the domain (Fig. 4.2 a,b).
  The region also has rough topography at the bottom with depths varying between 300 m in the northeastern part to $\sim$ 5 km in the southwestern part of the domain (Fig. 4.3a).

- A relatively low eddy activity region in the Central Atlantic Ocean bounded by latitudes 10° N and 29° N and between longitudes 42° W and 25° W (see Fig. 4.1). This region encloses part of the southern branch of the Subtropical gyre, namely, the North Equatorial current that recirculates off the west coast of Africa (e.g., Fofonoff, 1981). The net flow on the ocean surface in this region is toward the West and it becomes stronger with increasing distance from the west coast of Africa. However, the net flow in the ocean interior is weak, and

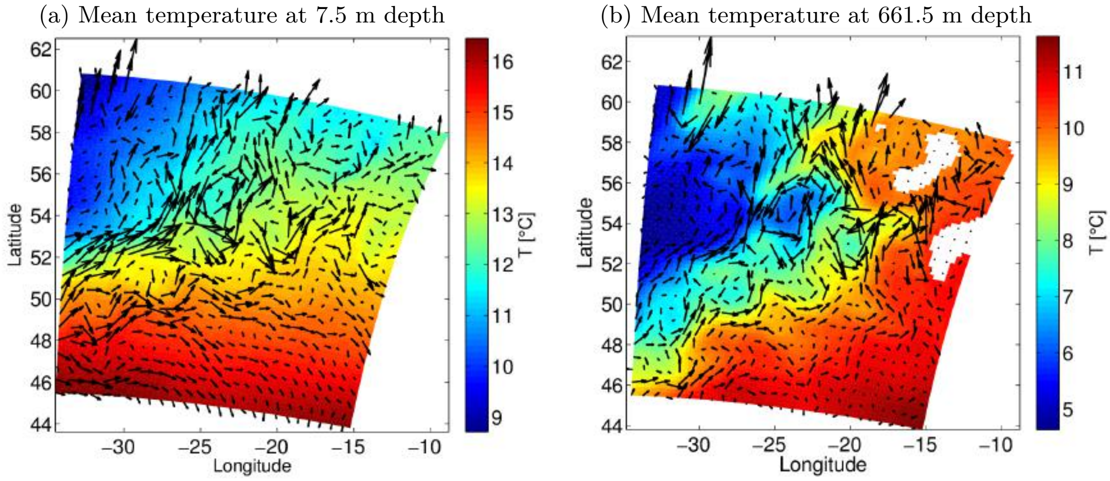

Figure 4.2: Ten year average temperature field for the region in the North East Atlantic ocean. Vectors show the horizontal velocity field, which is characterised by several meanders and a net flow towards the North East.

does not show a dominant direction (Fig. 4.4 a,b). The topography of the region is largely flat with depths varying between $\sim$ 4 km and 5.5 km (Fig. 4.3b).

Velocity fields for the above two study regions shown in Fig. 4.1 for the years 2006, 2007, 2010 and 2011 were extracted from the parent dataset. Since the current study aims at understanding the stirring influence of MLIs and their associated chaotic advection, the study concentrates only on the topmost 60 levels, equivalent to a total depth of $\sim$ 1 km from the ocean surface. With the extracted velocity fields, particle trajectories are obtained following the same procedure described in Chapter 3.2 and the different FTLE approximations calculated as for the idealised simulations, with integration time $\tau = 15$ days. In what follows, results of the simulation for the

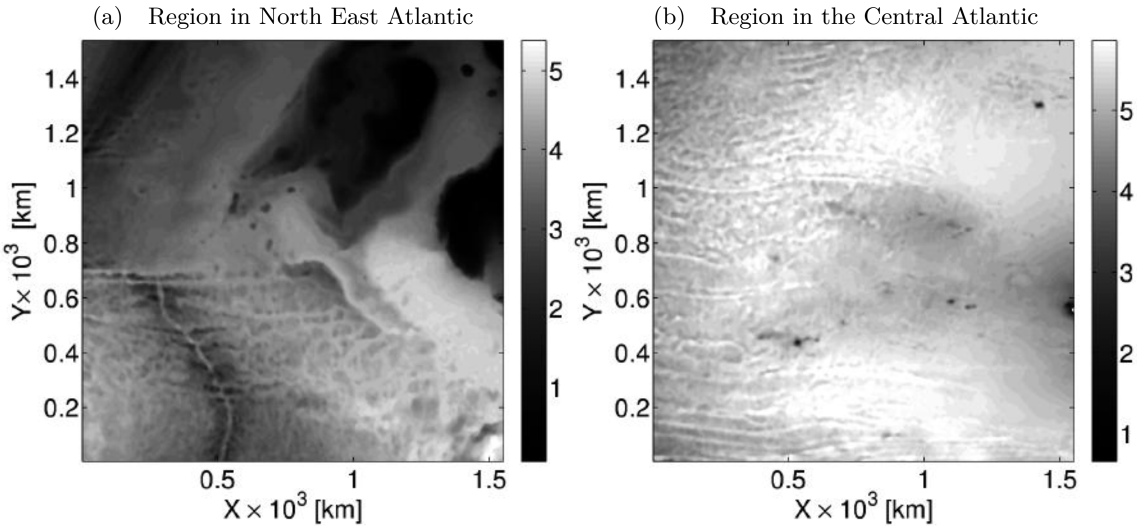

Figure 4.3: Topography of the case study regions. (a) region in the North East Atlantic ocean (b) region in the Central Atlantic ocean. Colorbars are in units of km.

(a) Mean temperature at 7.5 m depth (b) Mean temperature at 661.5 m depth

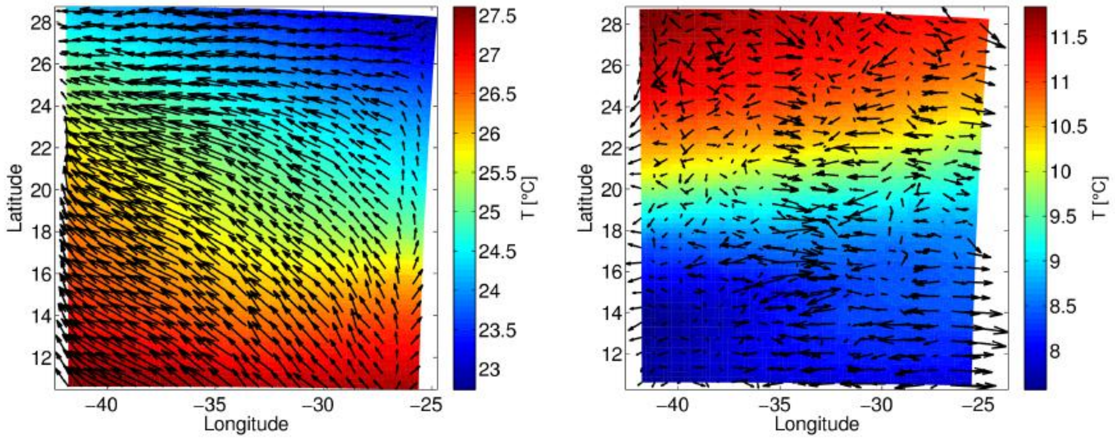

Figure 4.4: Ten year average temperature for the region in the Central Atlantic ocean. Vectors show the horizontal velocity field orientation, which is towards the North West at the ocean surface.

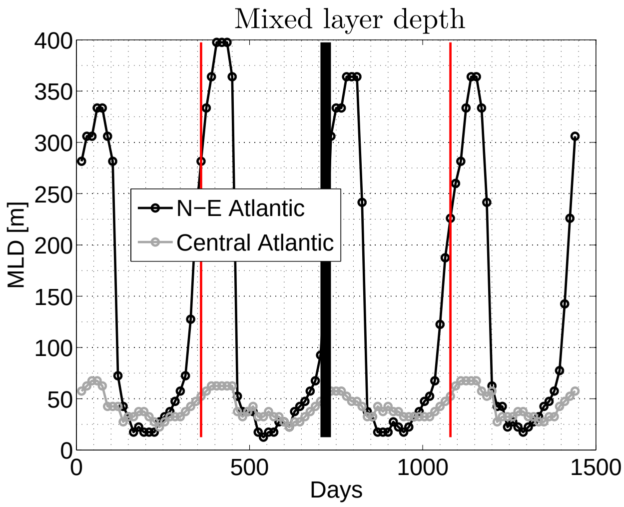

Figure 4.5: Time series of the mixed layer depth for the region in the North East Atlantic Ocean (dotted black line) and the region in the Central Atlantic ocean (dotted gray line). Red lines separate the different years and the thick vertical black line emphasizes the jump between the year 2007 and 2010.

year 2011 will be presented for the two case study regions discussed above whose primary distinguishing feature is the mixed layer depth (MLD). We here define the

	North East Atlantic		Central Atlantic	
	Winter	Summer	Winter	Summer
Rd_{ML} [km]	12	5	14	8.8
Rd_{tot} [km]	16	21	74	76

Table 4.1: Mixed layer and pycnocline Rossby radii of deformation for the case study regions, calculated for both winter and summer seasons.

MLD as the depth at which the ocean water temperature deviates from its surface value by 0.5°C (e.g., Sasaki et al., 2014; Thompson et al., 2016). Other criteria of determining the MLD such as, the depth at which the water density deviates from its surface value by 0.03 kg m^{-3} (e.g., Mensa et al., 2013), yield approximately similar results. For the region in the North East Atlantic ocean, the MLD ranges between 20 m in summer and 400 m in winter, while for the region in the Central Atlantic ocean, the MLD varies between 20 m in summer and 80 m in winter (Fig. 4.5). Further, variations in MLD during winter and summer seasons lead to different deformation radii for the two seasons, which are computed here using (3.7). The deformation radii for winter and summer seasons in the two case study regions are shown in Table 4.1. The spatial resolution of the numerical model (which is $\sim$ 4 km), does not allow the visualization of submesoscale features for which the deformation radius is of the same size or slightly higher, for the region in the northeast Atlantic ocean. In the central Atlantic ocean, the ML deformation radii for winter and summer are also low ($\leq$ 14 km) and thus no submesoscale MLIs can be resolved. The pycnocline deformation radius is however large enough to enable the resolution of pycnocline submesoscale features.

4.2 Results: North Eastern Atlantic Ocean

Figure 4.6 presents snapshots of normalised Eulerian fields: the relative vorticity, strain rate and Okubo-Weiss parameter at 7.5 m (left column) and 660 m (right column) depth calculated during winter, specifically for day 90 [i.e end of March] of the year 2011. Vortices are noticed to be characterised by regions with cores of

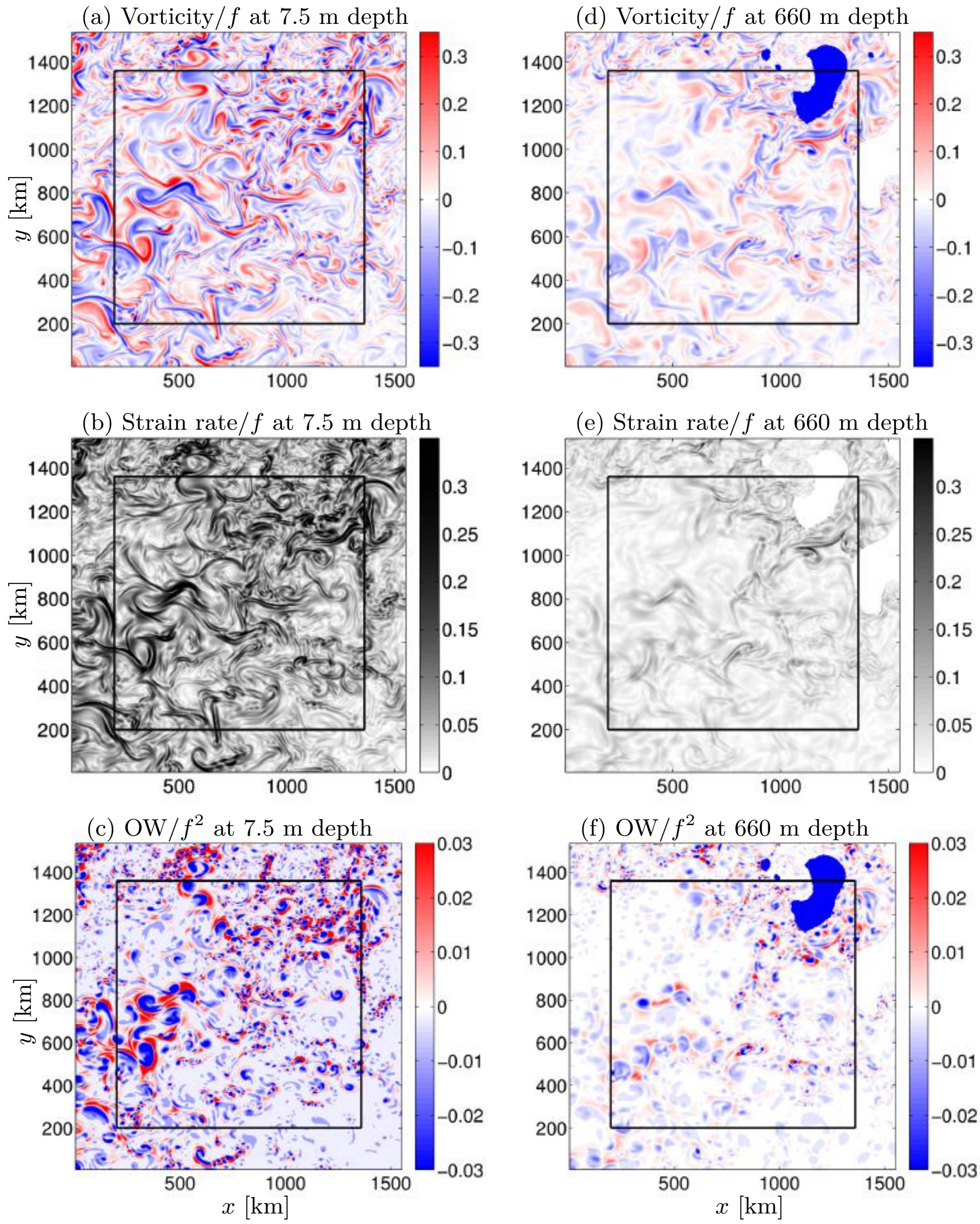

Figure 4.6: Normalised Eulerian fields evaluated at day 90 [end of March] of the year 2011 in the North Eastern Atlantic Ocean. Left column: (a) relative vorticity (b) strain rate and (c) OW parameter at 7.5 m depth . Right column: (d) relative vorticity, (e) strain rate and (f) OW parameter at $\sim$ 660 m depth.

intensified relative vorticity surrounded by large values of strain rate. Filaments are instead shown by regions along which vorticity and strain rate are simultaneously intensified (Fig. 4.6 a, b). It is also noticed that the flow in this region exhibits features over a broad range of scales, with vortices whose radii range between 30 to hundreds of kilometres and filaments which are a few kilometres thick. Regions of strain arising mostly from the interaction of mesoscale vortices manifest themselves as filaments with differing length scales and strength. An outstanding region with a rich submesoscale field is the region in the North Eastern part of the domain which encompasses part of the North Atlantic Drift, showing a large number of submesoscale vortices [i.e with radius of $\mathcal{O}(10)$ km] and high intensity filaments.

In the domain interior, a decrease in the number of small scale features with radii of $\mathcal{O}(20)$ km is noticed, leaving only mesoscale vortices (Fig. 4.6 d,e). This is in

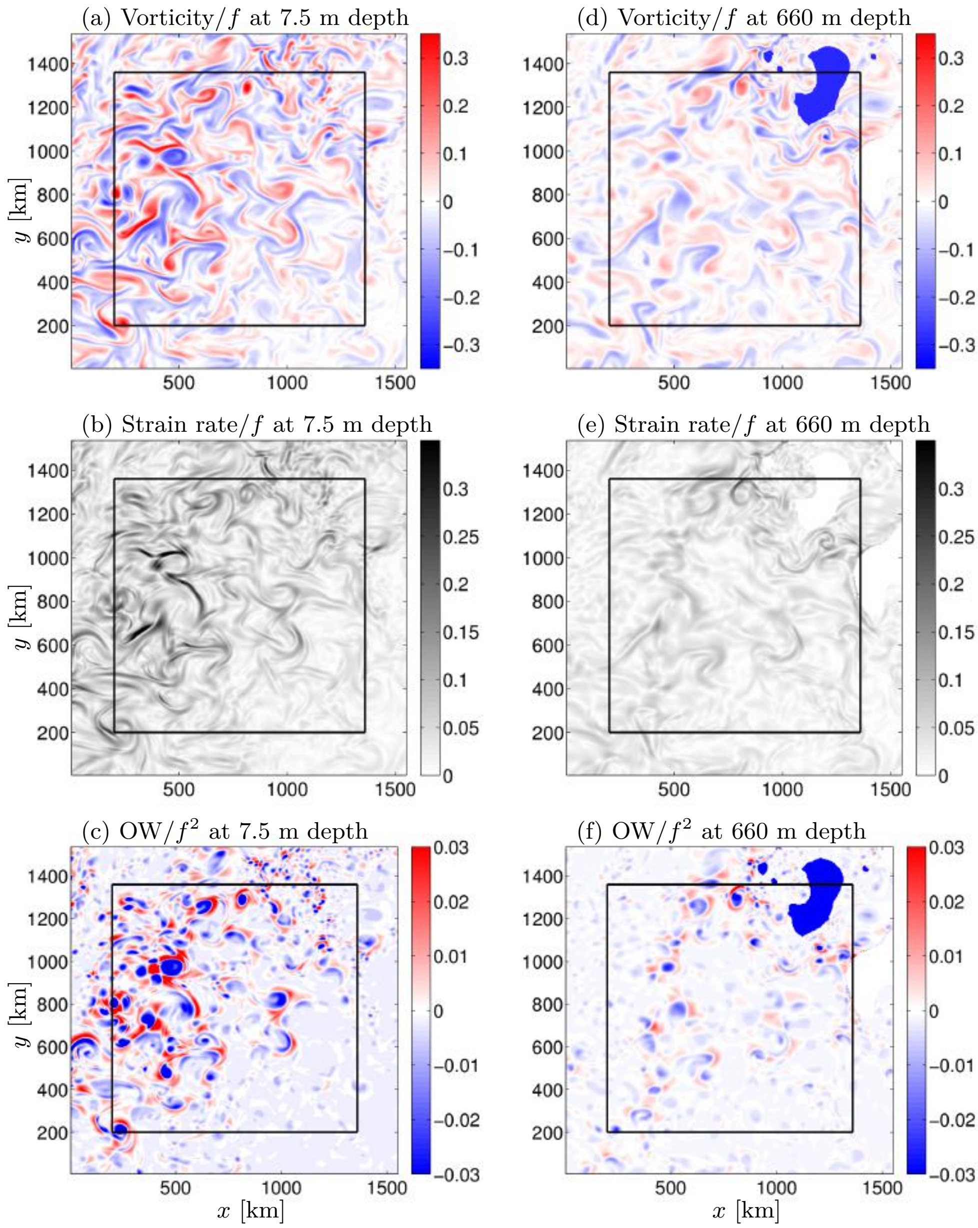

Figure 4.7: Normalised Eulerian fields evaluated at day 270 [end of September] of the year 2011 in the North Eastern Atlantic Ocean. Left column: (a) relative vorticity (b) strain rate and (c) OW parameter at 7.5 m depth . Right column: (d) relative vorticity, (e) strain rate and (f) OW parameter at ∼ 660 m depth.

agreement with previous studies (e.g., Thomas et al., 2008) which have reported that submesoscale dynamics thrive in the presence of weak stratification which is characteristic of the ML, and that these dynamics reduce by several folds in the pycnocline. One particular property of the ML that governs the dominance and visibility of small scale features, is the mixed layer depth (MLD) whose deepening in winter leads to their increased intensity, and to its weakening when the MLD becomes shallow in summer (e.g., Sasaki et al., 2014; Thompson et al., 2016). As expected, Eulerian diagnostics in the interior attain values lower than those obtained at the ocean surface due to the weakening of the flow in the ocean interior (see Figs. 4.6 d,e,f and Figs. 4.7 d,e,f).

In summer, when the ML is shallow (attaining average values ~ 25 m, see fig. 4.5), the number of vortices with radii below 50 km is noticed to have reduced, both at the ocean surface and interior (see Fig. 4.7), with mesoscale vortices of radii of $\mathcal{O}(100 \text{ km})$ covering most regions of the domain. The values attained by the Eulerian diagnostics are also noticed to be generally lower than those calculated for the winter period, which signifies the stirring importance of MLIs enhanced during winter and weakened in summer. Several studies have previously reported the emergence of a richness of scales in winter, its weakening in summer and its associated seasonality using Eulerian diagnostics (e.g., Mensa et al., 2013; Sasaki et al., 2014) and statistical techniques (e.g., Callies et al., 2015). In this thesis, we consider an alternative diagnostic, the FTLE, to understand the seasonality of the turbulence arising due to these small scale features and the factors upon which it depends.

4.2.1 FTLEs

FTLEs are calculated following the same methodology used in the idealised simulations in Section 3.2. We here consider only the backward FTLEs since they can be used as proxies for passive tracer (e.g., Beron-Vera and Olascoaga, 2009), thus allowing a calculation of passive tracer spectra from which we understand whether local or nonlocal dynamics dominate the flow. Also, it was found in Chapter 3 that forward and backward FTLEs yield comparable magnitudes of FTLEs and similar statistics (see Fig. 3.8 a,b), although the finite-time dynamical systems involved are different since they involve use of different initial conditions (Haller, 2015).

Analysis of snapshots of the backward FTLEs calculated in windows of 15 days for the four years considered, shows that 3D FTLEs are surface intensified both in winter and summer, while their vertical variation reduces in the sub-surface and deep interior of the ocean. It should therefore be noted that a different scale has been used for 3D FTLEs at the surface, to allow for a clear visualization of flow features, which would otherwise have been impossible to see. The 2D FTLEs instead show only a minimal change between the surface and sub-surface values, initially increasing and reaching a maximum near the base of the ML, and then decreasing with depth to the deepest level of the ocean considered (Figs. 4.8 and 4.9). As observed in Chapter 3 for the idealised simulation, the 3D FTLEs at the surface are more complex (Fig. 4.8a and Fig. 4.9a), showing large values of FTLEs both at the edges and interior of vortices, and along filaments. However, they yield a more distinct appearance at the base of the ML (Fig. 4.8b and Fig. 4.9b). The 2D FTLEs instead yield a distinct appearance with large FTLE values at the edges of vortices and along filaments at all depths. It should however be noted that both 3D and 2D FTLEs show ridges in similar locations.

Maps of 2D FTLEs for the surface and interior of the ocean, differ only slightly in magnitude (Fig. 4.8 d-f and Fig. 4.9 d-f) compared to those of 3D FTLEs, which are seen to be strongly intensified at the surface while changing slightly in the pycnocline (Fig. 4.8 a-c and Fig. 4.9 a-c). The distinct appearance of 2D FTLEs also reveals a dominance of frontal structures both at the surface and interior of the ocean. The

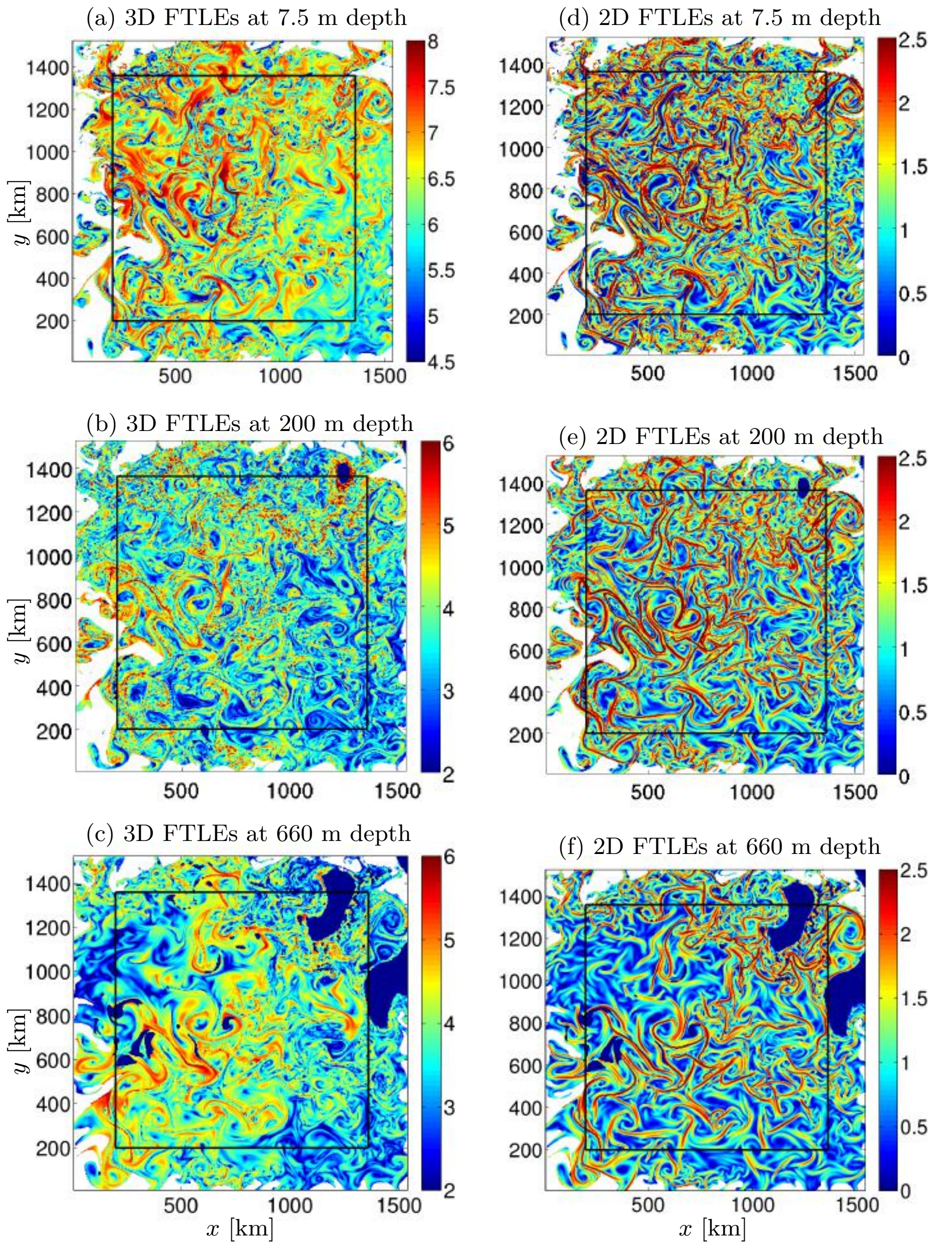

Figure 4.8: Backward in time 3D (left column) and 2D (right column) FTLEs calculated at day 90 [end of March] of year 2011 in the North Eastern Atlantic Ocean at (a, d) 7.5 m, (b, e) $\sim$ 200 m and (c, f) 660 m depths.

large difference in magnitude between surface and sub-surface values of 3D FTLEs is further noticed in the vertical profiles calculated from the seasonal averages over the four years considered. Below the ML, which is on average $\sim$ 30 m in summer and $\sim$ 200 m in winter, 3D FTLEs are found to reduce by $\sim$ 50% of their surface values. In the topmost levels of the ocean, the difference in magnitude between winter and summer 3D FTLEs is minimal with both quantities showing minimal changes with depth. The winter 3D FTLEs show a vertical structure, which is smoothly decreasing at a rate faster than linear within the ML. In the ocean interior, 3D FTLEs are observed to vary only slightly with depth, with the winter season exhibiting values

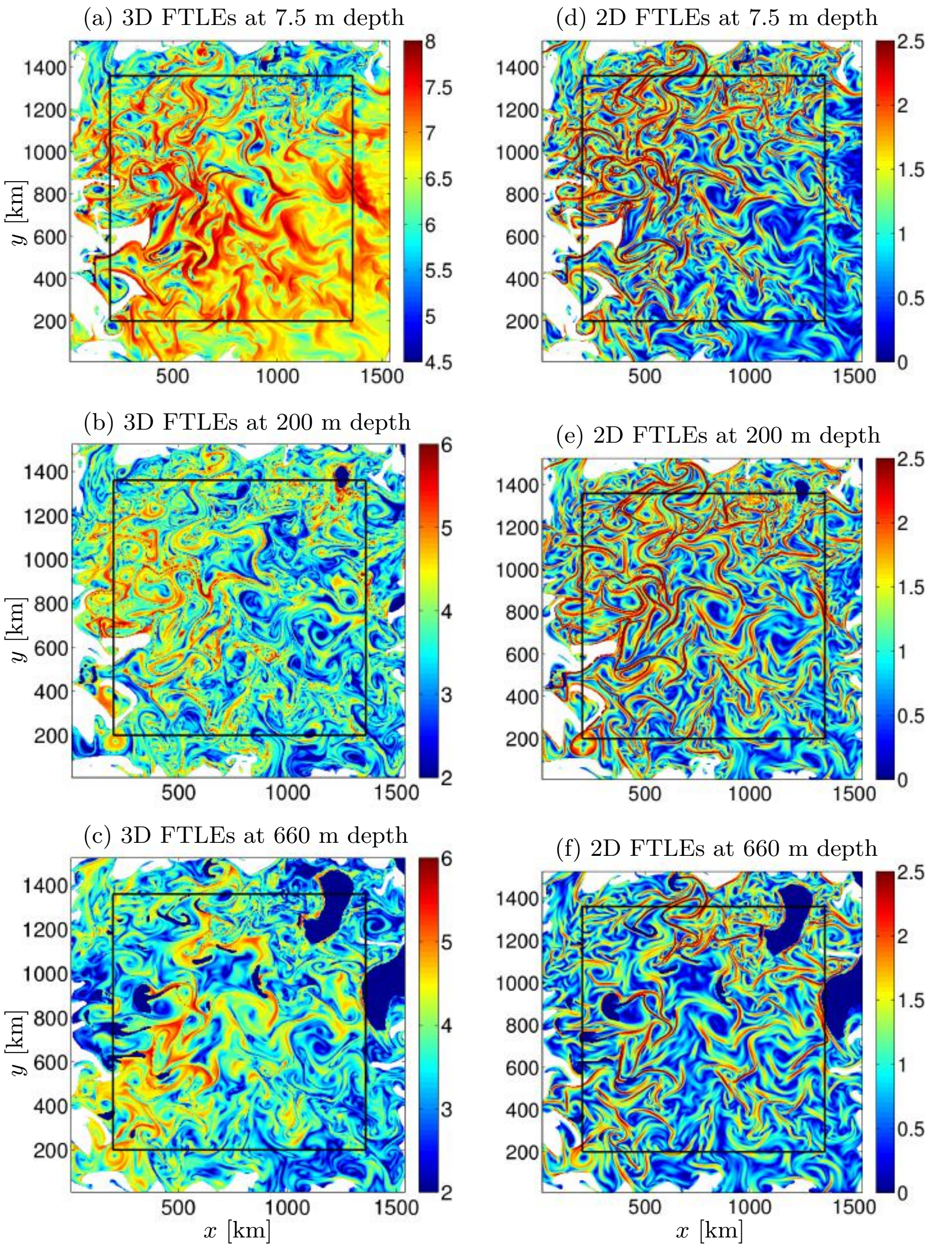

Figure 4.9: Backward in time 3D (left column) and 2D (right column) FTLEs calculated at day 290 [end of October] of the year 2011 in the North Eastern Atlantic Ocean at (a, d) 7.5 m, (b, e) $\sim$ 200 m and (c, f) 660 m depths.

larger than those in the summer as expected due to the strong winter stirring activity (Fig. 4.10).

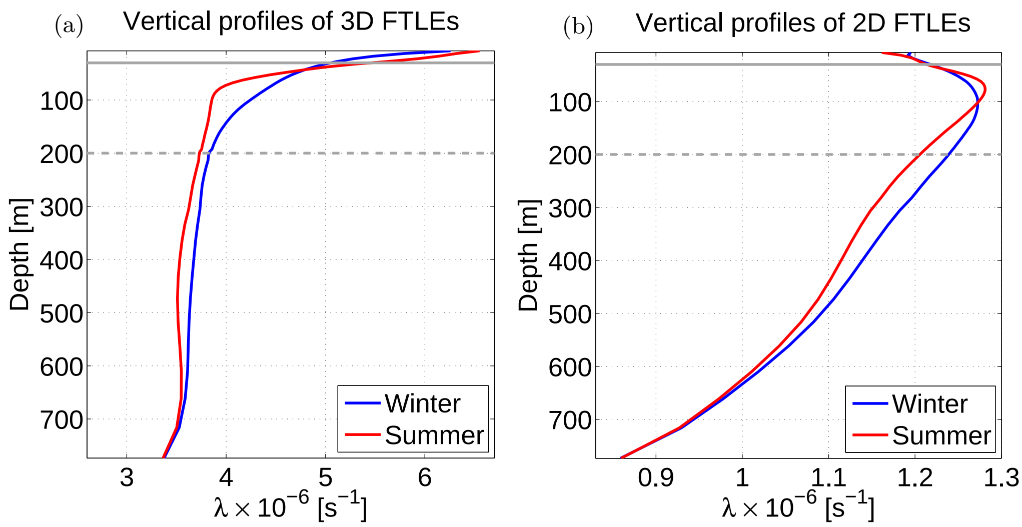

Figure 4.10: Average vertical profiles of area averages for (a) 3D FTLEs and (b) 2D FTLEs calculated for the winter [between 21st December to 21st March] and summer [between 21st June to 21st September] for the region in North Eastern Atlantic Ocean. The full and dashed gray lines correspond to the average summer and winter mixed layer depths respectively. Note that different scales are used for 3D and 2D FTLEs due to the large difference in magnitude between them.

Vertical profiles instead show that 2D FTLEs increase with depth reaching local maxima at $\sim$ 70 m and $\sim$ 110 m in the summer and winter seasons respectively, and then decrease with depth to the lowest levels of the ocean considered. The winter and summer 2D FTLEs are also observed to yield only slight differences in magnitude in the topmost levels of the ocean, while they separate in the interior, yielding larger values for winter than summer. The deep MLs in winter lead to the emergence of more energetic small scale features, thus yielding large FTLE values in the ocean interior. In summer instead, the ML is relatively shallow, shrinking the APE reservoir from which ML baroclinic instabilities (Molemaker and McWilliams, 2005) draw and thus yielding low FTLE values in the pycnocline (Fig. 4.5).

4.2.2 Seasonality of FTLEs

To study the seasonal cycle of FTLEs and the factors that modulate them, in the two case study regions of the Atlantic ocean, we consider time series calculated at a frequency of every 15 days during the four years: 2006, 2007, 2010 and 2011. Due to the limited span of our time series of FTLEs, the analysis offered in this thesis is generally qualitative. Figure 4.11 presents the time series of 3D and 2D FTLEs superimposed on top of each other, to allow for a comparison between them. It should be noted that the scale used for 3D FTLEs (on the left) is different from that of 2D FTLEs (on the right) which are found to be ~ 6 and ~ 3 times smaller at the surface and pycnocline, respectively. The variability of 3D and 2D FTLEs is noticed

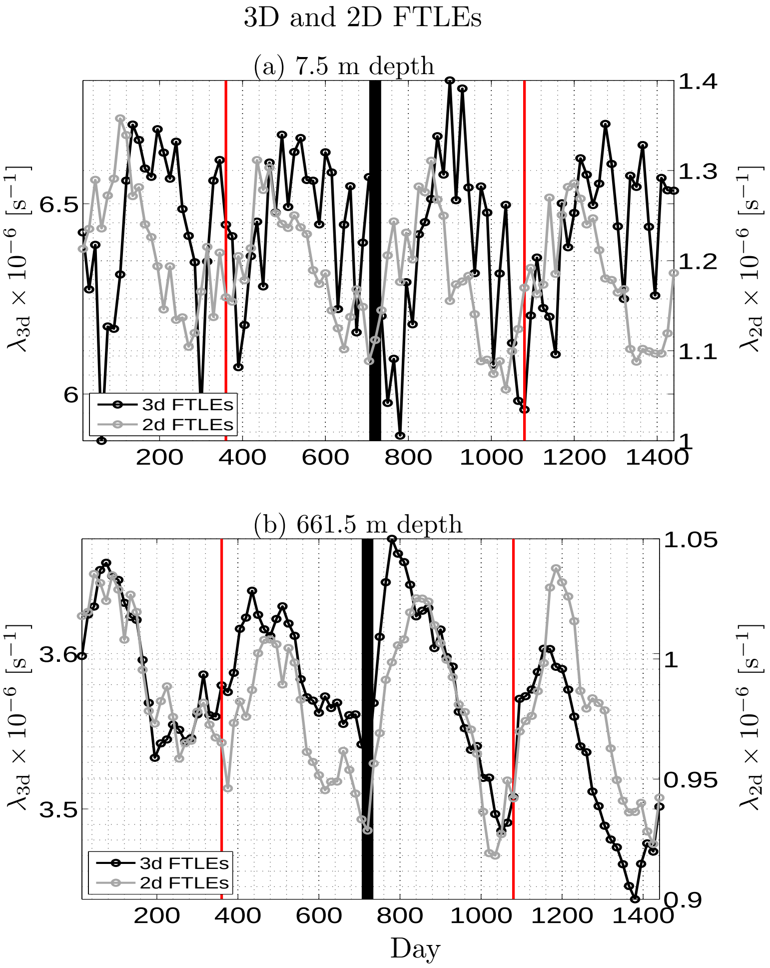

Figure 4.11: Timeseries of 3D FTLEs (black lines, left vertical scale) and 2D FTLEs (gray lines, right vertical scale) at (a) 7.5 m depth and (b) 661.5 m depth over the years 2006, 2007, 2010 and 2011 for the region in the North East Atlantic Ocean. Red lines separate the different years and the thick vertical black line emphasizes the jump between the year 2007 and 2010.

to be stronger at the surface than in the ocean interior, as it would be expected due to the variability of the surface wind forcing (see Fig. 4.11a,b), but further studies are required to study this correlation.

At the ocean surface, 3D FTLEs show a seasonal cycle, reaching a maximum in spring and a minimum, late in summer. Similarly, 2D FTLEs show a clear seasonal behaviour, attaining maximum values in late winter and reaching a minimum in late autumn (Fig. 4.11a). Noticeable also is that 3D FTLEs show more variability than that yielded by 2D FTLEs, which could mean that the two diagnostics depend on different factors at the ocean surface. Also in the interior, both 3D and 2D FTLEs show a clear seasonal cycle, representing more stirring in winter and less in summer. Further, apart from a small discrepancy that 3D FTLEs reach a maximum earlier than 2D FTLEs, the variability of the two diagnostics is comparable (Fig. 4.11b). In what follows, we attempt to study the factors that determine the seasonal cycle of the FTLEs, with particular emphasis on factors and dynamics set by properties of the mixed layer.

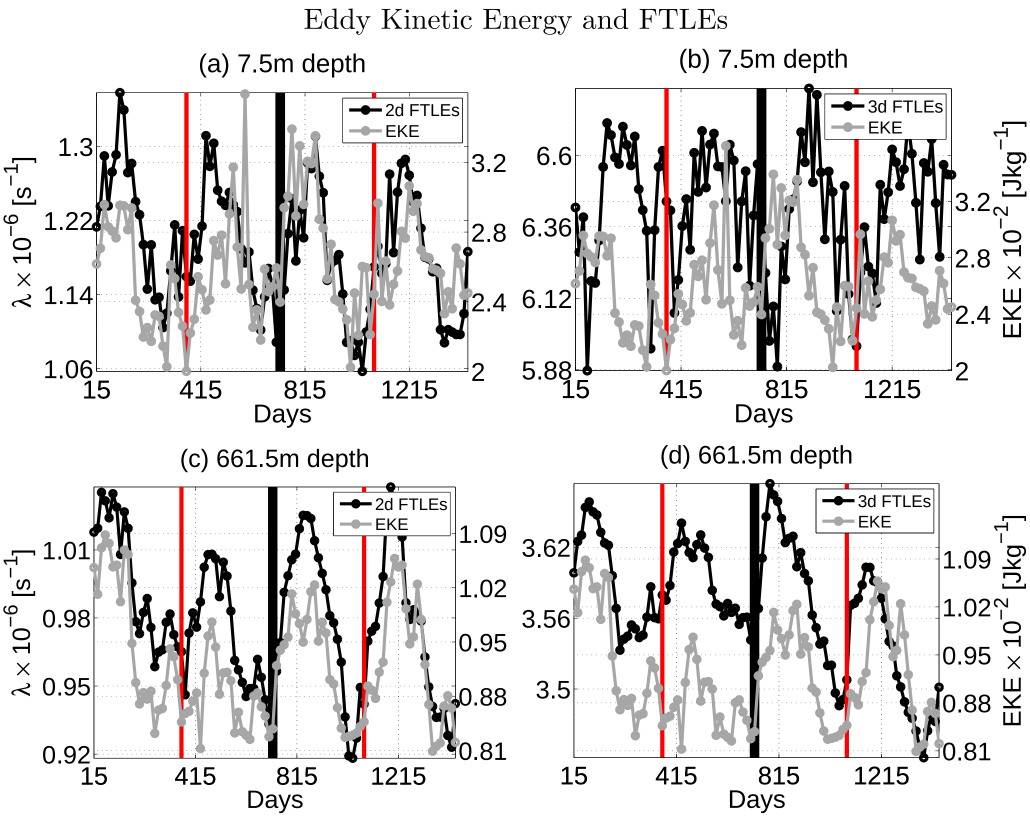

Figure 4.12: Timeseries of 2D FTLEs (black lines in left panels), 3D FTLEs (black lines in right panels) and Eddy Kinetic Energy (gray lines) at (a, b) 7.5 m depth and (c, d) 661.5 m depth over the years 2006, 2007, 2010 and 2011 for the region in the North Eastern Atlantic Ocean. Red lines separate the different years and the thick vertical black line emphasizes the jump between the year 2007 and 2010.

First, we seek to understand the relationship between FTLEs and the eddy kinetic energy (EKE), defined in units of m^2s^{-2} as

$$\mathrm{EKE} = \frac{1}{2}(u'^2 + v'^2) \ , \tag{4.1}$$

where the primed variables represent deviations from a respective 10 year average of the parent simulation described in Section 4.1. The EKE shows a seasonal cycle, attaining maximum values late in winter and minimum values late in summer. At the ocean surface, the EKE shows a phase difference from the 2D FTLEs, reaching its maximum values before the 2D FTLEs. The seasonality of 2D FTLEs can thus

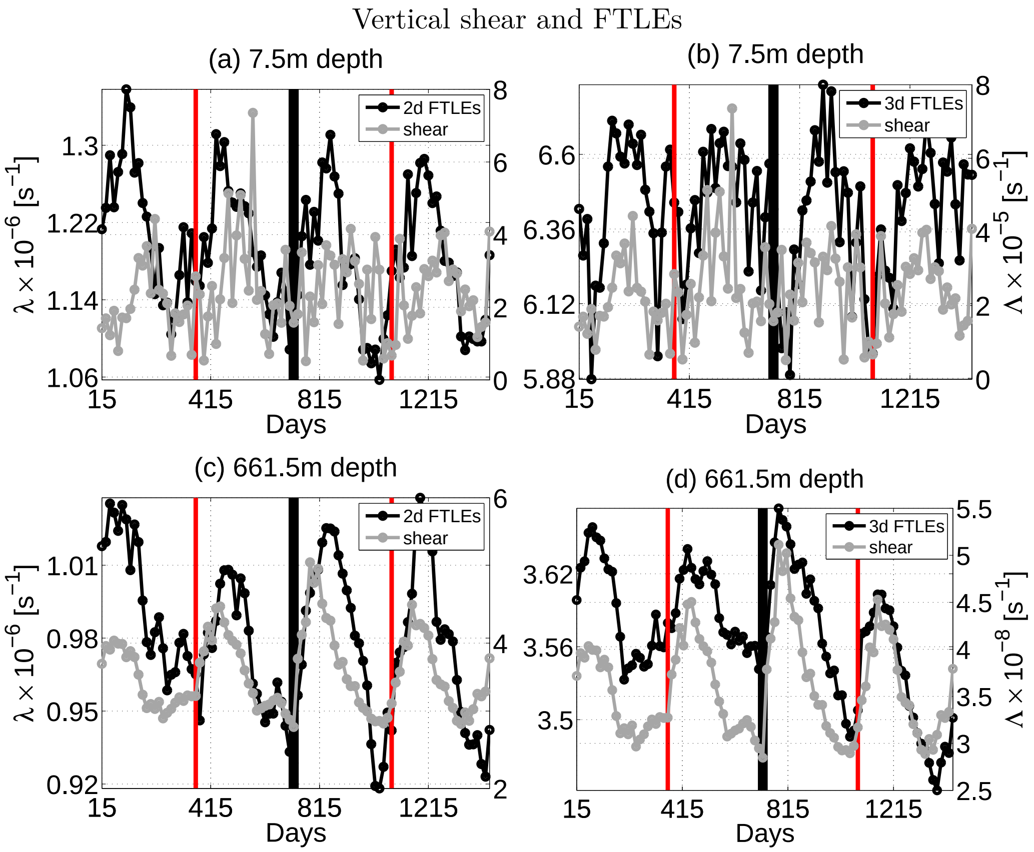

Figure 4.13: Timeseries of 2D FTLEs (black lines in left panels), 3D FTLEs (black lines in right panels) and root mean square value of the vertical shear of horizontal velocities (gray lines) at (a, b) 7.5 m depth and (c, d) 661.5 m depth over the years 2006, 2007, 2010 and 2011 for the region in the North East Atlantic Ocean. Red lines separate the different years and the thick vertical black line emphasizes the jump between the year 2007 and 2010.

be said to be modulated by the EKE, with the contribution of the other sources of forcing manifesting in the lag between the peaking times of the two diagnostics. In the pycnocline, the EKE and 3D FTLEs reach their respective maxima at the same instant of time, with both diagnostics reaching their maxima in the spring, and reducing to their respective minima in late summer (Fig. 4.12 d). In three of the four years considered, EKE reaches a maximum before the 3D FTLEs, which reach their maximum in late spring. This shows that EKE alone is not sufficient to explain increased values of 3D FTLEs at the ocean surface in winter, and their decrease late in the summer (Fig. 4.12 b).

In the idealised study in Chapter 3, it was found that the magnitude and structure of 3D FTLEs, are determined by the vertical shear of horizontal velocities while 2D

FTLEs are determined by the horizontal shear. We therefore proceed to confirm or not that finding in a more realistic setting by comparing the time series of FTLEs and vertical shear of horizontal velocities. The vertical shear of horizontal velocities yields a clear seasonal cycle, both at the surface and in the ocean interior (see gray curves in Fig. 4.13). At the surface, the vertical shear increases during winter reaching a maximum in late spring, and then decreases reaching a minimum in autumn. In the ocean interior instead, the vertical shear attains maximum values in winter and reaches its lowest values in late summer. The existence of a correlation between the time series of 3D FTLEs and vertical shear of horizontal velocities both at the ocean surface and interior (see Figs. 4.13b,d), is in agreement with the findings in the idealised simulations in Chapter 3, that 3D FTLEs are modulated by the vertical shear of horizontal velocities. More interestingly, it will be shown a little later that the modulation of 3D FTLEs by the vertical shear of horizontal velocities, also holds in the Central Atlantic ocean, where the flow is surface intensified and relatively much weaker than in the North East Atlantic ocean.

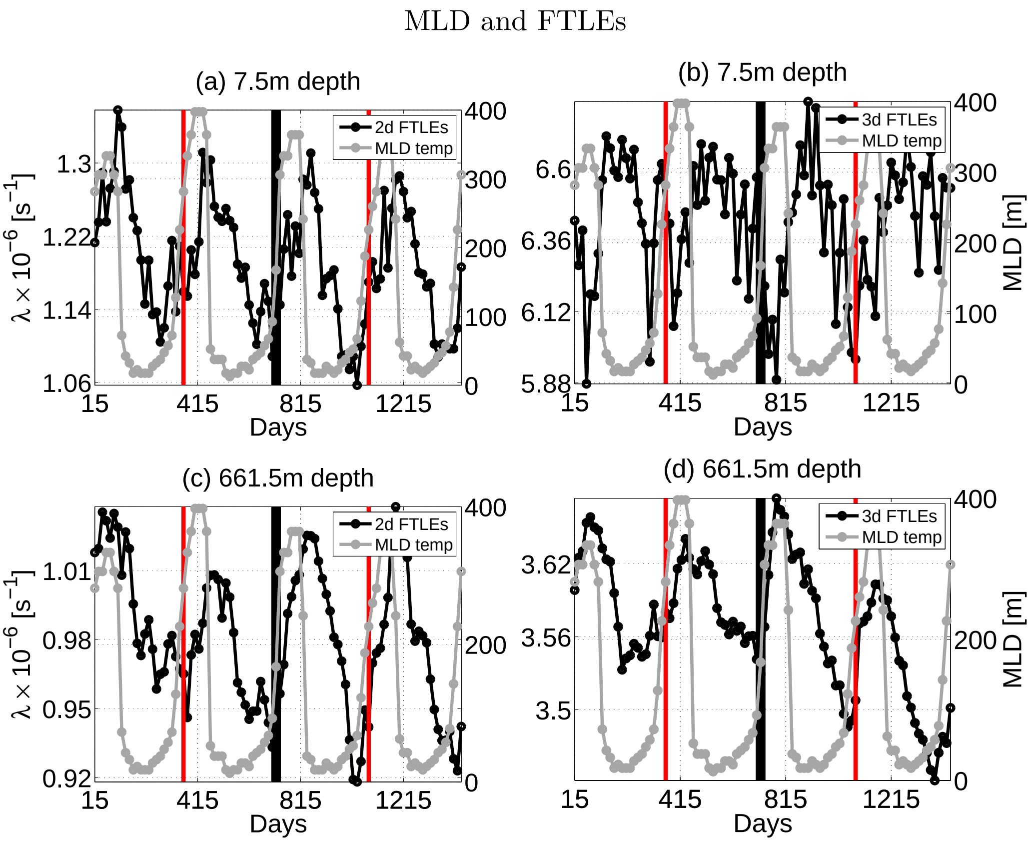

Figure 4.14: Timeseries of 2D FTLEs (blacklines in left panels), 3D FTLEs (blacklines in right panels) and mixed layer depth (gray lines) at (a, b) 7.5 m depth and (c, d) 661.5 m depth over the years 2006, 2007, 2010 and 2011 for the region in the North East Atlantic Ocean. Red lines separate the different years and the thick vertical black line emphasizes the jump between the year 2007 and 2010.

In various basins of the World Ocean, studies about the seasonality of the oceanic

ML turbulence from numerical modelling (e.g., Mensa et al., 2013; Sasaki et al., 2014; Gula et al., 2016) and observations (e.g., Callies et al., 2015; Thompson et al., 2016) have reported a strong relationship between the MLD and the emergence of energetic small scale features, with more (in number) and energetic vortices and filaments emerging in winter when the ML is deep and a reduction in intensity or disappearance of such features in summer when the ML is shallow. In this Chapter, we consider two contrasting regions (in terms of MLDs displayed, see fig. 4.5), not covered by previous studies on seasonality of the oceanic ML turbulence and move to establish the relationship between FTLEs and the seasonal cycle of the MLD. Consideration of a less active region in the Central Atlantic ocean serves to test the robustness of the findings of previous studies, which have concentrated on regions of the world ocean with strong currents like the Kuroshio (e.g., Sasaki et al., 2014) and Gulf Stream (e.g., Mensa et al., 2013; Gula et al., 2014). The exception is the study by Thompson et al. (2016), who studied the seasonality of the oceanic ML turbulence in the open ocean using a year long glider measurements of salinity, temperature and pressure fields, and found that a strong seasonal behaviour exists in key ocean properties such as stratification.

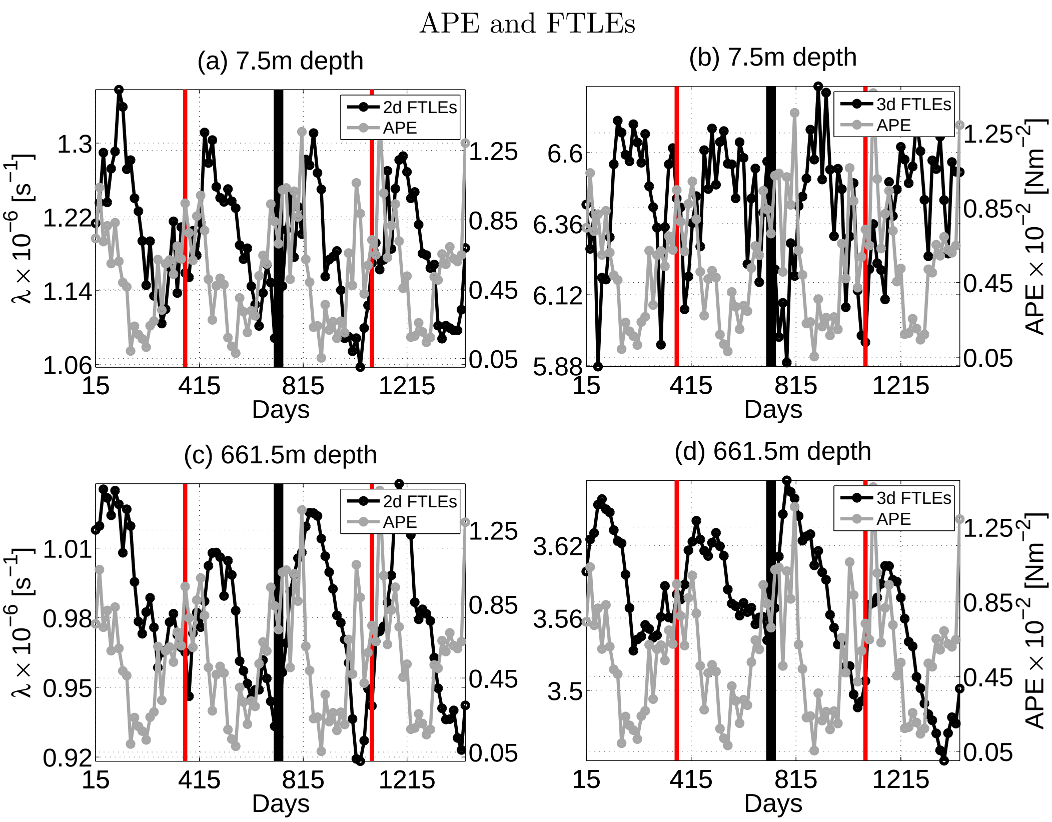

Figure 4.15: Timeseries of 2D FTLEs (blacklines lefthand panels), 3D FTLEs (blacklines righthand panels) and the available potential energy (gray lines) for the region in the North East Atlantic ocean at (a,b) 7.5 m depth, (c,d) 197.5 m depth and (e,f) 661.5 m depth for the years 2006, 2007, 2010 and 2011. Red lines separate the different years and the thick vertical black line emphasizes the jump between the year 2007 and 2010.

The MLD shows a seasonal cycle, reaching maximum values ($\sim$ 400 m) in late winter, and decreasing quickly in spring reaching minimum values ($\sim$ 25 m) in summer (Fig. 4.14). Previous studies (e.g., Boccaletti et al., 2007; Fox-Kemper et al., 2008) have reported that deep MLs act as large reservoirs of available potential energy (APE) from which baroclinic instabilities draw. The APE is defined as (e.g., Badin et al., 2009)

$$\mathrm{APE} = \frac{\rho_0}{6}\frac{f^2}{H}\int_V \frac{1}{N}\frac{\partial U}{\partial z} dxdydz \ , \tag{4.2}$$

where V is the volume of the domain considered, ρ_0 is the reference density and $\partial U/\partial z$ is the root mean square value of the vertical shear of horizontal velocities. As such, the MLD should be viewed as a cause and the APE as the consequence which is in turn converted to EKE as the instabilities develop. On the contrary, the APE is expected to be lower in summer when the MLs are predominantly shallow, yielding low EKE and thus less energetic instabilities and stirring. It should however be noted that other sources of energy like surface wind could contribute to the EKE budget in addition to the APE contribution from baroclinic instabilities.

With the exception of the FTLEs showing longer tails and slower descent from their maxima in winter to their minima in late summer, the seasonal cycles of FTLEs and MLD display maximum values at the same time and thus, it can be concluded that the seasonal cycle of 2D FTLEs in the ocean interior is determined by the MLD. At the surface, the MLD reaches its maxima before the 2D FTLEs reach their respective maxima (Fig. 4.14a) and it can thus be suggested that baroclinic MLIs drawing their energy from the APE are responsible for modulating the 2D FTLEs, with the lag between the two quantities attributed to the time required for the instabilities to reach maximum amplitude, which is of the order of days (e.g., Boccaletti et al., 2007). The variability of 3D FTLEs at the ocean surface cannot be directly linked to MLD (hence MLIs) since 3D FTLEs reach their maxima much later and show a lot of variability which is not observed in the time series of the MLD (see Fig. 4.14b). The seasonal cycle of 3D FTLEs at the ocean surface is however noticed to closely follow that of the vertical shear of horizontal velocities (see Fig. 4.13b).

As expected, time series of the APE display a seasonal cycle close to that shown by the MLD, attaining maximum values in winter and reaching its minimum in summer when the MLD is also at its lowest (Fig. 4.15). At the surface, the seasonal cycle of 2D FTLEs is noticed to be well marked by that of the APE, except for a delay of the order of 15 - 30 days which may be attributed to the growth time scale of instabilities, whose resulting stirring influence is assumed here to be wholly captured by the FTLEs. No clear relationship can be drawn between 3D FTLEs at the surface and APE. In the ocean interior, the time series of FTLEs and APE, closely follow each other and the observed phase difference is larger than that displayed between FTLEs and MLD (see Fig. 4.14).

4.2.3 Spectra

In what follows, we calculate wave number spectra in each year, averaged for winter [21st December to 21st March] and summer [21st June - 21st September] and further consider the average over the fours years. The ML deformation radii R$_d$ calculated using (3.7) in the two case study areas show differences for both winter and summer seasons, attaining large values for the region in the North East Atlantic ocean where the ML is deep and low values in the Central Atlantic where the ML is shallower. Similarly, values of the first baroclinic Rossby deformation radius in the pycnocline vary widely due to the large differences in MLD in the two case study regions and also during the winter and summer seasons over which the stratification varies (see Table 4.5). The values of the ML and pycnocline deformation radii are superimposed on the spectra (in gray lines) for comparison. Also, wave number spectra are calculated along the zonal direction for the region enclosed by black lines in Figs. 4.6, 4.7, 4.8 and 4.9.

In winter, the kinetic energy (KE) spectrum $E(k) \sim k^{-\alpha}$ displays no inertial range for wave numbers above $k_d \sim 1/R_d$ due to the small ML Rossby radius of deformation (R$_d$) ($\sim$ 12 km, shown by gray line on the right). At scales above the first baroclinic deformation radius but below $\sim$ 27 km, the $E(k)$ spectrum displays slopes of $\alpha \geq 3$ corresponding to nonlocal dynamics, thus implying that the flow on such scales is controlled by flow features whose scale is larger than 27 km. At scales above 27 km, the $E(k)$ spectrum shoals acquiring a slope close to -2. The relatively gentle -2 slopes of the KE spectrum are indicative of a spectrally local regime, in which dynamics at these scales are controlled by velocity flow features of a comparable scale (Fig. 4.16a). Passive tracer spectra $T(k)$ in the ML deduced from the four year winter averaged, backward FTLEs are presented in Figs. 4.16b and 4.16c for 3D and 2D FTLEs, respectively. Both 3D and 2D FTLEs show spectra slopes close to -2 at scales below 90 km, which correspond to frontal features (Boyd, 1992). For scales between the first baroclinic deformation radius and $\sim$ 100 km, passive tracer spectra converge more to slopes of -2, and eventually attain slopes of -1, for scales above 100 km. The passive tracer spectra with -2 slopes are consistent with the $E(k)$ spectra which predicts local dynamics at scales near the deformation radius. The local stirring at scales between 27 km and 100 km can be attributed to the mesoscale vortices which are seen to dominate the flow in winter (see Fig. 4.6).

In the pycnocline, $E(k)$ spectra show -3 or steeper slopes at all scales above the first baroclinic deformation radius, which correspond to nonlocal dynamics (Fig. 4.16d). The corresponding 3D and 2D FTLE spectra show slopes s, $-2 < s < -1$ at scales $\leq$ 100 km representative of frontal features. At scales above 100 km, FTLE spectra show a gradual flattening, attaining slopes of -1 which are reflective of local dynamics. The -2 slopes shown by the FTLE spectra for scales below 100 km are indicative of frontal dynamics and have also been found in the idealised simulations studied in Chapter 3. This result is consistent with findings of previous studies in various basins of the world Ocean, which report passive tracer spectra of similar slopes (e.g., Cole and Rudnick, 2012; Kunze et al., 2015).

The KE spectra at the ocean surface and interior show discrepancies in slopes, es-

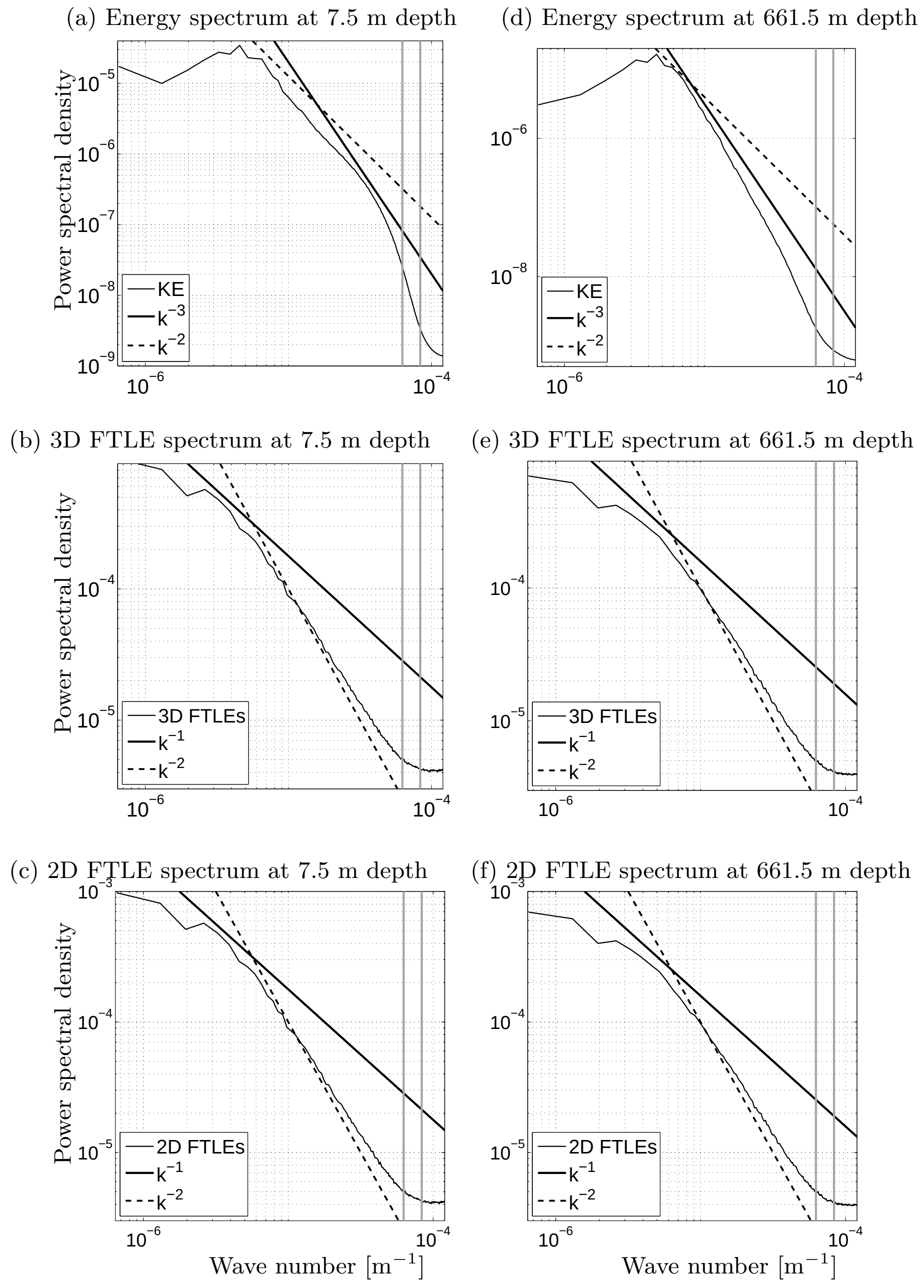

Figure 4.16: Winter Spectra of kinetic energy calculated at (a) 7.5 m depth and (d) 661.5 m depth. 3D FTLE spectra averaged for the winter season at (b) 7.5m depth and (e) 661.5 m depth. 2D FTLE spectra calculated at (c) 7.5 m depth and (f) 661.5 m depth, all for the region in the North East Atlantic ocean. On each panel, gray lines show the location of the ML (left) and first baroclinic (right) deformation radii.

pecially at scales near $\sim$ 30 km, while the FTLE spectra maintain the same slopes at the surface and in the interior (see Fig. 4.16b,c,e,f). Passive tracer spectra with -2 slopes at the ocean surface and interior have also been found in high resolution numerical simulations of the California Current System (Capet et al., 2008), and are seemingly robust since they are independent of the spatial resolution and are also obtained for both idealised and realistic ocean simulations. In addition, the prediction of frontal dynamics in the ocean interior is in agreement with earlier findings (e.g., Badin et al., 2011; Ragone and Badin, 2016) which have reported that MLIs penetrate into the pycnocline where they may affect the lateral stirring of tracers. The presence of energetic fine filaments in FTLE fields inside the ocean interior (Figs. 4.8f and 4.9f), is evidence of the impact of instabilities originating from the ML, in

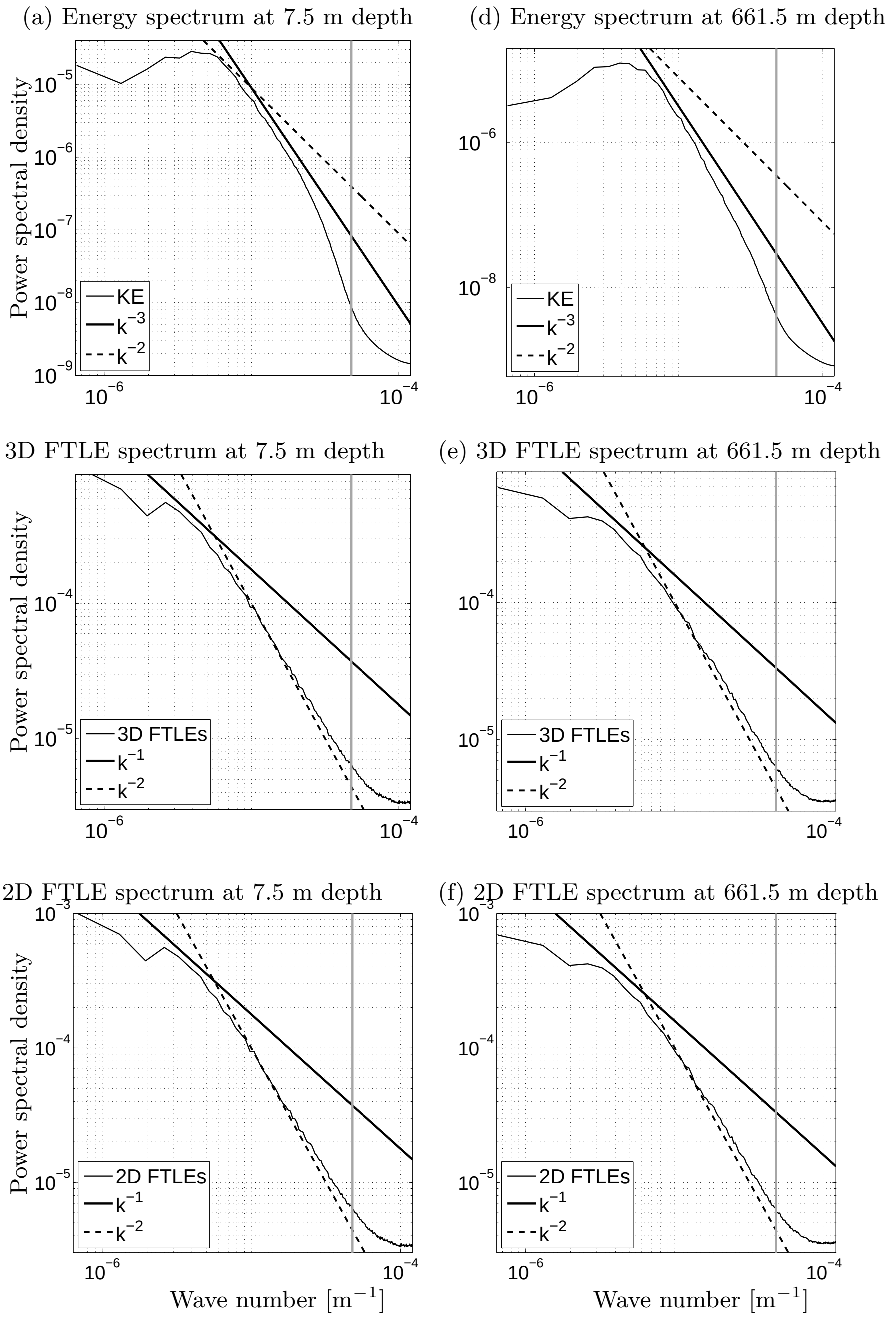

Figure 4.17: Summer Spectra of kinetic energy calculated at (a) 7.5 m depth and (d) 661.5 m depth. 3D FTLE spectra averaged for the summer season at (b) 7.5m depth and (e) 661.5 m depth. 2D FTLE spectra calculated at (c) 7.5 m depth and (f) 661.5 m depth, all for the region in North Eastern Atlantic. On each panel, the gray line shows the location of the first baroclinic deformation radius.

the pycnocline.

In summer, KE spectra show slopes of -3 or steeper at all depths, which is reflective of nonlocal dynamics, while backward in time FTLE (passive tracer) spectra show -2 slopes corresponding to frontal dynamics, for scales below 100 km. At scales above 100 km, the tracer spectra gradually become gentle converging to slopes of -1 above the deformation radius (Fig. 4.17). The disappearance in summer of gentle slopes in the $E(k)$ spectrum, seen in the winter, at scales near $\sim$ 30 km, is due to the low intensity of small scale vortices and filaments, which dominate the flow during winter when the ML is deep. Noteworthy here is that the -2 slopes of passive tracer that persist at all depths of the ocean are observed to exist even in summer. The transition of tracer spectra from -2 slopes at scales below $\sim$ 100 km, to -1 at scales above 100 km is due to the fact that in this region, the flow is dominated by mesoscale vortices of comparable size that act to tangle FTLEs energetically and thus causing a larger variance of FTLEs at such scales.

4.3 Results: Central Atlantic Ocean

For the relatively less energetic region in the Central Atlantic ocean, features over a broad range of scales are also noticed to dominate the surface ocean, ranging from submesoscale to mesoscale vortices and filaments. Features of $\mathcal{O}(10$ km$)$ are attributed to the deep ML (for winter) in which baroclinic MLIs energised by the available potential energy in the quasi-vertical isopycnals of the ML thrive (Fig. 4.18). Also, the stirring resulting from the flow is observed to be surface intensified and significantly weakening in the ocean interior (Fig. 4.18). In addition to the weakening of the flow in the ocean interior, a disappearance of features at scales below 30 km in the interior is noticed and frontal structures are observed to dominate the flow (Fig. 4.18 d,e,f).

In summer, the energetic filaments and submesoscale vortices disappear both at the surface and ocean interior retaining only the frontal structures and mesoscale vortices (Fig. 4.19). The disappearance of the submesoscale structures may be explained by the shallow MLs in summer, which are as low as 20 m (see Fig. 4.5), thus providing minimal APE for the developing instabilities.

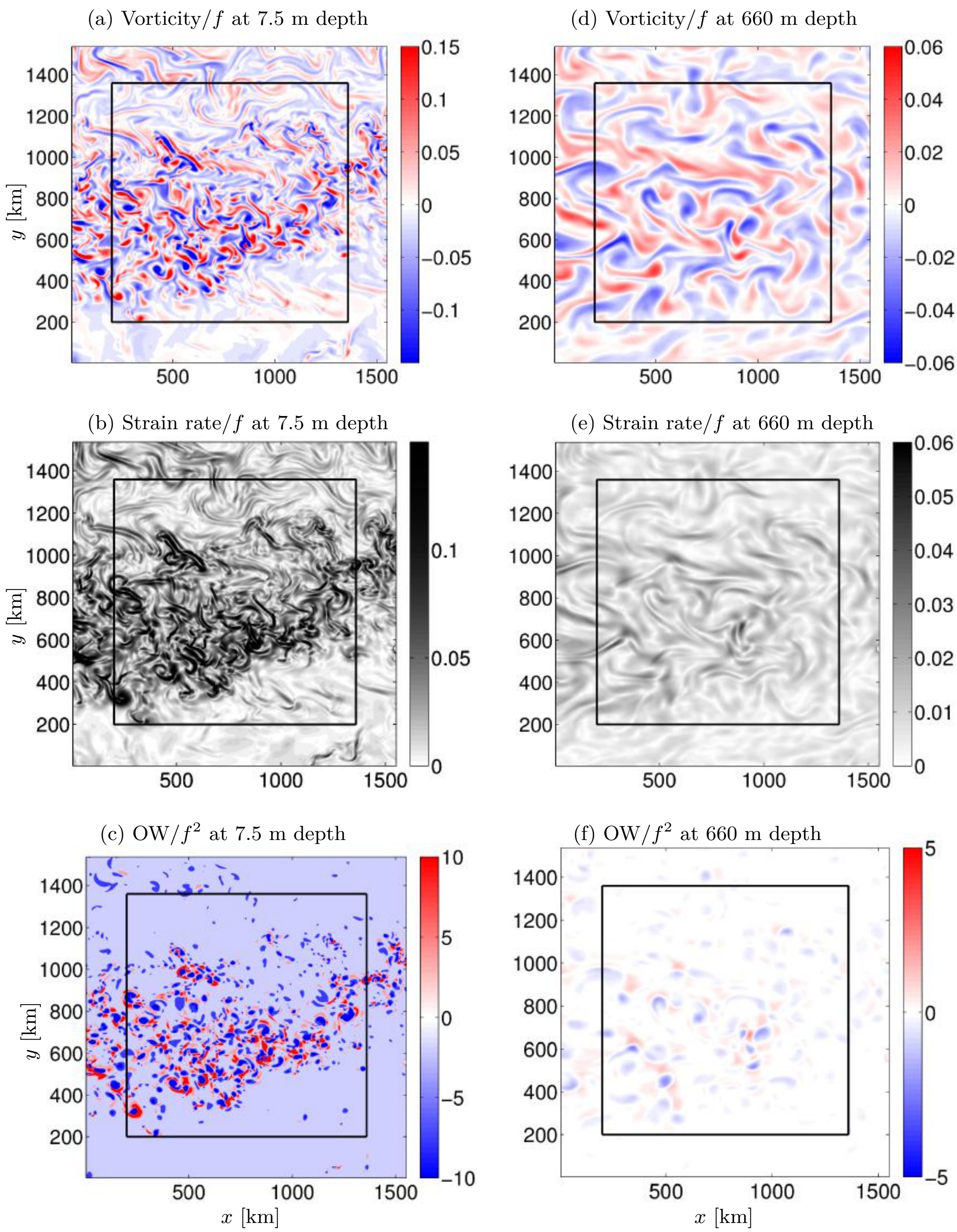

Figure 4.18: Normalised Eulerian fields evaluated at day 90 [end of March] of the year 2011 in the Central Atlantic Ocean. left column: (a) relative vorticity (b) strain rate and (c) OW parameter at 7.5 m depth . right column: (d) relative vorticity, (e) strain rate and (f) OW parameter ($\times 10^{-3}$) at $\sim$ 660 m depth.

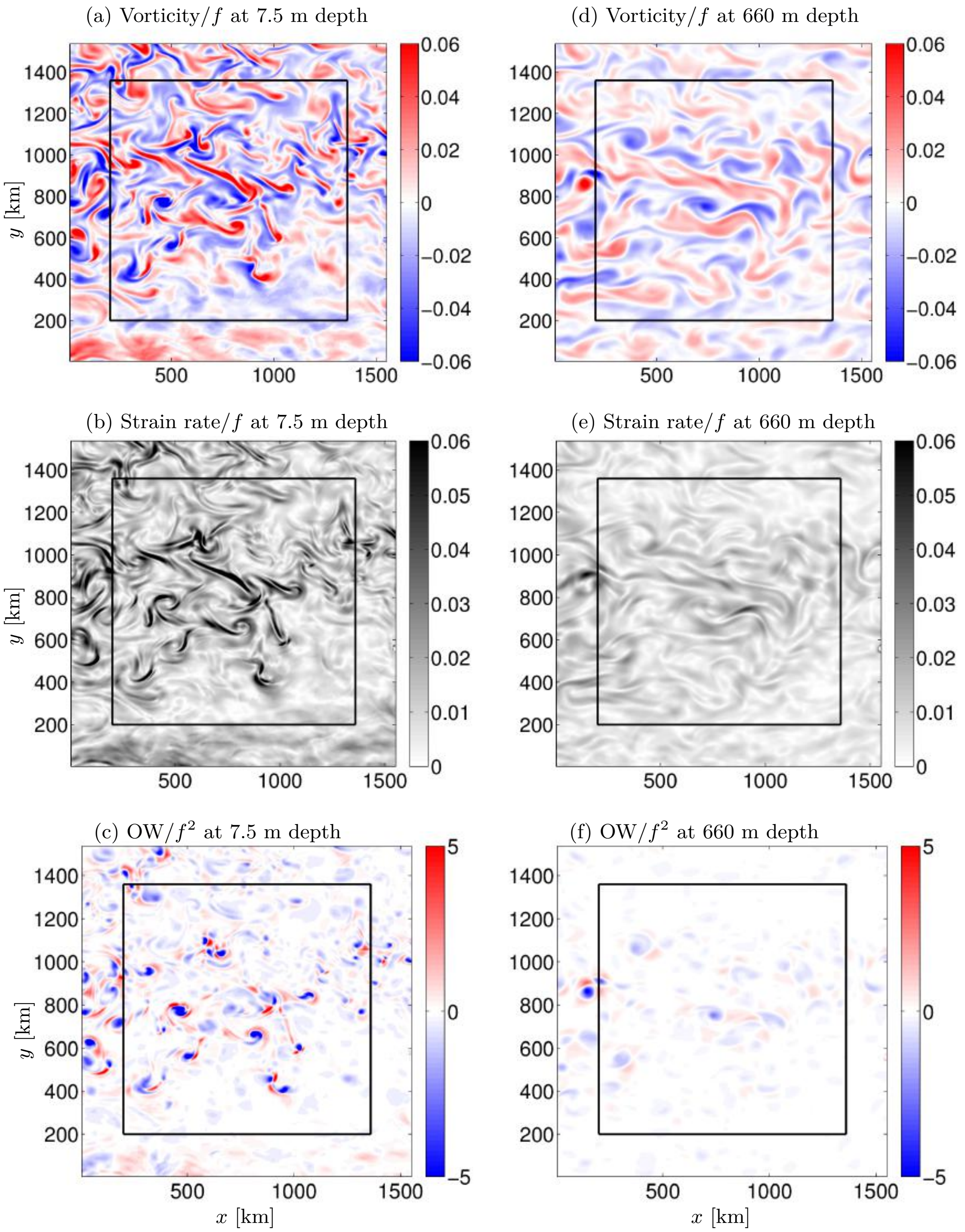

Figure 4.19: Normalised Eulerian fields evaluated at day 290 [end of September] of the year 2011 in the Central Atlantic Ocean. Left column: (a) relative vorticity (b) strain rate and (c) OW parameter at 7.5 m depth . Right column: (d) relative vorticity, (e) strain rate and (f) OW parameter ($\times 10^{-3}$) at $\sim$ 660 m depth.

4.3.1 FTLEs

As in the idealised simulations discussed in Chapter 3, 3D FTLEs display large values of FTLEs on vortex boundaries, vortex cores and along filaments (Fig. 4.20 a,b). Further, while 3D FTLEs were found to be approximately twice as large as 2D FTLEs in the idealised simulations, we here notice that 3D FTLEs are more than twice larger than 2D FTLEs both at the surface and ocean interior for both winter and summer seasons (see also Fig. 4.21). The energetic stirring in winter at the ocean surface and its weakening in the interior is also displayed by the FTLEs, which show large values at the surface and low values in the interior (Fig. 4.20 and 4.21).

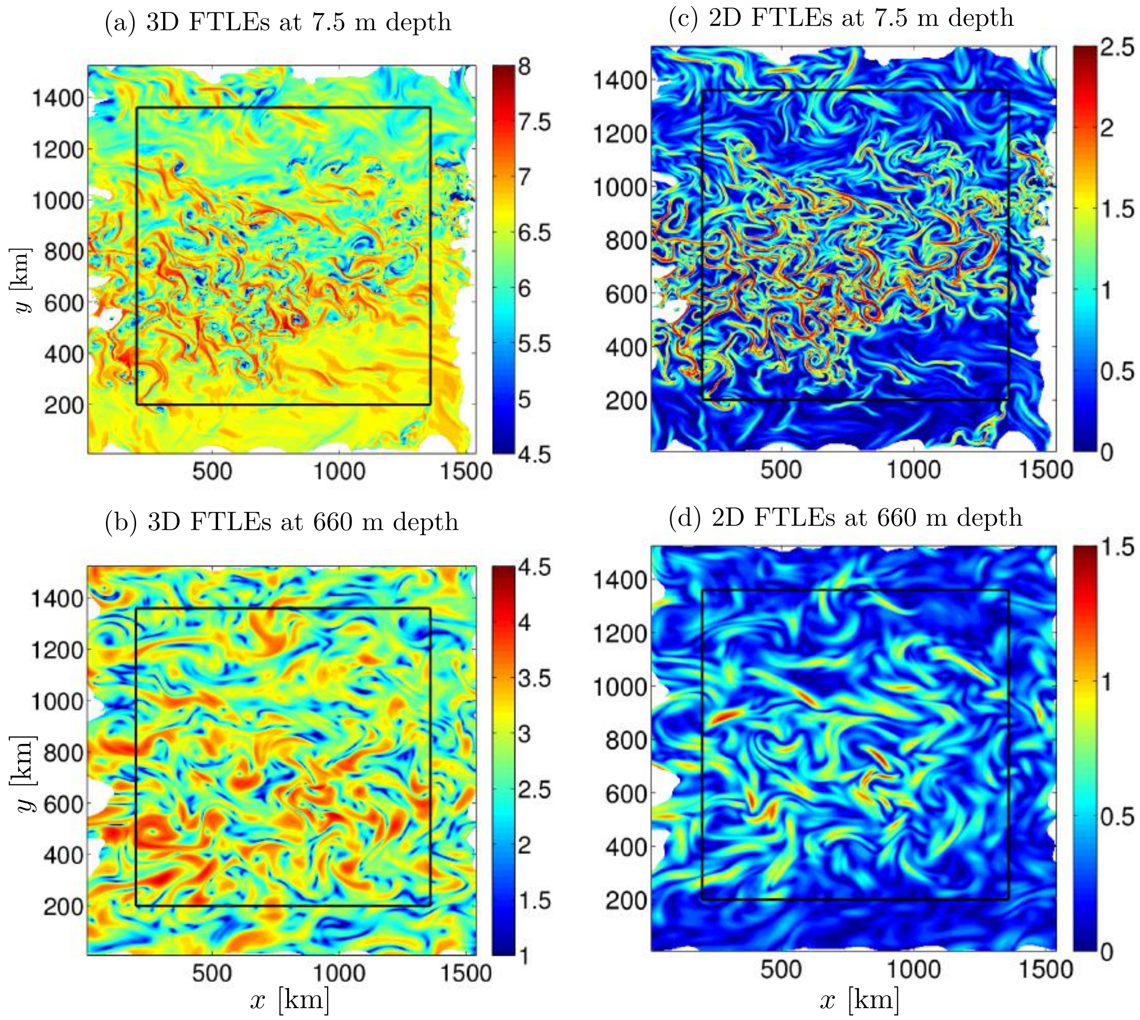

Figure 4.20: Backward in time 3D (left column) and 2D (right column) FTLEs calculated at day 90 [end of March] of year 2011 in the Central Atlantic Ocean at (a, c) 7.5 m and (b, d) 660 m depths. Different colorbars are used to enable a clear visualization of features at the surface and ocean interior.

The 2D FTLEs reveal a predominance of frontal structures in summer while vortices disappear (Fig. 4.21). The disappearance of smaller vortices and the reduced intensity of submesoscale filaments, may be attributed to the extremely shallow ML in summer attaining values as low as 20 m (see Fig. 4.5). As also observed in the idealised simulations and the region in the North East Atlantic ocean, non zero FTLE values are observed in the ocean interior, confirming the likely role of ML dynamics, particularly MLIs, on lateral stirring in the pycnocline (e.g., Badin et al., 2011).

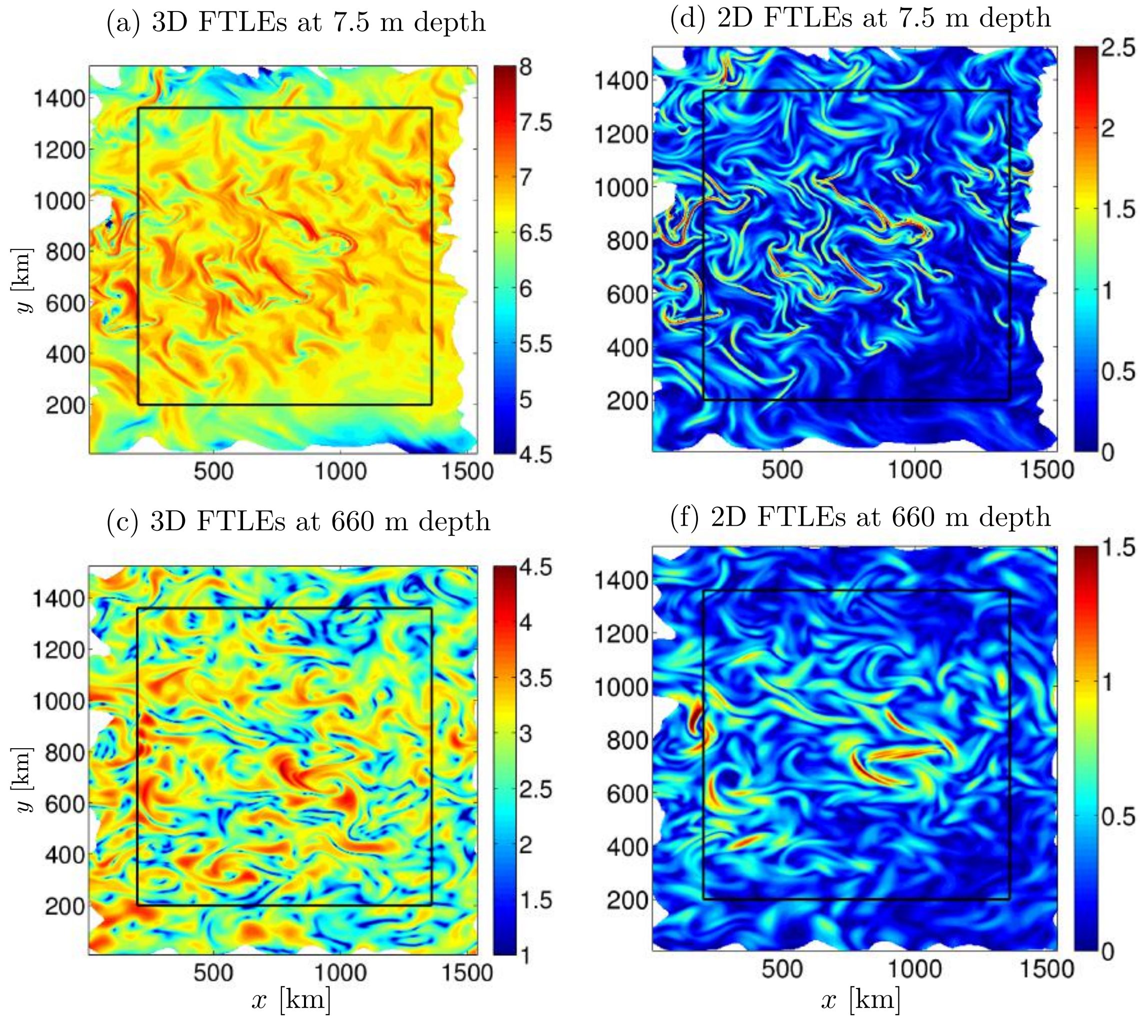

Figure 4.21: Backward in time 3D (left column) and 2D (right column) FTLEs calculated at day 290 [end of October] of the year 2011 in the Central Atlantic Ocean at (a, c) 7.5 m and (b, d) 660 m depths. Different colorbars are used to enable a clear visualization of features at the surface and ocean interior.

The analysis of average vertical profiles shows that winter and summer 3D FTLEs display minimal differences in magnitude, in the topmost levels of the ocean in this region. In summer, 3D FTLEs are intensified at the ocean surface and display a tendency for constant values at depths just beneath the shallow ML, below which they quickly decrease with depth. In winter instead, a steady decrease of 3D FTLEs is noticed, but here, the same decrease with depth is maintained in the nearest ~70 m above and below the ML after which, the winter and summer FTLEs coincide with each other (Fig. 4.22a). The larger 3D FTLEs seen in summer than in winter in the topmost levels may probably indicate that the net stirring imparted by mesoscale vortices, which dominate the ocean surface in summer, is more energetic than that which results from the small scale features, that dominate in winter.

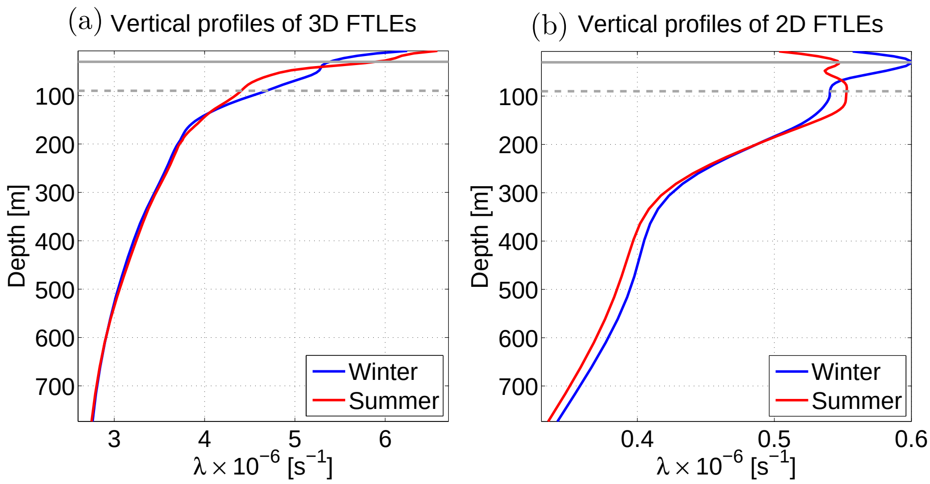

Figure 4.22: Average vertical profiles of (a) 3D FTLEs and (b) 2D FTLEs calculated for the region in the Central Atlantic Ocean. Also indicated are the lines marking the average ML depth in summer (gray continous) and winter (gray broken) lines, respectively. Note that different scales are used for 3D and 2D FTLEs due to the large difference in magnitude between them.

The small scale features observed at the ocean surface in winter, do not generate larger 3D FTLEs to surpass those effected by mesoscale vortices and frontal structures observed in summer (see Fig. 4.19). It is also observed that 3D FTLEs are intensified only at the surface, weakening only a few metres below the ML. Further, the influence of instabilities persists into the interior yielding values higher than those of the summer 3D FTLEs. At ~ 200 m, the two curves converge to each other, what probably means that other dynamics, for example, intra-thermocline vortices, which are independent of seasons start to control the flow at deeper levels of the ocean (Fig. 4.22 a). The 2D FTLEs instead reveal a more complex vertical structure, with larger values in winter than summer for the first ~ 70 km. At depths of ~ 200 m and more, 2D FTLEs calculated for winter are larger than those obtained in summer (Fig. 4.22 b).

4.3.2 Seasonality of FTLEs

We now investigate the seasonality of FTLEs for the region in the Central Atlantic ocean, where the dynamics lead to shallow mixed layers than those observed for the case study region in the North East Atlantic ocean. The relationship between stirring at scales below 100 km and MLD reported by previous studies (e.g., Sasaki et al., 2014) and also realised for the region in the North East Atlantic ocean in this thesis lead us to investigate the dependence of the seasonal cycle of FTLEs on the MLD and its vertical structure.

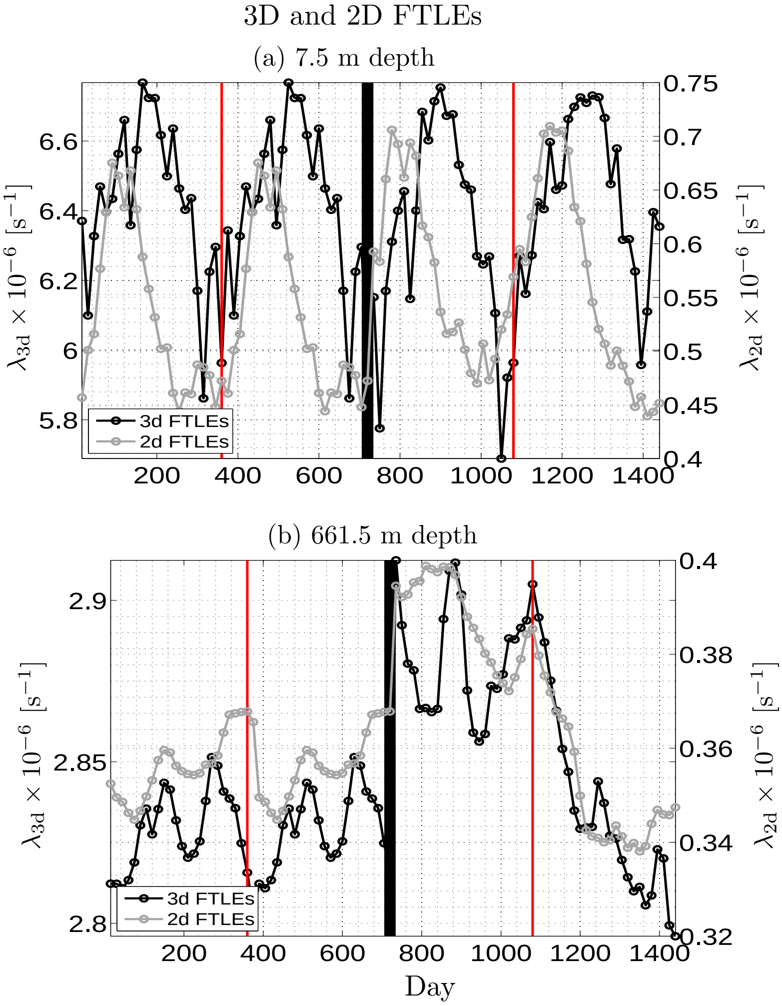

Figure 4.23: Time series of 3D FTLEs (black line) and 2D FTLEs (gray line) at (a) 7.5 m depth and (b) 661.5 m depth for the years 2006, 2007, 2010 and 2011. Red lines separate the different years and the thick vertical black line emphasizes the jump between the year 2007 and 2010.

At the ocean surface, FTLEs display a clear seasonal cycle with 3D FTLEs reaching maximum values in spring and minimum values in late summer. The 2D FTLEs instead reach maximum values in winter and decrease quicker than 3D FTLEs, displaying long tails and reaching their lowest values in summer (Fig. 4.23a). In the ocean interior, no pronounced seasonal cycle is displayed by FTLEs and also no clear relationship can be drawn between the time series of 3D and 2D FTLEs in the ocean interior (Fig. 4.23b).

At the ocean surface, the EKE (4.1) displays more variability than FTLEs showing dominant maxima in summer and reaching minimum values in winter. In general, there is only a weak correlation between EKE and FTLEs at the ocean surface (Fig. 4.24 a,b). The phase difference between the time when FTLEs and EKE reach their respective maxima and minima, suggest that FTLEs on the surface are not fully controlled by EKE in isolation but are modulated by a combination of multiple factors, for example, the mean flow. In the ocean interior instead, the EKE is noticed to correlate with the time series of FTLEs, reaching maxima and minima at approximately the same time (Fig. 4.24 c,d) .

In the idealised simulations in Chapter 3, it was found that the vertical shear of horizontal velocities plays an important role in setting the values of 3D FTLEs at all depths. To establish whether this finding is robust and persistent in a more realistic setting as is considered in this Chapter, we compare the time series of FTLEs and the vertical shear of horizontal velocities. In the ML, the seasonal cycle of the vertical shear of horizontal velocities correlates well with that of 3D FTLEs (Fig. 4.25 b), displaying maximum values in spring and minimum values in winter. As already

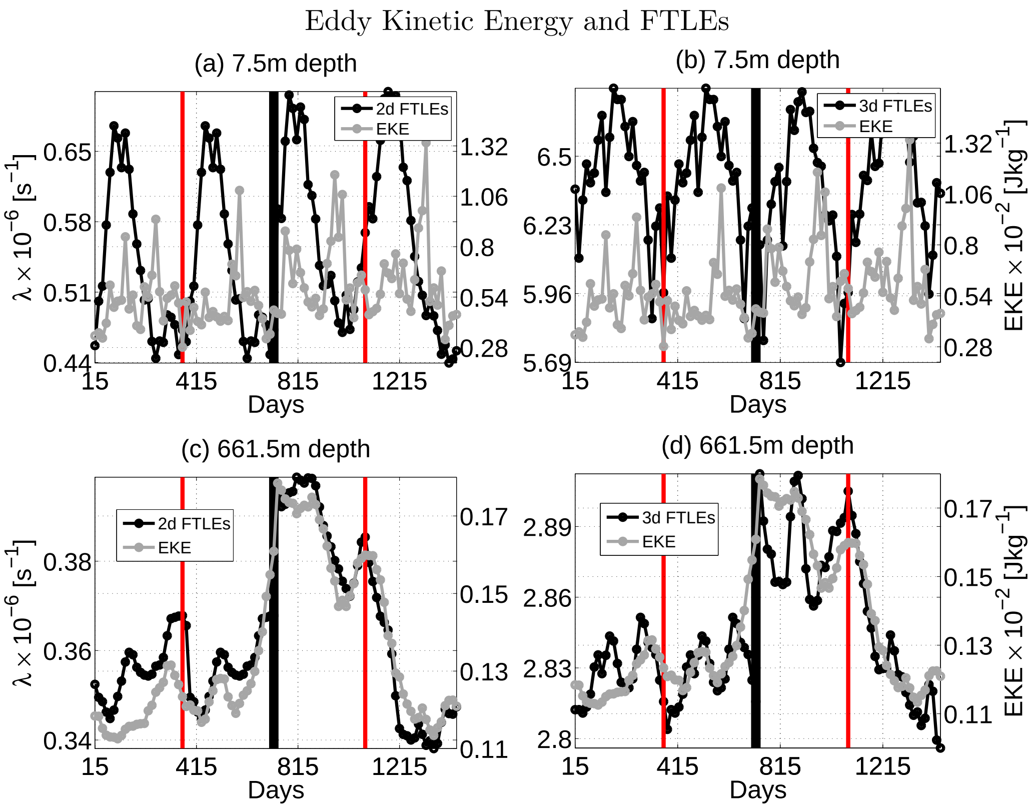

Figure 4.24: Timeseries of 2D FTLEs (black lines in left panels), 3D FTLEs (black lines in right panels) and Eddy Kinetic Energy (gray lines) at (a, b) 7.5 m depth and (c, d) 661.5 m depth over the years 2006, 2007, 2010 and 2011 for the region in the Central Atlantic Ocean.

reported in figure 4.23, the 2D FTLEs display long tails, decreasing much quicker than the vertical shear of horizontal velocities (Fig. 4.25 a).

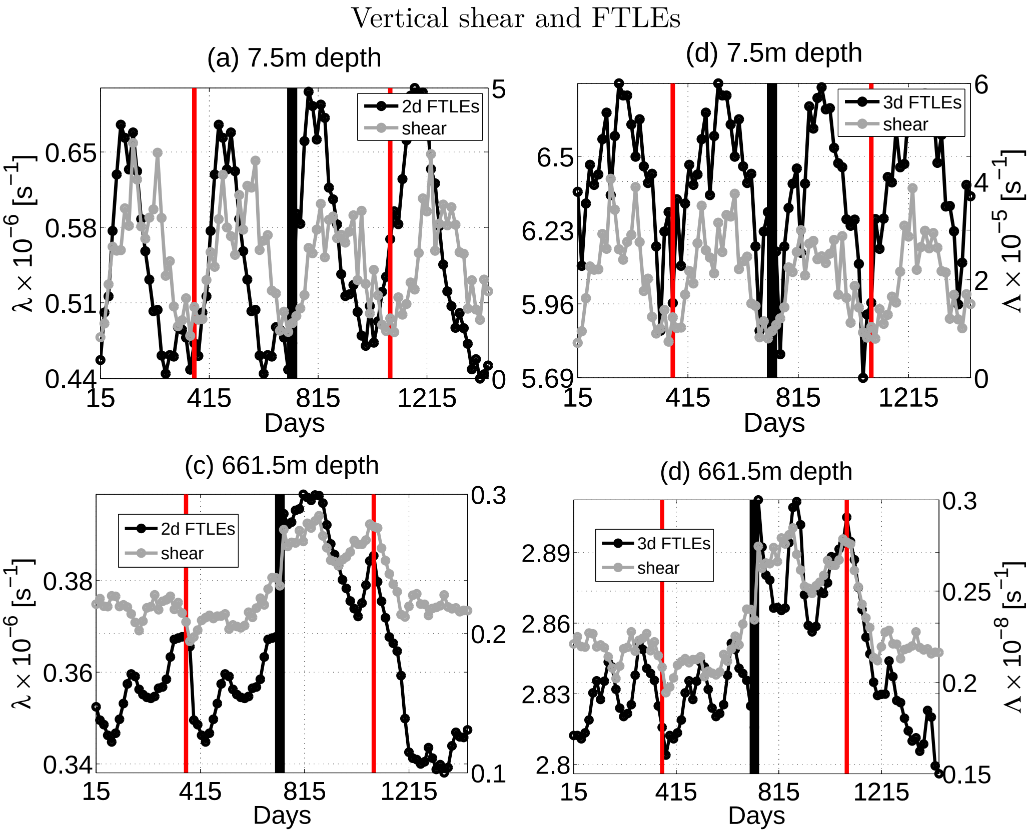

Figure 4.25: Timeseries of 2D FTLEs (black lines in left panels), 3D FTLEs (black lines in right panels) and root mean square value of the vertical shear of horizontal velocities (gray lines) at (a,b) 7.5 m depth and (c, d) 661.5 m depth over the years 2006, 2007, 2010 and 2011 for the region in the Central Atlantic Ocean.

In the pycnocline, except for a delay of $\sim$ 15 days, the dominant maxima of FTLEs and vertical shear of horizontal velocities coincide. It can thus be concluded that the seasonal cycle of FTLEs in the ocean interior is controlled by the vertical shear of horizontal velocities (Fig. 4.25 c,d).

To establish the role of ML baroclinic instabilities in modulating the seasonal cycle of FTLEs, as already noted for the region in the North East Atlantic ocean, the MLD and APE are used as indicators of the dominance or non dominance of these instabilities (e.g., Sasaki et al., 2014). The MLD displays a consistent seasonal cycle, reaching maximum values in late winter (end of March) and minimum values in late summer (Fig. 4.26). Correspondingly, the APE attains maximum values in winter when the MLs are deep and its minimum values in summer when the ML is shallow (see Fig. 4.27). The APE is however noticed to decay from its maxima slower than the MLD since the baroclinic instabilities, which draw the APE require time to reach finite amplitude of the order of days (e.g., Boccaletti et al., 2007).

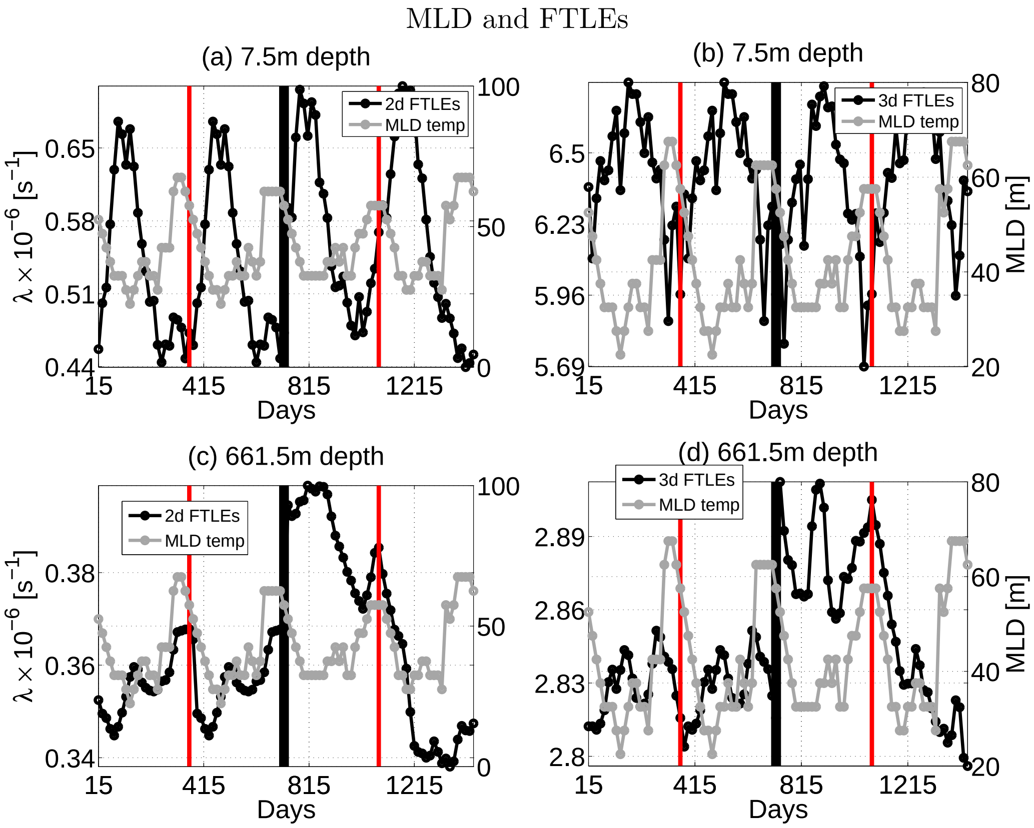

Figure 4.26: Timeseries of 2D FTLEs (black lines in left panels), 3D FTLEs (black lines in right panels) and mixed layer depth (gray lines) at (a, b) 7.5 m depth and (c, d) 661.5 m depth during the years 2006, 2007, 2010 and 2011 for the region in the Central Atlantic Ocean. Red lines separate the different years and the thick vertical black line emphasizes the jump between the year 2007 and 2010.

The APE reaches its maximum earlier than the MLD, as the depth of the ML increases with time, since the ocean water takes much longer to release the latent heat. Further, the discrepancies between the APE and FTLEs in the ocean interior can be explained by the fact that the efficiency of the conversion of APE into EKE is dependent upon other factors, like the presence of lateral buoyancy gradients (e.g., Capet et al., 2008). In support of this, the idealised simulations in Chapter 3 which differed from each other in terms of the lateral density gradient used to initialize the ML front, show that more energetic instabilities (hence large EKE values) are produced with increasing values of the lateral buoyancy gradients used.

4.3.3 Spectra

In the ML during winter, wave number energy spectra $E(k)$ display slopes of -3 or steeper at scales smaller than 50 km corresponding to nonlocal dynamics, for which motions at a given scale are controlled by velocity field features of a larger scale. The small Rossby radius of deformation in the ML (Table 4.1) make it impossible to display the inertial range for scales smaller that the ML deformation radius (Fig. 4.28a). Also, caution should be taken in explaining the steepest part of the spectra

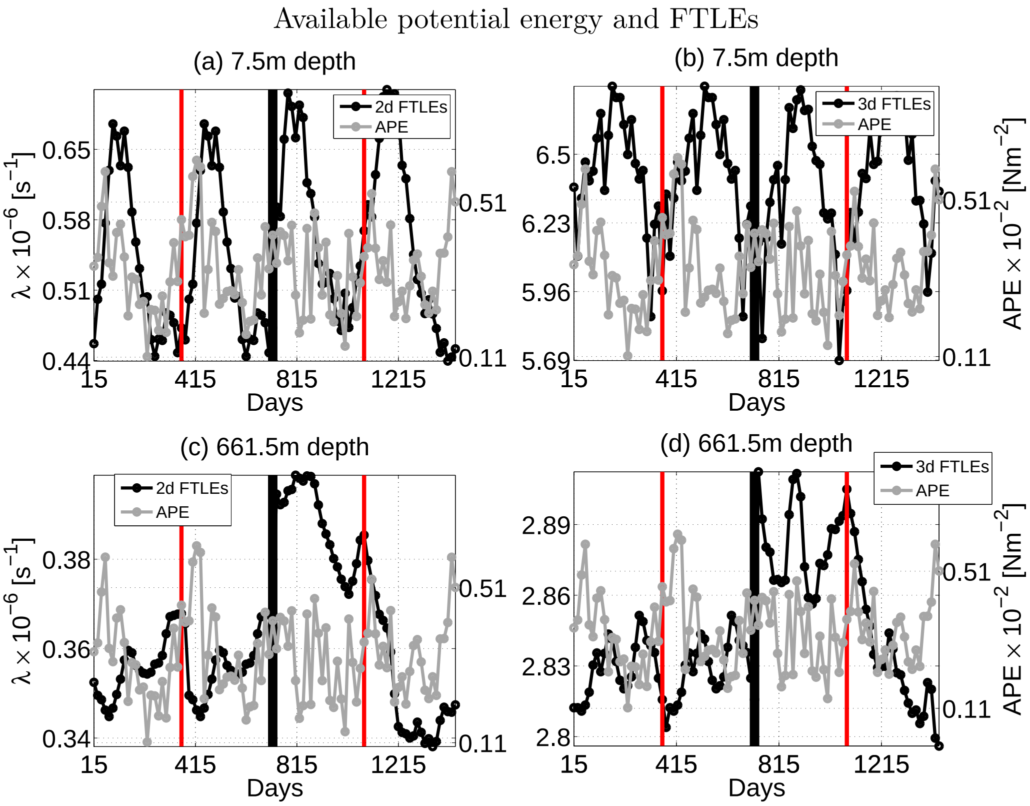

Figure 4.27: Timeseries of 2D FTLEs (black lines in left panels), 3D FTLEs (black lines in right panels) and the available potential energy (gray lines) at (a,b) 7.5 m depth and (c, d) 661.5 m depth during the years 2006, 2007, 2010 and 2011 for the region in the central Atlantic ocean. Red lines separate the different years and the thick vertical black line emphasizes the jump between the year 2007 and 2010.

since such scales are dominated by the model grid noise. At scales larger than 50 km, the $E(k)$ spectrum shows more gentle slopes (with $\alpha < 3$) corresponding to local dynamics, where motions at a given scale are controlled by velocity field features of comparable scales. The gentle slope part of the spectra is due to the mesoscale vortices, which dominate the ocean surface in winter (see Fig. 4.18 a,b,c). FTLE spectra, here considered as proxies for passive tracer, display -2 slopes corresponding to frontal dynamics for scales starting at $\sim$ 120 km and below. At scales above 120 km, passive tracer spectra become more gentle, transitioning from -2 to -1 slopes, corresponding to local diffusion. Interestingly, both 3D and 2D FTLEs show dominant maxima at similar positions, due to the fact both fields show ridges in similar locations (Fig. 4.28 b,c).

In the pycnocline, energy spectra show slopes steeper than -3 at all scales below the first baroclinic deformation radius, which corresponds to nonlocal dynamics (Fig. 4.28d). This is also observed from the Eulerian diagnostics which reveal a disappearance of small scale structures and a predominance of large scales, particularly, frontal structures (Fig. 4.18 d,e,f). The respective passive tracer spectra instead show two regimes: one with a -2 slope corresponding to frontal dynamics, for scales below $\sim$ 100 km and another with -1 slope corresponding to nonlocal diffusion, for

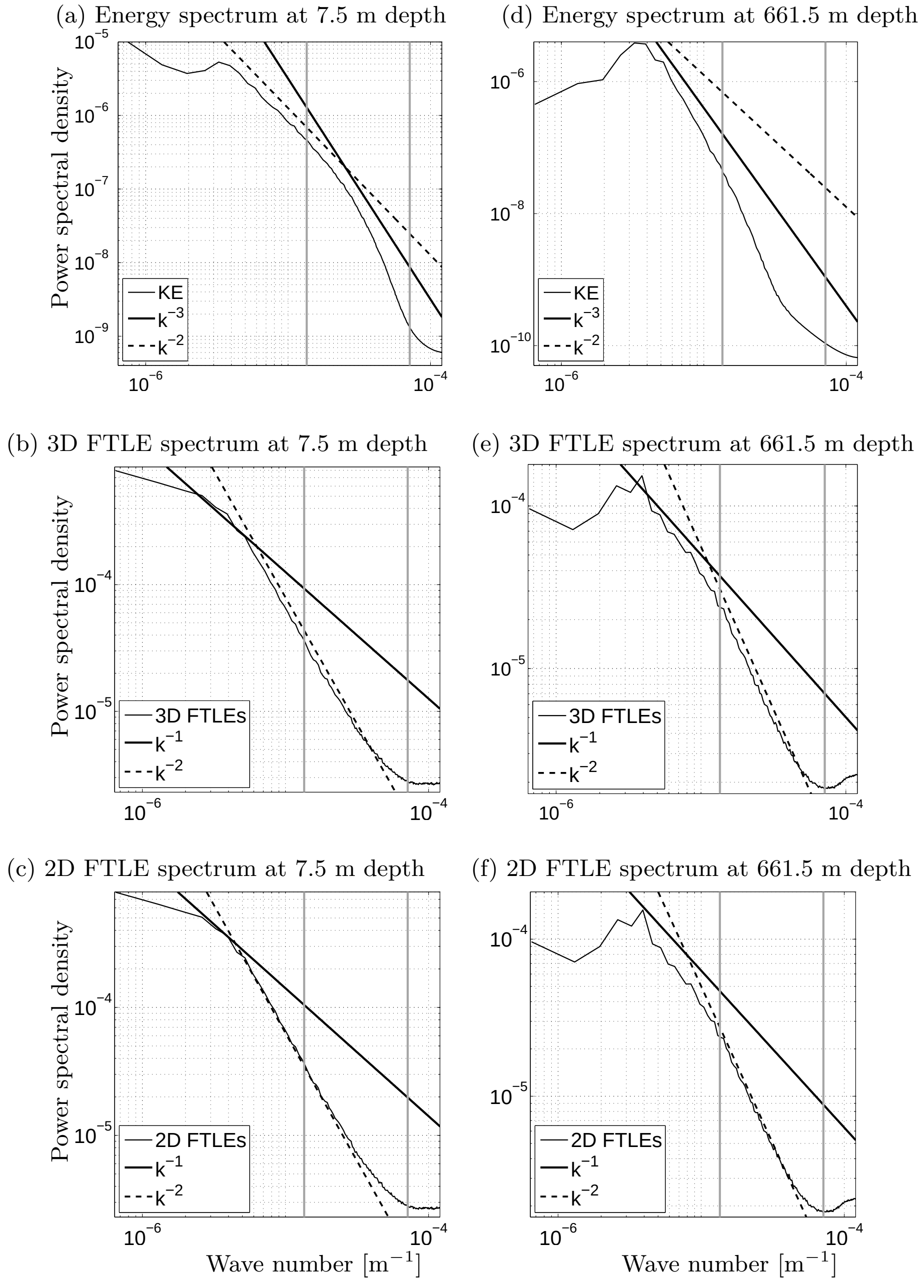

Figure 4.28: Winter Spectra of kinetic energy calculated at (a) 7.5 m depth and (d) 661.5 m depth. 3D FTLE spectra averaged for the winter season at (b) 7.5m depth and (e) 661.5 m depth. 2D FTLE spectra calculated at (c) 7.5 m depth and (f) 661.5 m depth, all for the region in the Central Atlantic Ocean. On each panel, gray lines show the location of the ML (left) and first baroclinic (right) deformation radii.

scales above 100 km.

In summer, energy spectra display -3 slopes or steeper for scales smaller than ~ 100 km, indicative of nonlocal dynamics. At scales above 100 km, the spectra displays a more gentle slope close to -2 (Fig. 4.29a), which may be attributed to mesoscale

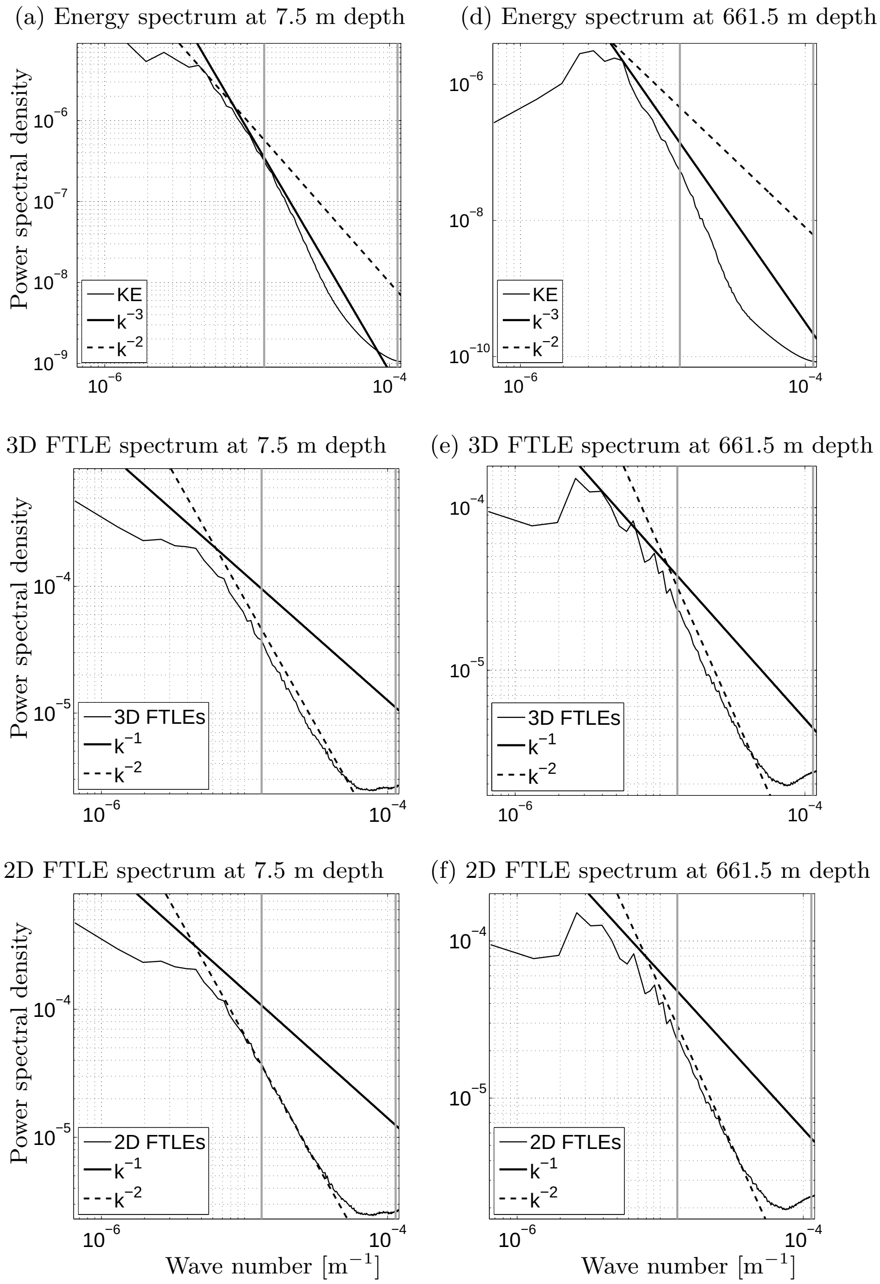

Figure 4.29: Summer Spectra of kinetic energy calculated at (a) 7.5 m depth and (d) 661.5 m depth. 3D FTLE spectra averaged for the summer season at (b) 7.5m depth and (e) 661.5 m depth. 2D FTLE spectra calculated at (c) 7.5 m depth and (f) 661.5 m depth, all for the region in the Central Atlantic Ocean. On each panel, the gray line shows the location of the first baroclinic deformation radius.

vortices and frontal structures that are noticed to dominate the ocean surface in summer (see Fig. 4.19 a,b,c). The more gentle slopes of the energy spectra observed at the ocean surface in winter (compare to Fig. 4.28a) are not displayed at scales above $\sim$ 100 km in summer, as already shown by the Eulerian diagnostics that the mesoscale vortices and submesoscale filaments reduce in intensity during the summer as the ML becomes more shallow limiting the growth of the baroclinic instabilites (e.g., Boccaletti et al., 2007). The respective FTLE spectra display -2 slopes characteristic of frontal structures for all scales below $\sim$ 140 km, and -1 slopes for scales above 140 km, which correspond to nonlocal dynamics as predicted by the energy spectra (Fig. 4.29 b,c). In the pycnocline, energy wave number spectra show slopes steeper than -3 for all scales below 140 km, thus predicting nonlocal dynamics (Fig.4.29 d). The respective passive tracer spectra calculated from FTLEs display two regimes: a -1 slope regime for scales above $\sim$ 100 km consistent with the nonlocal dynamics predicted by the energy spectra and a -2 slope regime characteristic of frontal structures (Fig. 4.29 e,f).

4.4 Summary and Discussion

In this Chapter, we have explored the seasonality of ML turbulence and how it in turn modulates the seasonal cycle of FTLEs. Two contrasting (in terms of the MLDs) case study regions of the Atlantic ocean, one in the North East and another in the Central Atlantic ocean are considered. In the two regions, the MLD displays a clear seasonal cycle, attaining large values in winter and becoming shallower in summer. Deepening of the ML in winter leads to a dominance of submesoscale filaments and vortices, by energizing baroclinic instabilities via the APE stored in the quasi-vertical isopycnals (Boccaletti et al., 2007). In summer when the ML is relatively shallower, the height of the isopycnals is reduced, which essentially translates into a shrinking of the APE reservoir from which MLIs draw, hence their weakening (Fox-Kemper and Ferrari, 2008). Indeed, wave number spectra calculated at the ocean surface become less steep in winter, implying local dynamics due to the energetic small scales and steepen in summer, when the small scale features disappear and the domain is dominated by a mesoscale field. We have calculated time series of 3D and 2D FTLEs with a total span of 4 years and we have compared them to time series of EKE (capturing the stirring influence of instabilities ignoring the mean flow), MLD, APE and vertical shear of horizontal velocities.

At the ocean surface and in the two case study regions, 2D FTLEs reach their maxima earlier than the 3D FTLEs, while time series of both 2D and 3D FTLEs correlate well in the pycnocline, displaying maxima and minima at approximately the same instant. In agreement with the findings of the idealised simulations in Chapter 3, the vertical shear of horizontal velocities is noticed to determine the magnitude of 3D FTLEs in the two case study regions, with the two diagnostics displaying time series which correlate well. It has also been noticed that 3D FTLEs show minimal differences at the surface during summer and winter, while differences emerge in the subsurface levels, yielding large FTLE values in winter when the MLIs are stronger due to deep MLs. Significant differences are realised between winter and summer 2D FTLEs at the surface and interior ocean levels, showing a strengthening of stirring in winter and a weakening in summer.

Except at the surface, where 3D FTLEs display a relatively non clear behavior, with maxima in early summer and minima in late summer, time series of FTLEs in the two case study regions correlate well with EKE, highlighting a seasonality in the stirring intensity of the flow, that is, a maximum in winter and a minimum in summer. Time series of the MLD and APE also closely follow those of EKE suggesting the importance of baroclinic instabilities in enhancing the eddy (residual) field of the flow. The enhancement of small scale turbulence in winter and its decay in summer has been reported in previous studies (e.g., Qiu and Kelly, 1993; Sasaki et al., 2014) as an indirect consequence of large scale atmospheric forcing, which through ML deepening, leads to a build-up of APE in the body of the ML. Baroclinic instabilities in the ML are energized by the release of this APE, leading to restratification of the upper ocean at the end of the cycle.

In this Chapter, it has thus been found that time series of FTLEs, which are a diagnostic that quantifies stirring effected by a flow, display a clear seasonal cycle similar to that of MLIs or their proxies like MLD and APE. The seasonal cycle of 2D FTLEs is modulated entirely by EKE at all depths. At the surface, 3D FTLEs show a seasonal cycle reaching maximum FTLE values in late summer and reaching values in mid winter; thus displaying a cycle which does not correlate with the EKE (hence 2D FTLEs). In the subsurface and interior ocean levels, 3D FTLEs display a seasonal cycle close to that of 2D FTLEs (and hence EKE).

Chapter 5

Summary and Outlook

In this Chapter, a general summary of the thesis, outlining the main results and how the different research questions in Section 1.1 have been addressed, is provided. Finally, an outlook for future research in connection to the findings in this thesis is provided.

5.1 Summary

In this thesis, our main goal was to explore the chaotic stirring that is imparted by submesoscale processes arising in the oceanic ML. To address this, we have considered a current in an idealised zonal channel undergoing baroclinic instability, with a ML front whose adjustment is known to produce MLIs. Due to the inability of Eulerian diagnostics to detect MLIs in the form of filaments, we have instead used Lagrangian diagnostics - the FTLEs, to detect these MLIs and quantify the chaotic stirring they impart to the flow. It has been found that while Eulerian quantities, such as the Okubo-Weiss parameter, yield relatively less features, FTLEs display more complexity, confirming previous studies that regular velocity fields can produce chaotic particle trajectories. 3D and 2D FTLEs display ridges and hence spectra peaks in the same locations. PDFs of backward FTLEs, which are proxies to passive tracer are found to be non Gaussian, thus suggesting the need for non diffusive parameterization schemes for processes due to MLIs.

By setting individual terms of the flow deformation tensor to zero, we have found that vertical velocities are less important in determining the structure and magnitude of FTLEs, confirming previous studies that the enhancement of vertical velocities to within 4 orders of magnitude lower than horizontal velocities does not make their contribution to stirring stronger. Instead, the vertical shear of horizontal velocities determines the structure and magnitude of 3D FTLEs, with the vertical shear also enhancing stirring in the ocean interior. The 2D FTLEs instead which are surface intensified and quickly decay below the ML base. We have also found that 3D FTLEs are approximately twice as large as 2D FTLEs. However, it was shown for the realistic ocean dataset, that 3D FTLEs can be much larger than twice the 2D FTLEs. It is thus concluded that the vertical shear of horizontal velocities enhances stirring, which is in agreement with earlier theoretical findings (Haynes, 2001) that the vertical shear provides a more efficient mechanism of stirring. Assuming thermal wind balance, domination of 3D FTLEs by the vertical shear of horizontal velocities allowed a derivation of a scaling law between FTLEs and the density gradient used to initialize the ML front. The scaling law converges to the numerical values of FTLEs in the pycnocline while it diverges from it at the surface, where ageostrophic MLIs are predominant.

To investigate how the skeleton of ML turbulence responsible for chaotic stirring looks like, Lagrangian Coherent Structures (LCSs), which constitute the skeleton that constrains the flow into dynamically distinct regions, were calculated from the geodesic theory, allowing to obtain elliptic (e.g., vortices) and hyperbolic (e.g., filaments) LCSs. We have confirmed previous findings that the relationship between LCSs and ridges of FTLEs is not one-to-one, with attracting LCSs (ALCSs) and repelling LCSs (RLCSs) revealing a complex web of LCSs. Vortices are displayed as elliptic LCSs from which a variety of ALCSs and RLCSs spreads. The complexity of LCSs is higher at the surface due to the entanglement caused by the relatively stronger flow, which repeatedily stretches and folds fluid patches at the channel surface. The observed complex structures of LCSs associated to MLIs can be important for the characterization of mixing and the transfer of nutrients and other passive tracers at the ocean surface (e.g., Lévy et al., 2001), as well as provide the landscape for the growth of different phytoplankton species (d'Ovidio et al., 2010). Also, the possibility of obtaining LCSs as explicitly parameterized curves and/or surfaces, may be useful in predicting flow paths of substances, such as oil spills (e.g., Olascoaga and Haller, 2012) imparted by energetic MLIs.

In order to understand how our findings from the idealised setting of a ML front relate to a more realistic setting, in which noise induced by surface winds and/or internal waves are likely to change the flow dynamics, we have considered a dataset from a realistic ocean simulation of the Atlantic ocean in two case study regions. The two considered regions included a region in the North East Atlantic ocean and another in the low activity Central Atlantic ocean. Unlike in the idealised study, where 3D FTLEs were found to be approximately twice as large as 2D FTLEs, 3D FTLEs in the realistic setting are found to be approximately 4 times larger than 2D FTLEs. 3D FTLEs are also found to be intensified at the ocean surface, decreasing quickly in summer and gradually in winter before remaining generally constant in the pycnocline. Further, to characterize the seasonality of ML turbulence, we considered time series (over a period of 4 years) of key diagnostics such as the eddy kinetic energy and vertical shear of horizontal velocities, comparing them to the time series of the mixed layer depth (MLD), since ML deepening or shallowing has been reported as the primary response of the ocean to atmospheric forcing at the ocean surface (e.g., Sasaki et al., 2014). In this thesis, due to the correlation of time series of 2D FTLEs and EKE at the surafce and ocean interior, we conclude that the seasonal cycle of 2D FTLEs is modulated by the EKE.

Finally, we have found that 2D FTLEs display a clear seasonal cycle both at the surface and ocean interior, reaching maximum values in winter and minimum values in summer. At the ocean surface, time series of 3D FTLEs show a seasonal behaviour, reaching maxima in late summer and minima in late autumn and correlate well with time series of the vertical shear of horizontal velocities. In the ocean interior, 3D FTLEs display a similar seasonal cycle of the 2D FTLEs, thus correlating well with the time series of EKE. The most outstanding difference between time series of 2D and 3D FTLEs is at the ocean surface, where the seasonality of 3D FTLEs is modulated by the vertical shear of horizontal velocities, different from the 2D FTLEs seasonal cycle which is modulated by the EKE.

5.2 Outlook for future research

Bettencourt et al. (2012) reported a dominating role of the vertical shear of horizontal velocities in determining the vertical structure of FTLEs in the Benguela upwelling region, where the vertical velocities are 3 orders of magnitude lower than horizontal velocities. It would be interesting to extend the analysis here proposed to other kind of flows, such as idealized flows (e.g., Pratt et al., 2013; Rypina et al., 2015) and Langmuir turbulence (e.g., Van Roekel et al., 2012), in which vertical velocities are comparable to the horizontal velocities and the emerging turbulence is no longer quasi two dimensional. Further, the geodesic LCSs presented in this thesis were calculated along 2D surfaces, and an extension to a fully 3D calculation of LCSs is appealing. A number of theoretical studies have considered analytic velocity fields and calculated 3D LCSs but a realization of such a flow in a geophysical context would be interesting to investigate in order to understand the properties of the emerging LCSs and their impact on fluid stirring. A systematic identification of elliptic LCSs would also enable a good estimate of the integrated transport properties of vortices. Specifically, this would enable a more quantitative estimate of the total transport of active and passive tracers away from the main frontal regions. Also, integrating the flow longer in a future study, would lead to further understanding of the evolution of LCSs as MLIs develop. As an example, it would help reveal whether the spreading centres of ALCSs and RLCSs observed in the pycnocline develop into vortices.

For future work on the realistic ocean simulation, a consideration of longer time series of FTLEs will enable a more quantitative analysis of the seasonal cycle of FTLEs. Also with longer FTLE time series, the importance of the mean flow in modulating the seasonality of FTLEs, particularly the 3D FTLEs, which we have found in this thesis to be decorrelated from the time series of EKE and displaying a non clear behaviour could be addressed. The time series of 3D FTLEs at the ocean surface may be dependent on non seasonal factors, such as background flow changes dominated by mesoscale eddies.

Finally and more ambitiously, a consideration of more regions of the World Ocean at higher spatial and temporal resolutions would allow for a more accurate visualization of MLIs, which emerge at scales of $\mathcal{O}(1)$ km, where secondary instabilities and 3D dynamics are expected to emerge.

Appendices

Appendix A

A mechanism for the development of large-scale fronts

The contents of this Appendix have been published in the 2014 Geophysical Fluid Dynamics (GFD) summer school proceedings held at Woods Hole Oceanographic Institution (WHOI) (see Mukiibi, 2014).

A.1 Introduction

In this appendix, the downstream development of a baroclinic instability is studied in a 2-layer non-linear Quasi-Geostrophic (QG) model with a semi-infinite downstream extent and rigid meridional walls. The setup here considered describes a possible mechanism for the development of large-scale fronts. Starting with a baroclinic current in a channel, a perturbation is invoked at the entrance of the channel upstream and it's spatial and temporal downstream development is studied. For simplicity, this study considers only 2 modes in the y direction. This restriction offers two advantages: first, it is simple enough to easily follow the 2 modes, and second, it gives insight into the more complicated scenario of having more than one mode leading to interaction of the different modes and hence modifying the dynamics of the flow. The boundary conditions at the channel entrance upstream are a temporal oscillating perturbation at $x = 0$. Downstream, it imposed that the potential vorticity is zero at $x = \infty$. In the $y-$direction, the derivatives of the stream function (i.e velocity) at the meridional walls are set to zero. It has been found by Pedlosky (2011) that in a simple finite amplitude model of a spatially developing baroclinic instability, there is a regime during which the spatial and temporal evolution of the instability amplitude along x, t characteristics exhibits chaotic behaviour. In this appendix, we study numerically the factors that determine the persistence of the chaotic behaviour in a more realistic ocean model. We find that dynamics are primarily controlled by the degree of dissipation in the model. When the dissipation is high, the growth rate of instabilities is governed by the velocity shear between the layers. When instead the dissipation is low, the rate of growth of instabilities is determined by the Froude number.

A.2 The Model

Consider the QG equations for a two-layer model (Pedlosky, 1970, 2011). The formulation is given in terms of the potential vorticity q and the equations of motion in the two layers are

$$\left(\frac{\partial}{\partial t} + \mathrm{U}_1 \frac{\partial}{\partial x}\right) q^{(1)} + Q_{y1}\frac{\partial \psi^{(1)}}{\partial x} + \mathrm{J}(\psi^{(1)}, q^{(1)}) = -r\nabla^2\psi^{(1)} \ , \tag{A.1}$$

$$\left(\frac{\partial}{\partial t} + \mathrm{U}_2 \frac{\partial}{\partial x}\right) q^{(2)} + Q_{y2}\frac{\partial \psi^{(2)}}{\partial x} + \mathrm{J}(\psi^{(2)}, q^{(2)}) = -r\nabla^2\psi^{(2)}. \tag{A.2}$$

where the jacobian, J, is defined as $J(a,b) = \dfrac{\partial a}{\partial x}\dfrac{\partial b}{\partial y} - \dfrac{\partial b}{\partial x}\dfrac{\partial a}{\partial y}$, ψ is the stream function, U_i is the fluid velocity in the i^{th} layer and r is the dissipation coefficient.

From hereon, superscripts will denote the model layer and subscripts will denote the mode under consideration. For a channel with no bottom topography,

$$\begin{aligned} Q_1 &= \nabla^2\psi^{(1)} - \mathrm{F}_1(\psi^{(1)} - \psi^{(2)}) + \beta y \ , \\ Q_2 &= \nabla^2\psi^{(2)} + \mathrm{F}_2(\psi^{(1)} - \psi^{(2)}) + \beta y \ , \end{aligned}$$

where $\beta = \partial f/\partial y$, with f being the Coriolis parameter. We from hereon propose truncated Fourier series solutions to (A.1) and (A.2) of the form

$$\begin{pmatrix} q^{(1)} \\ \psi^{(1)} \end{pmatrix} = \begin{pmatrix} q_1^{(1)}(x,t)\sin\pi y + q_2^{(1)}(x,t)\sin 2\pi y + \cdots \\ \psi_1^{(1)}(x,t)\sin\pi y + \psi_2^{(1)}(x,t)\sin 2\pi y + \cdots \end{pmatrix} , \tag{A.3}$$

$$\begin{pmatrix} q^{(2)} \\ \psi^{(2)} \end{pmatrix} = \begin{pmatrix} q_1^{(2)}(x,t)\sin\pi y + q_2^{(2)}(x,t)\sin 2\pi y + \cdots \\ \psi_1^{(2)}(x,t)\sin\pi y + \psi_2^{(2)}(x,t)\sin 2\pi y + \cdots \end{pmatrix} . \tag{A.4}$$

and impose the boundary conditions

$$\begin{pmatrix} q(x=0,\infty) \\ \psi(x=0,\infty) \end{pmatrix} = \begin{pmatrix} q_o \sin\omega t \\ 0 \end{pmatrix} , \tag{A.5}$$

$$\begin{pmatrix} q(y=0,\frac{1}{2},1) \\ \psi(y=0,\frac{1}{2},1) \end{pmatrix} = \begin{pmatrix} 0 \\ 0 \end{pmatrix} , \tag{A.6}$$

where q_o is a constant. Substituting (A.3) into (A.1) and projecting onto sinπy and sin$2\pi y$ yields (A.7) and (A.8) respectively

$$\begin{aligned} \left(\frac{\partial}{\partial t} + \mathrm{U}_1 \frac{\partial}{\partial x}\right) q_1^{(1)} + Q_{y1}\frac{\partial \psi_1^{(1)}}{\partial x} - \frac{\pi^2}{2} q_2^{(1)}\frac{\partial \psi_1^{(1)}}{\partial x} + \frac{\pi^2}{4} q_1^{(1)}\frac{\partial \psi_2^{(1)}}{\partial x} \ - \\ \frac{\pi^2}{4}\psi_1^{(1)}\frac{\partial q_2^{(1)}}{\partial x} + \frac{\pi^2}{2}\psi_2^{(1)}\frac{\partial q_1^{(1)}}{\partial x} = -r q_1^{(1)} \ , \end{aligned} \tag{A.7}$$

$$\left(\frac{\partial}{\partial t}+\mathrm{U}_1\frac{\partial}{\partial x}\right)q_2^{(1)}+Q_{y1}\frac{\partial\psi_2^{(1)}}{\partial x}+\frac{\pi^2}{4}q_1^{(1)}\frac{\partial\psi_1^{(1)}}{\partial x}-\frac{\pi^2}{4}\psi_1^{(1)}\frac{\partial q_1^{(1)}}{\partial x}=-rq_2^{(1)}. \qquad \text{(A.8)}$$

In the reduced model, (A.7) and (A.8) are the equations of motion in layer 1. Following the same steps above but with the variables $q_i^{(2)}$ and ψ_i^2 for $i=1,2$, the equations of motion in layer 2 are:

$$\left(\frac{\partial}{\partial t}+\mathrm{U}_2\frac{\partial}{\partial x}\right)q_1^{(2)}+Q_{y2}\frac{\partial\psi_1^{(2)}}{\partial x}-\frac{\pi^2}{2}q_2^{(2)}\frac{\partial\psi_1^{(2)}}{\partial x}+\frac{\pi^2}{4}q_1^{(2)}\frac{\partial\psi_2^{(2)}}{\partial x}-$$
$$\frac{\pi^2}{4}\psi_1^{(2)}\frac{\partial q_2^{(2)}}{\partial x}+\frac{\pi^2}{2}\psi_2^{(2)}\frac{\partial q_1^{(2)}}{\partial x}=-rq_1^{(2)}\ , \qquad \text{(A.9)}$$

$$\left(\frac{\partial}{\partial t}+\mathrm{U}_2\frac{\partial}{\partial x}\right)q_2^{(2)}+Q_{y2}\frac{\partial\psi_2^{(2)}}{\partial x}+\frac{\pi^2}{4}q_1^{(2)}\frac{\partial\psi_1^{(2)}}{\partial x}-\frac{\pi^2}{4}\psi_1^{(2)}\frac{\partial q_1^{(2)}}{\partial x}=-rq_2^{(2)}. \qquad \text{(A.10)}$$

Linearising (A.7), (A.8), (A.9) and (A.10) yields a set of equations from which the linear stability of the equations can be investigated. We further suppose normal mode ansatz for the potential vorticity and stream function of the form:

$$q_j^{(\ell)}=\hat{q}_j^{(\ell)}\mathrm{e}^{ik(x-ct)}\quad\text{and}\quad\psi_j^{(\ell)}=\hat{\psi}_j^{(\ell)}\mathrm{e}^{ik(x-ct)}\quad\text{for}\quad\ell=1,2;\quad j=1,2\ , \qquad \text{(A.11)}$$

where x is the downstream coordinate and k is the x-direction wave number. After substituting (A.11) into the system of equations (A.7 - A.10), the linearised combination of equations (A.7) and (A.9) can be written in matrix form as

$$\begin{pmatrix} r+ik(\mathrm{U}_1-c)-\dfrac{ikQ_{y1}(\mathrm{K}_1^2+\mathrm{F}_2)}{\mathrm{K}_1^2(\mathrm{K}_1^2+\mathrm{F}_1+\mathrm{F}_2)} & \dfrac{-ikQ_{y1}\mathrm{F}_1}{\mathrm{K}_1^2(\mathrm{K}_1^2+\mathrm{F}_1+\mathrm{F}_2)} \\ \dfrac{-ikQ_{y2}\mathrm{F}_2}{\mathrm{K}_1^2(\mathrm{K}_1^2+\mathrm{F}_1+\mathrm{F}_2)} & r+ik(\mathrm{U}_2-c)-\dfrac{ikQ_{y2}(\mathrm{K}_1^2+\mathrm{F}_1)}{\mathrm{K}_1^2(K_1^2+\mathrm{F}_1+\mathrm{F}_2)}\end{pmatrix}\begin{pmatrix}\hat{q}_1^{(1)}\\ \hat{q}_1^{(2)}\end{pmatrix}=0 \qquad \text{(A.12)}$$

where $\mathrm{K}_1^2=k^2+\pi^2$ and k is the zonal wave number.

The linearised forms of (A.8) and (A.10) take a similar form and can be written as a matrix in the same form as (A.12) but with $\mathrm{K}_2=k^2+2\pi^2$. For non-trivial solutions, the determinant of the matrix in (A.12) must vanish, thus,

$$\left(r+ik(\mathrm{U}_1-c)-\frac{ikQ_{y1}(\mathrm{K}_1^2+\mathrm{F}_2)}{\mathrm{K}_1^2(\mathrm{K}_1^2+\mathrm{F}_1+\mathrm{F}_2)}\right)\left(r+ik(\mathrm{U}_2-c)-\frac{ikQ_{y2}(\mathrm{K}_1^2+\mathrm{F}_1)}{\mathrm{K}_1^2(K_1^2+\mathrm{F}_1+\mathrm{F}_2)}\right)-$$
$$\left(\frac{-ikQ_{y1}\mathrm{F}_1}{\mathrm{K}_1^2(\mathrm{K}_1^2+\mathrm{F}_1+\mathrm{F}_2)}\right)\left(\frac{-ikQ_{y2}\mathrm{F}_2}{\mathrm{K}_1^2(\mathrm{K}_1^2+\mathrm{F}_1+\mathrm{F}_2)}\right)=0. \qquad \text{(A.13)}$$

Because we are interested in dynamics at scales comparable to the deformation radius in the ocean, we ignore the β-effect from our consideration and also define the velocity shear $\mathrm{U}_s=\mathrm{U}_1-\mathrm{U}_2$ as the difference of fluid velocities in the two layers. Assuming also that $\mathrm{F}_1=\mathrm{F}_2=\mathrm{F}$, yields a simple form of the derivatives of Q:

$$Q_{y1}=\mathrm{FU}_s,\quad Q_{y2}=-\mathrm{FU}_s\ , \qquad \text{(A.14)}$$

and thus

$$Q_{y1} + Q_{y2} = 0, \quad Q_{y1} \cdot Q_{y2} = -\mathrm{F}^2 \mathrm{U}_s^2 \ . \tag{A.15}$$

Equation (A.13) yields a quadratic equation in c whose solution is obtained as

$$c = \left(-i\frac{r}{k} + \frac{1}{2}(\mathrm{U}_1 + \mathrm{U}_2)\right) \pm \frac{\mathrm{U}_s}{2}\left(1 - 4\mathrm{F}\left(\frac{\mathrm{F}^3}{y^2} - \frac{\mathrm{F}x^2}{y^2} + \frac{x}{y}\right)\right)^{1/2} \tag{A.16}$$

where, $\quad x = \mathrm{K}_1^2 + \mathrm{F}, \quad y = \mathrm{K}_1^2(\mathrm{K}_1^2 + 2\mathrm{F})$ and thus

$$c - \mathrm{U}_B = -i\frac{r}{k} \pm \frac{\mathrm{U}_s}{2}\left(\frac{\mathrm{K}_1^2 - 2\mathrm{F}}{\mathrm{K}_1^2 + 2\mathrm{F}}\right)^{1/2} . \tag{A.17}$$

Thus c is generally complex and can be written as

$$c = c_r + ic_i \ , \tag{A.18}$$

where c_r and c_i are the real and imaginary parts of c respectively. In case the term in the last parentheses vanishes, then the dispersion relation reduces to

$$c = \left(-i\frac{r}{k} + \mathrm{U}_B\right) \ , \tag{A.19}$$

where, $\mathrm{U}_B = \frac{1}{2}(\mathrm{U}_1 + \mathrm{U}_2)$ is the barotropic velocity.

From (A.19), it is possible to see that the decay of the perturbation is proportional to the dissipation in the system and is higher for lower wave numbers. In this case, the shear does drop out of the dispersion relation rendering the dissipation, r, and the magnitude of the barotropic flow as the only effective parameters governing the growth rate of instabilities in the channel under consideration. However if $\mathrm{K}_1 < (2\mathrm{F})^{1/2}$, then the terms in (A.17) also contribute to the complex part of c and in turn the shear, U_s and the Froude number, F become effective parameters of the system too.

In what follows, two sets of simulations are carried out; the first being the case when the dissipation $r = \mathcal{O}(1)$ and the second being the case when the dissipation in the system is almost zero i.e $r = \mathcal{O}(\Delta)$ for very small Δ.

(i) $r = \mathcal{O}(1)$
When the dissipation in the model is high, growing modes of instabilities are only obtained when $2\mathrm{F} > \mathrm{K}_1^2$ and the product of the now imaginary term in the parentheses of (A.17) and $\mathrm{U}_B/2$ must be large enough to outweigh the decay term $-i\frac{r}{k}$. This yields the relation for the marginal condition on U_s in order to have a growing instability.

$$\mathrm{U}_s = \frac{2r}{k}\left(\frac{2\mathrm{F} + \mathrm{K}_1^2}{2\mathrm{F} - \mathrm{K}_1^2}\right)^{1/2} \tag{A.20}$$

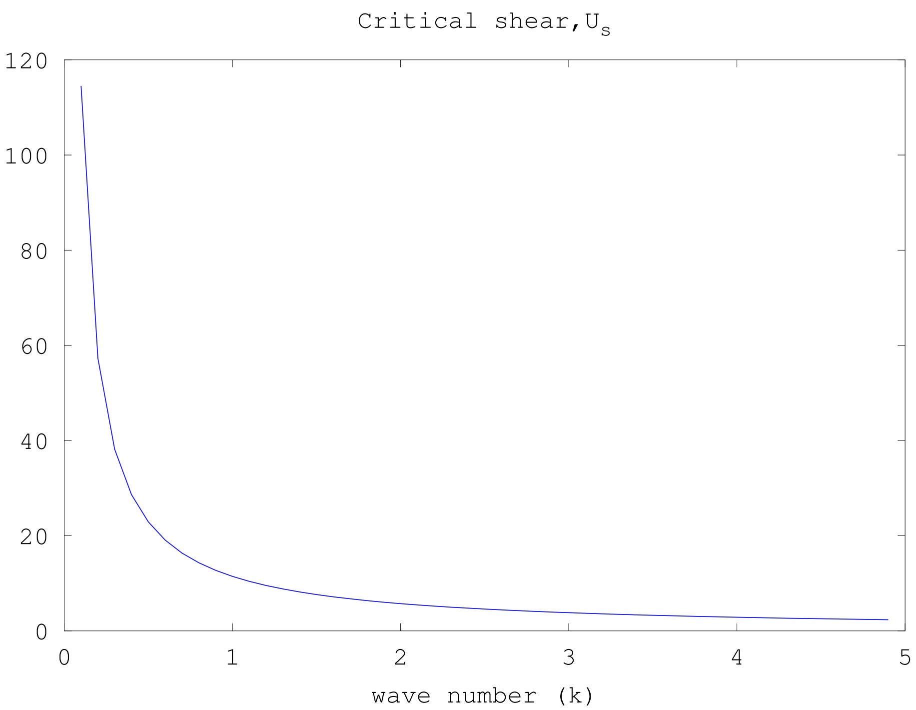

Figure A.1: Critical dependence of the velocity shear U_s as a function of the zonal wavenumber k.

For the selected values, $r = 4.6, \mathrm{F} = 40, l = \pi$ and $0 < k < 5$ (Pedlosky, 2011), $U_s = U_s(k)$ is noticed to exhibit a hyperbolic dependence as a function of the zonal wave number k (see Fig. A.1).

(ii) $r = \mathcal{O}(\Delta)$
When the model dissipation r is low, the marginal curve is given in terms of the parameter F, the Froude number, and takes the form

$$\mathrm{F} = \frac{\mathrm{K}_1^2}{2} = \frac{k^2 + l^2}{2} \ , \tag{A.21}$$

thus yielding a parabolic dependence of F as a function of the zonal wave number, with a minimum at $k = 0$ and takes the shape in Fig. A.2:

A.3 Numerical Simulations and Results

In what follows, results emerging from nonlinear numerical simulations of the the reduced set of equations ((A.7 - A.10)) are presented. Results are discussed first, for the case in which the model dissipation is high and second, for almost inviscid dynamics but with the dissipation not effectively zero ($r \neq 0$).

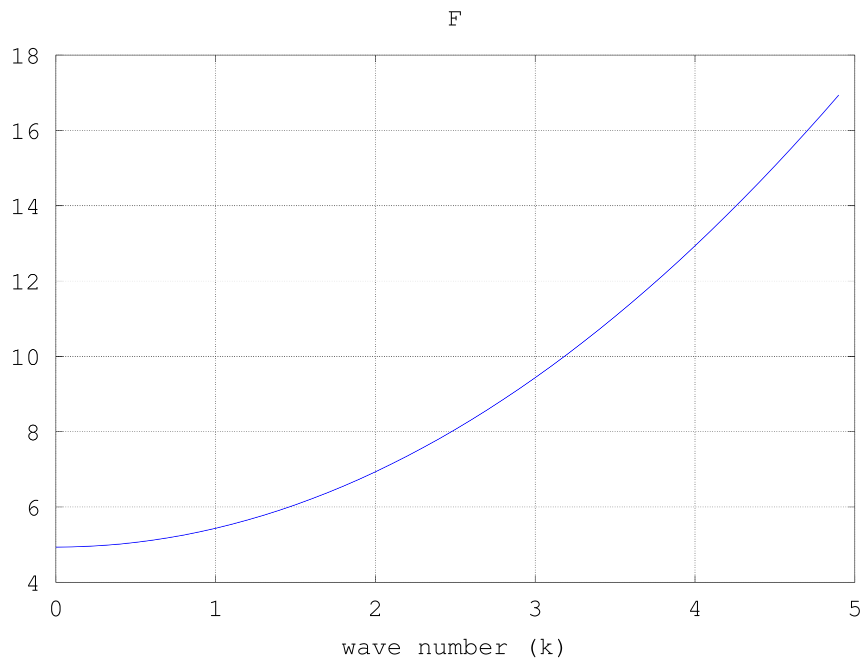

Figure A.2: Critical dependence of the Froude number F as a function of the zonal wavenumber k.

A.3.1 The case $r = \mathcal{O}(1)$

The model set up is such that the system is slightly above its neutral criticality. The barotropic velocity in the channel is set at $\mathrm{U}_B = 13.125$ and the most unstable mode with this barotropic velocity is found to be $k = 4.34$. The parameter values of the model when neutrally critical and those used in the nonlinear numerical simulations are given in table A.1.

Table A.1: Model parameters used for the case $r = O(1)$

Parameter	Symbol	Critical values	Simulation value
Shear	U_s	3.00	3.25
Froude number	F	40.0	40.0
Dissipation	r	4.60	4.60

Discussion

At first order, the solution has both $\sin \pi y$ barotropic and baroclinic modes as the leading terms of the solution to the nonlinear set of equations (A.7, A.8, A.9 and A.10). The leading terms of the solution exhibit the oscillations of the initial perturbation imposed at the entrance of the channel (see figures A.3 and A.5) up to downstream. The amplitude of the perturbation grows initially with increasing distance downstream until it reaches a finite amplitude and thereafter momentarily stabilises

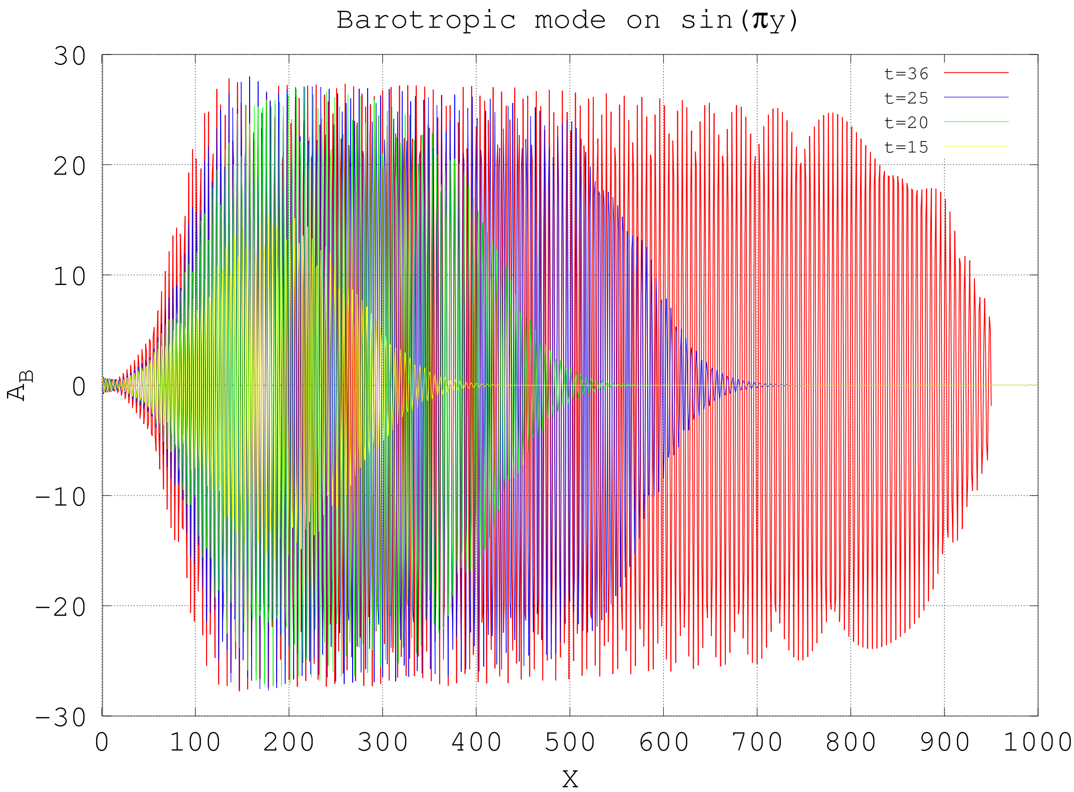

Figure A.3: Snapshots of the $\sin \pi y$ mode of the barotropic potential vorticity with $\mathrm{U}_s = \mathrm{U}_{so} + 0.25$ and $r = r_o$.

before eventually decaying to zero. The stabilisation in growth of the perturbation at finite amplitude is longer downstream.

In all cases and for all the modes considered, it is observed that the part of the growing perturbation behind the front reaches finite amplitude before saturation such that, in the regions ahead of the front, the amplitude of the perturbation remains constant in the vicinity of the front and decays quite quickly away from the front downstream. The slightly unique cases amongst the modes considered in this study are the $\sin 2\pi y$ baroclinic and barotropic modes which exhibit fewer oscillations compared to the leading order terms (see Fig. A.4 and Fig. A.6). With the exception of a few oscillations whose amplitudes are still small near the channel entrance, any information about the oscillatory nature of the perturbation is lost downstream and the resulting correction to the leading order terms, is at large non-oscillating.

Behind the front, oscillations are observed in the spatial and temporal structure of the perturbation before finally reaching finite amplitude in the vicinity of the front (Fig. A.6). Ahead of the front, the perturbation has already reached finite amplitude and therefore remains constant (for longer time scales) or immediately decays (for shorter time scales) ahead of the front. This is in agreement with the results found by Pedlosky (2011) who highlighted that the correction to the mean flow carries the oscillatory information of the perturbation only behind the front during which time

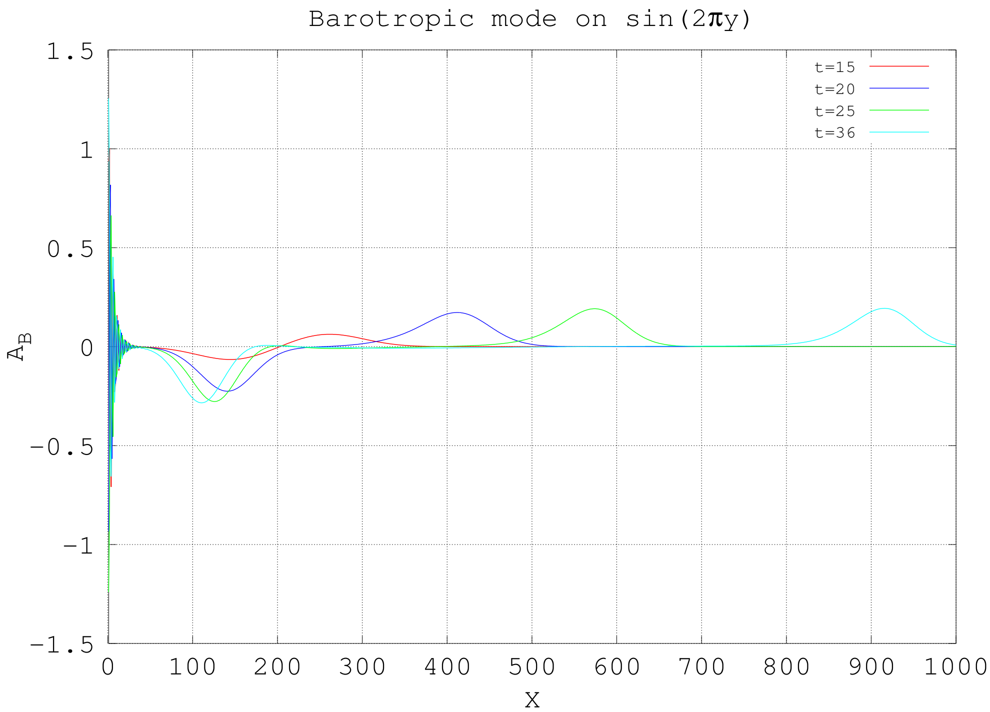

Figure A.4: Snapshots of the baroclinic potential vorticity on the $\sin(2\pi \mathrm{y})$ mode with $\mathrm{U}_s = \mathrm{U}_{so} + 0.25 \quad \text{and} \quad r = r_o$

the perturbation also attains finite amplitude. In that study, it was also noticed that ahead of the front, the structure of the correction term is smooth, with the perturbation having reached finite amplitude.

We also notice that the baroclinic mode is the largest of the $\sin 2\pi y$ modes which is consistent with the results obtained by Pedlosky (2011), who showed analytically that the first order correction to the mean flow is fully baroclinic. However, the non-linear simulations conducted in this study reveal that there is a small contribution to the mean flow correction by the $\sin 2\pi y$ barotropic mode (Fig. A.4). This component is the smallest of all the modes but it is worth noting that although the asymptotic approach adopted using the finite amplitude model in Pedlosky (2011) fails to capture this contribution, it is not necessarily zero as observed in figure A.4.

A probable explanation why the asymptotic approach shows that the $\sin(2\pi y)$ barotropic mode does not contribute to the mean flow correction could be that as observed from figure (A.4), the spatial average of this mode is zero. So, the reason for the failure to capture this mode in the theory is not because it is small in magnitude but it is because it vanishes on the average. More interestingly, apart from the initial transients, the $\sin 2\pi y$ barotropic mode manifests as a periodic oscillation with vanishing spatial average.

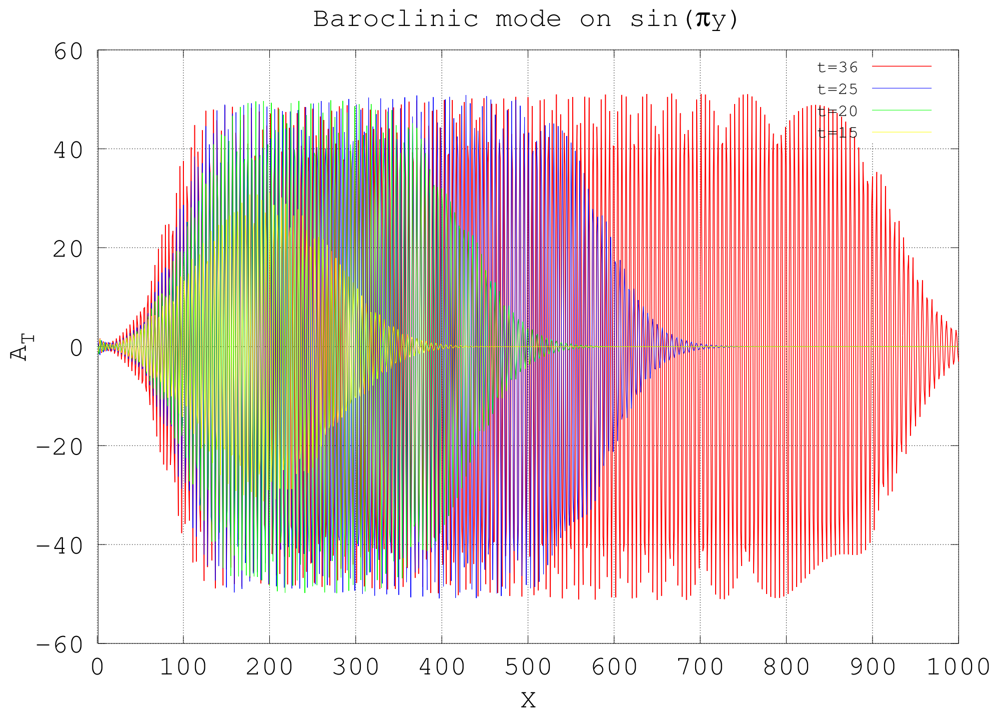

Figure A.5: Snapshots of the $\sin \pi y$ baroclinic potential vorticity mode with $\mathrm{U}_s = \mathrm{U}_{so} + 0.25$ and $r = r_o$

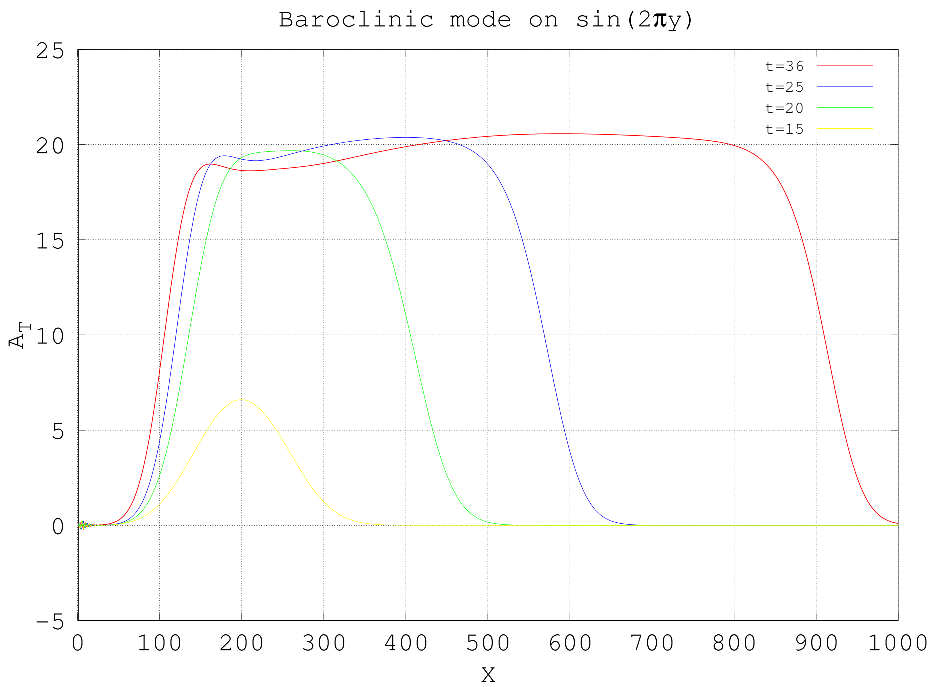

Figure A.6: Snapshots of the baroclinic potential vorticity on the $\sin(2\pi \mathrm{y})$ mode with $\mathrm{U}_s = \mathrm{U}_{so} + 0.25$ and $r = r_o$

Table A.2: Model parameters used for the case $r = O(\Delta)$

Parameter	Symbol	Critical values	Simulation value
Shear	U_s	1.30	1.30
Froude number	F	4.9348	4.9348 + 0.02
Dissipation	r	0.001	0.001

A.3.2 The case $r = \mathcal{O}(\Delta)$

The barotropic flow in this case is reduced to $U_B = 1.65$ and the most unstable mode corresponds to the wave number $k = 0.15$. Several simulations are performed at various degrees of super criticality (i.e for increasing values of Δ). Results are presented in figures A.7, A.8 and A.9. For most values of Δ, the flow does not seem to change significantly but it happens that as Δ increases, more features emerge ahead of the front for longer integration times. At leading order, the baroclinic mode is largest while the corresponding barotropic mode is small but nonzero (Fig. A.7) and all the modes are noticed to exhibit oscillations downstream. Also as theory predicts, the largest component of the correction to the leading order solution is baroclinic (the $\sin 2\pi y$ baroclinic mode). However, the fully non-linear solution shows that a barotropic contribution is also present. The latter is initially small (≈ 0) but develops with time until it is one order of magnitude lower than the $\sin 2\pi y$ baroclinic mode.

Discussion

At the leading order, the dominant part of the flow is the $\sin\pi y$ baroclinic mode. The $\sin 2\pi y$ baroclinic mode is lower than the former but it is significantly large. This is in agreement with the findings of Pedlosky (2011) which showed that in this regime, the leading order solution is the $\sin\pi y$ baroclinic mode and that its barotropic correspondent although an order of magnitude lower, is the second most important component. Although not as much as an order of magnitude, the fully nonlinear solutions strongly yield similar results.

At the next order, the major correction component to the mean flow is found to be largely baroclinic (i.e the $\sin 2\pi y$ baroclinic mode). The $\sin 2\pi y$ barotropic mode is at large zero for short timescales during the simulation. The amplitudes of this barotropic mode are noticed to grow with increasing distance from the channel entrace but with oscillations of low frequency compared to all the other components. This is also in agreement with the findings from the multi-scale asymptotics which yielded that the correction to the mean flow is baroclinic for all time scales (Pedlosky, 2011). However, our findings here show that there is a small barotropic contribution to the mean flow as the downstream distance increases.

Increasing the degree of super criticality leads to a complete break down of the predictions of the linear and weakly non-linear theory. In this case, at leading order, the dominant term is the $\sin\pi y$ baroclinic mode as opposed to the $\sin\pi y$ barotropic mode predicted by theory. Also, at the next order, the barotropic correction to the mean flow becomes appreciable which is of course another difference from the case considered when the dynamics are slightly super critical. The other remarkable

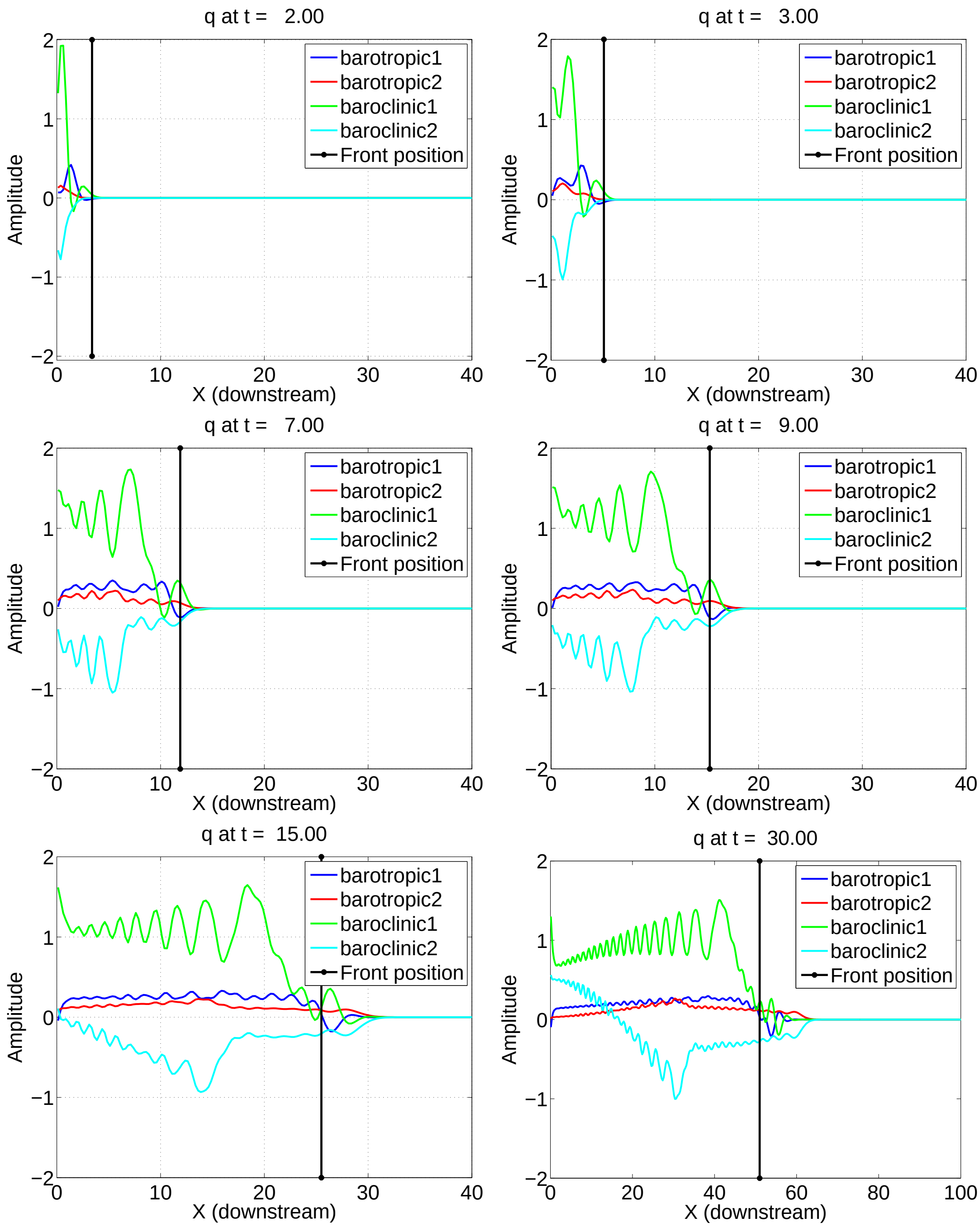

Figure A.7: Snapshots of the barotropic and baroclinic potential vorticities for $\Delta = 0.02$.

feature that emerges with increasing levels of supercriticalities is that the features formed ahead of the front become more apparent and highly variable downstream as one would expect when the non-linearities in the system are at full operation.

In conclusion, the findings from this study qualitatively show that the degree of dissipation in the system is a major determinant of the dynamics of the flow. When the system is substantively dissipative, the marginal curve is given in terms of the

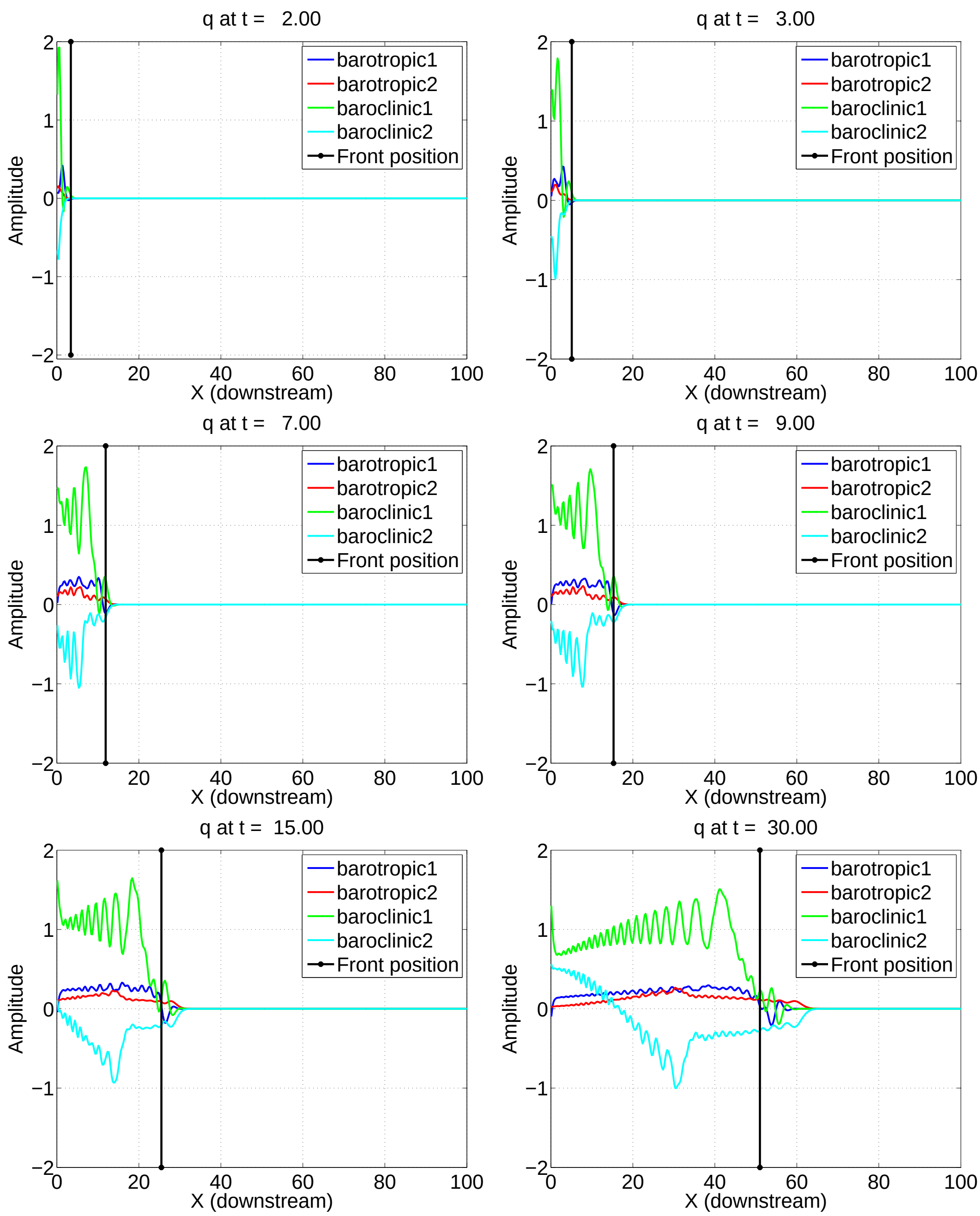

Figure A.8: Snapshots of the barotropic and baroclinic potential vorticities for $\Delta = 0.1$.

shear and the dominant correction component to the mean flow is largely baroclinic. In the case when the dissipation is so small, the marginal curve is expressed in terms of the parameter, F - the Froude number. Here, the lowest order component is found to be barotropic and the correction is fully baroclinic.

For further study, it would be meaningful to consider using a periodic channel so that the flow statistics can be obtained with a good degree of accuracy to enable giving a quantitative account of the dynamics of the flow and how the different

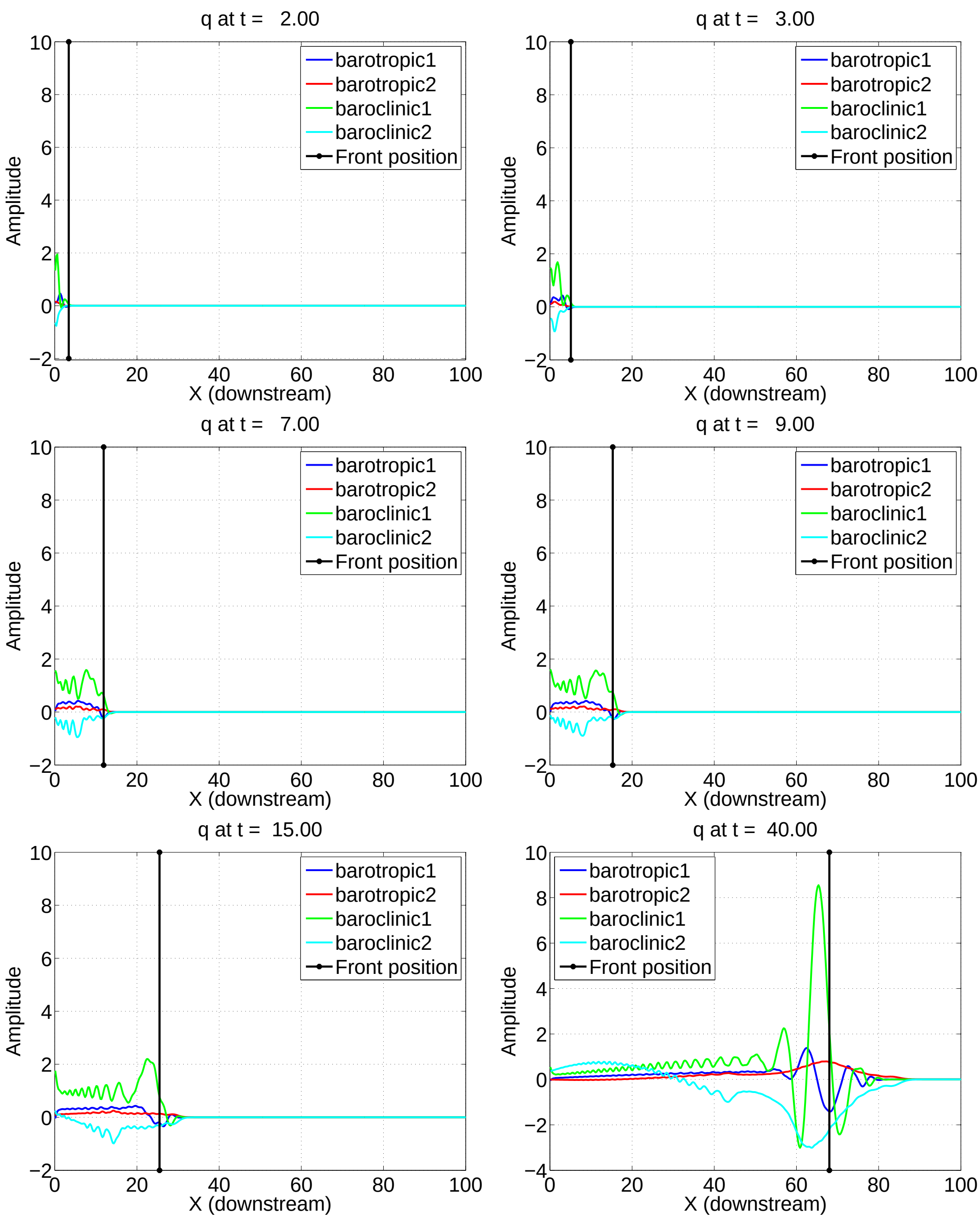

Figure A.9: Snapshots of the barotropic and baroclinic potential vorticities for $\Delta = 0.7$.

components exchange the energy in both spatial and temporal considerations. Of course, inclusion of the $\beta-$ effect would also serve the purpose of getting the results obtained into comparison of what happens when scales larger than the deformation radius are considered.

Bibliography

Abraham, E. R., and M. M. Bowen, 2002: Chaotic stirring by a mesoscale surface-ocean flow. *Chaos*, **12**, 373–381.

Aref, H., 1984: Stirring by Chaotic Advection. *J. Fluid Mech.*, **143**, 1 – 21.

Aref, H., 2002: The development of chaotic advection. *Phys. Fluids*, **14**, 1315 – 1325.

Arnold, V. I., 1973: *Ordinary Differential Equations*. Cambridge, MA: MIT Press.

Artale, V., G. Boffetta, A. Celani, M. Cencini, and A. Vulpiani, 1997: Dispersion of passive tracers in closed basins: Beyond the diffusion coefficient. *Phys. Fluids*, **9**, 3163–3171.

Aurell, E., G. Boffetta, A. Crisanti, G. Paladin, and A. Vulpiani, 1997: Predictability in the large: an extension of the concept of Lyapunov exponent. *J. Phys. A: Math. Gen.*, **30**, 1–26.

Badin, G., 2013: Surface semi-geostrophic dynamics in the ocean. *Geophys. Astrophys. Fluid Dyn.*, **107**, 526–540.

Badin, G., 2014: On the role of non-uniform stratification and short-wave instabilities in three-layer quasi-geostrophic turbulence. *Phys. Fluids*, **26**, 096 603.

Badin, G., A. Tandon, and A. Mahadevan, 2011: Lateral Mixing in the Pycnocline by Baroclinic Mixed Layer Eddies. *J. Phys. Oceanogr.*, **41**, 2080 – 2101.

Badin, G., R. G. Williams, J. T. Holt, and L. J. Fernand, 2009: Are mesoscale eddies in shelf seas formed by baroclinic instability of tidal fronts? *J. Geophys. Res.*, **114**, C10 021.

Badin, G., R. G. Williams, Z. Jing, and L. Wu, 2013: Water-mass transformations in the Southern Ocean diagnosed from observations: contrasting effects of air-sea fluxes and diapycnal mixing. *J. Phys. Oceanogr.*, **43**, 1472–1484.

Badin, G., R. G. Williams, and J. Sharples, 2010: Water-mass transformation in the shelf seas. *J. Mar. Res.*, **68**, 189 – 214.

Bennett, A. F., 1984: Relative dispersion: Local and nonlocal dynamics. *J. Atmos. Sci.*, **41**, 1881 – 1886.

Beron-Vera, F. J., 2015: Flow Coherence: Distinguishing Cause from Effect. *Selected Topics of Computational and Experimental Fluid Mechanics*, J. K. et al., Ed., Springer International Publishing Switzerland.

Beron-Vera, F. J., and M. J. Olascoaga, 2009: An Assessment of the Importance of Chaotic Stirring and Turbulent Mixing on the West Florida Shelf. *J. Phys. Oceanogr.*, **39**, 1743–1755.

Beron-Vera, F. J., M. J. Olascoaga, M. G. Brown, H. Koçak, and I. I. Rypina, 2010: Invariant-tori-like Lagrangian coherent structures in geophysical flows. *Chaos*, **20**, 017 514.

Beron-Vera, F. J., M. J. Olascoaga, and G. J. Goni, 2008: Oceanic mesoscale eddies as revealed by Lagrangian coherent structures. *Geophys. Res. Lett.*, **35**, L12 603.

Beron-Vera, F. J., Y. Wang, M. J. Olascoaga, J. G. Goni, and G. Haller, 2013: Objective detection of oceanic eddies and the Agulhas leakage. *J. Phys. Oceanogr.*, **43**, 1426 – 1438.

Bettencourt, J. H., C. Lopez, and E. Hernandez-Garcia, 2012: Oceanic three-dimensional Lagrangian coherent structures: A study of a mesoscale eddy in the Benguela upwelling region. *Ocean Modell.*, **51**, 73 – 83.

Bettencourt, J. H., C. López, and E. Hernández-García, 2013: Characterization of coherent structures in three-dimensional turbulent flows using finite-size Lyapunov exponents. *J. Phys. A: Math. Theor*, **46 (254022)**.

Blazevski, D., and G. Haller, 2014: Hyperbolic and elliptic transport barriers in three dimensional unsteady flows. *Physica D*, **273**, 46 – 62.

Boccaletti, G., R. Ferrari, and B. Fox-Kemper, 2007: Mixed Layer Instabilities and Restratification. *J. Phys. Oceanogr.*, **37**, 2228 – 2250.

Boffetta, G., A. Celani, M. Cencini, G. Lacorata, and A. Vulpiani, 2000: Nonasymptotic properties of transport and mixing. *Chaos*, **1**, 50–60.

Boffetta, G., G. Lacorata, G. Redaelli, and A. Vulpiani, 2001: Detecting barriers to transport: a review of different techniques. *Physica D*, **159**, 58–70.

Boyd, J., 1992: The energy spectrum of fronts: time evolution and shocks in Burgers' equation. *J. Atmos. Sci.*, **49**, 128–139.

Boyer, T., S. Levitus, H. Garcia, R. A. Rocarnini, C. Stephens, and J. Antonov, 2005: Objective analyses of annual, seasonal, and monthly temperature and salinity for the world ocean on a 0.25° grid. *Int. J. Climatol.*, **(25)7**, 931 – 945.

Brunton, S. L., and C. W. Rowley, 2010: Fast computation of finite-time Lyapunov exponent fields for unsteady flows. *Chaos*, **20 (017503)**.

Calil, P. H., and K. J. Richards, 2010: Transient upwelling hot spots in the oligotrophic North Pacific. *J. Geophys. Res.*, **115**, C02 003.

Callies, J., and R. Ferrari, 2013: Interpreting Energy and Tracer Spectra of Upper-Ocean Turbulence in the Submesoscale Range (1-200 km). *J. Phys. Oceanogr.*, **43**, 2456 – 2474.

Callies, J., R. Ferrari, J. M. Klimak, and J. Gula, 2015: Seasonality in submesoscale turbulence. *Nature Communications*, **6**, 6862.

Capet, X., J. C. McWilliams, M. J. Molemaker, and A. F. Shchepetkin, 2008: Mesoscale to Submesoscale Transition in the California Current System. Part I: Flow Structure, Eddy Flux and Observational Tests. *J. Phys. Oceanogr.*, **38**, 29 – 43.

Cencini, M., and A. Vulpiani, 2013: Finite size Lyapunov exponent: review on applications. *J. Phys. A*, **46**, 254 019.

Charney, J., 1971: Geostrophic Turbulence. *J. Atmos. Sci.*, **28**, 1087 – 1095.

Cole, S. T., and D. L. Rudnick, 2012: The spatial distribution and annual cycle of upper-ocean thermohaline structure. *J. Geophys. Res.*, **117 (C02027)**, doi: 10.1029/2011JC007033.

Cole, S. T., D. L. Rudnick, and J. Colosi, 2010: Seasonal evolution of upper ocean horizontal structure and the remnant mixed layer. *J. Geophys. Res.*, **115 (C04012)**, doi:10.1029/2009JC005654.

Costa, M., A. Goldberger, and C. Peng, 2005: Multiscale entropy analysis of biological signals. *Phys. Rev.*, **71**, 021 906.

Dee, D. P., and Coauthors, 2011: The ERA-Interim reanalysis: configuration and performance of the data assimilation system. *Q. J. R. Meteorol. Soc.*, **137**, 553 – 597.

Dombre, T., U. Frisch, J. M. Greene, M. Henon, A. Mehr, and A. M. Soward, 1986: Chaotic streamlines in the ABC flows. *J. Fluid Mech.*, **167**, 353 – 391.

d'Ovidio, F., V. Fernández, E. Hernandez-Garcia, and C. Lopez, 2004: Mixing structures in the Mediterranean Sea from finite-size Lyapunov exponents. *Geophys. Res. Lett.*, **31**, L17 203.

d'Ovidio, F., J. Isern-Fontanet, C. Lopez, E. Hernandez-Garcia, and E. Garcia-Ladon, 2009: Comparison between Eulerian diagnostics and finite-size Lyapunov exponents computed from altimetry in the Algerian basin. *Deep-Sea Res. I*, **56**, 15 – 31.

d'Ovidio, F., S. D. Monte, S. Alvain, Y. Dandonneau, and M. Lévy, 2010: Fluid dynamical niches of phytoplankton types. *PNAS*, **107**, 18 366 – 18 370.

Farazmand, M., D. Blazevski, and G. Haller, 2014: Shearless transport barriers in unsteady two-dimensional flows and maps. *Physica D*, **278-279**, 44 – 57.

Farazmand, M., and G. Haller, 2012: Computing Lagrangian Coherent Structures from their variational theory. *Chaos*, **22 (013128)**.

Farazmand, M., and G. Haller, 2013: Attracting and repelling Lagrangian coherent structures from a single computation. *Chaos*, **23(2) (023101)**.

Farnetani, C. G., and H. Samuel, 2003: Lagrangian structures and stirring in the Earth's mantle. *Earth. Planetary Sci. Lett.*, **206**, 335–348.

Ferrari, R., and D. L. Rudnick, 2000: Thermohaline variability in the upper ocean. *J. Geophys. Res.*, **105**, 16 857 – 16 883.

Fofonoff, N., 1981: The Gulf Stream Stream System. Massachusetts Institute of Technology Press, Cambridge, MA.

Fox-Kemper, B., and R. Ferrari, 2008: Parameterization of Mixed Layer Eddies. Part II: Prognosis and Impact. *J. Phys. Oceanogr.*, **38**, 1166 – 1179.

Fox-Kemper, B., R. Ferrari, and R. Hallberg, 2008: Parameterization of Mixed Layer Eddies. Part I: Theory and Diagnosis. *J. Phys. Oceanogr.*, **38**, 1145 – 1165.

Fuchs, R., B. Schindler, and R. Peikert, 2012: Scale-space approaches to ftle ridges. *Topological Methods in Data Analysis and Visualization II*, R. Peikert, H. Hauser, H. Carr, and R. Fuchs, Eds., Springer, New York, 283 – 296.

Garaboa-Paz, D., J. Eiras-Barca, F. Huhn, and V. Pérez-Muñuzuri, 2015: Lagrangian coherent structures along atmospheric rivers. *Chaos*, **25**, 063 105.

Garcia-Olivares, A., J. Isern-Fontanet, and E. Garcia-Ladon, 2007: Dispersion of passive tracers and finite-scale Lyapunov exponents in the Western Mediterranean Sea. *Deep-Sea Res. I*, **54**, 253–268.

Gaspard, P., and X. Wang, 1993: Noise, chaos, and $(\epsilon - \tau)$ entropy per unit time. *Phys. Rep.*, **235**, 291–343.

Griffa, A., A. C. Haza, T. M. Özgökmen, A. Molcard, V. Taillandier, K. Schroeder, Y. Chang, and P. Poulain, 2013: Investigating transport pathways in the ocean. *Deep Sea Res. II*, **85**, 81–95.

Gula, J., M. J. Molemaker, and J. C. McWilliams, 2014: Submesoscale Cold Filaments in the Gulf Stream. *J. Phys. Oceanogr.*, **44**, 2617 – 2643.

Gula, J., M. J. Molemaker, and J. C. McWilliams, 2016: Submesoscale Dynamics of a Gulf Stream Frontal Eddy in the South Atlantic Bight. *J. Phys. Oceanogr.*, **46**, 305 – 325, doi:10.1175/JPO-D-14-0258.1.

Haine, T. W. N., and J. Marshall, 1998: Gravitational, Symmetric and Baroclinic Instability of the Ocean Mixed Layer. *J. Phys. Oceanogr.*, **28**, 634 – 658.

Haller, G., 2000: Finding finite-time invariant manifolds in two-dimensional velocity fields. *Chaos*, **10**, 99–108.

Haller, G., 2001: Distinguished material surfaces and coherent structures in three-dimensional fluid flows. *Physica D*, **149**, 248–277.

Haller, G., 2002: Lagrangian coherent structures from approximate velocity data. *Phys. Fluids.*, **14**, 1851–1861.

Haller, G., 2005: An objective definition of a vortex. *J. Fluid Mech.*, **525**, 1 – 26.

Haller, G., 2011: A variational theory of hyperbolic Lagrangian Coherent Structures. *Physica D*, **240**, 574 – 598.

Haller, G., 2015: Lagrangian Coherent Structures. *Ann. Rev. Fluid Mech.*, **47**, 137 – 162.

Haller, G., and F. J. Beron-Vera, 2012: Geodesic theory of transport barriers in two dimensional flows. *Physica D*, **241**, 1680 – 1702.

Haller, G., and F. J. Beron-Vera, 2013: Coherent Lagrangian vortices: the black holes of turbulence. *J. Fluid Mech.*, **731**, R4:1–10, doi:10.1017/jfm.2013.391.

Haller, G., and T. Sapsis, 2011: Lagrangian coherent structures and the smallest finite-time Lyapunov exponent. *Chaos*, **21 (023115)**.

Haller, G., and G. Yuan, 2000: Lagrangian coherent structures and mixing in two-dimensional turbulence. *Physica D*, **147**, 352–370.

Harle, M., and U. Feudel, 2007: Hierachy of islands in conservative systems yields multimodal distributions of FTLEs. *Chaos Solitons Fractals*, **31**, 130 – 137.

Harrison, C. S., and G. A. Glatzmaier, 2012: Lagrangian Coherent Structures in the California Current System - Sensitivies and Limitations. *Geophys. Astrophys. Fluid. Dyn.*, **106**, 22–24.

Haynes, P., and J. Anglade, 1997: The Vertical-Scale Cascade in Atmospheric Tracers due to Large-Scale Differential Advection. *J. Atmos. Sci.*, **54**, 1121 – 1136.

Haynes, P. H., 2001: Vertical shear plus horizontal stretching as a route to mixing. *Proceedings. 12th Hawaii Winter Workshop (16 - 19 January)*, University of Hawaii at Manoa.

Hernández-Carrasco, I., C. López, E. Hernandez-Garcia, and A. Turiel, 2011: How reliable are finite size Lyapunov exponents for the assessment of ocean dynamics ? *Ocean Modell.*, **36**, 208 – 218.

Hernández-Carrasco, I., C. López, E. Hernández-García, and A. Turiel, 2012: Seasonal and regional characterization of horizontal stirring in the global ocean. *J. Geophys. Res.*, **117 (C10007)**, doi:10.1029/2012JC008222.

Hoskins, B., I. Draghici, and H. Davies, 1978: A new look at the ω-equation. *Q. J. R. Meteorol. Soc.*, **104**, 31 – 38.

Joseph, B., and B. Legras, 2002: Relation Between Kinematic Boundaries, Strring and Barriers for the Antarctic polar Vortex. *J. Atmos. Sci.*, **59**, 1198 – 1212.

Karrasch, D., and G. Haller, 2013: Do Finite-Size Lyapunov Exponents detect coherent structures? *Chaos*, **23**, 043 126 – 043 126.

Klymak, J. M., W. Crawford, M. H. Alford, J. A. MacKinnon, and R. Pinkel, 2015: Along-isopycnal variability of spice in the North Pacific. *J. Geophys. Res. Oceans.*, **120**, 2287 – 2307.

Kunze, E., J. M. Klymak, R. C. Lien, R. Ferrari, C. M. Lee, M. A. Sundermeyer, and L. Goodman, 2015: Submesoscale Water-Mass Spectra in the Sargasso Sea. *J. Phys. Oceanogr.*, **45**, 1325 – 1338.

Lapeyre, G., 2002: Characterization of finite-time Lyapunov exponents and vectors in two-dimensional turbulence. *Chaos*, **12**, 688 – 698.

Lapeyre, G., P. Klein, and B. L. Hua, 2006: Oceanic restratification forced by surface frontogenesis. *J. Phys. Oceanogr.*, **36**, 1577 – 1590.

Large, W., J. McWilliams, and S. Doney, 1994: A review and a model with nonlocal boundary layer parameterization. *Rev. Geophys*, **32**, 363 – 403.

Lee, C., E. A. DÁsaro, and R. Harcourt, 2006: Mixed layer restratification: Early results from the AESOP program. *EOS Trans. AGU*, **87 (52)**.

Lekien, F., and J. Marsden, 2005: Tricubic interpolation in three dimensions. *Int. J. Numer. Meth. Engng.*, **63**, 455 – 471.

Lekien, F., S. C. Shadden, and J. E. Marsden, 2007: Lagrangian coherent structures in n-dimensional systems. *J. Math. Phys.*, **48**, 065 404.

Leung, S., 2011: An Eulerian approach for computing the finite time Lyapunov exponent. *J. Computation Phys.*, **230**, 3500 – 3524.

Lévy, M., P. Klein, and A. Treguier, 2001: Impacts of Submesoscale Physics on Production and Subduction of Phytoplankton in an Oligotrophic Regime. *J. Mar. Res.*, **59**, 535 – 565.

Luyten, J., 1977: Scales of motion in the deep Gulf Stream and across the continental rise. *J. Mar. Res.*, **35**, 49 – 74.

Mahadevan, A., 2006: Modelling vertical motion at ocean fronts: Are nonhydrostatic effects relevant at submesoscales? *Ocean Modell.*, **14**, 222 –240.

Mahadevan, A., and A. Tandon, 2006: An analysis of mechanisms for submesoscale vertical motion at ocean fronts. *Ocean Modell.*, **14**, 241 – 256.

Mahadevan, A., A. Tandon, and R. Ferrari, 2010: Rapid changes in mixed layer stratification driven by submesoscale instabilities and winds. *J. Geophys. Res.*, **115**, C03 017.

Marshall, J., L. P. A. Adcroft, C. Hill, and C. Heisey, 1997a: A finite-volume, incompressible Navier Stokes model for studies of the ocean on parallel computers. *J. Geophys. Res.*, **102**, 5753 – 5766.

Marshall, J., C. N. Hill, L. Perelman, and A. Adcroft, 1997b: Hydrostatic, quasi - hydrostatic and non - hydrostatic ocean modelling. *J. Geophys. Res.*, **102**, 5753 – 5752.

Mathur, M., G. Haller, T. Peacock, J. E. Rupert-Felsot, and H. L. Swinney, 2007: Uncovering the Lagrangian Skeleton of Turbulence. *Phys. Rev. Lett.*, **98**, 144 502.

Mensa, J., A. Griffa, Z. Garraffo, T. M. Özgökmen, A. C. Haza, and M. Veneziani, 2013: Seasonality of the submesoscale dynamics in the Gulf Stream region. *Ocean Dyn.*, **63**, 923–941.

Molemaker, M. J., and J. C. McWilliams, 2005: Baroclinic Instability and Loss of Balance. *J. Phys. Oceanogr.*, **35**, 1505 – 1517.

Mukiibi, D., 2014: A numerical study of the downstream development of a baroclinic instablity. *2014 GFD program*, Woods Hole Oceanographic Institution, Massachusetts,USA., Vol. Climate Physics and Dynamics, URL http://www.whoi.edu/fileserver.do?id=217704&pt=2&p=224229.

Mukiibi, D., G. Badin, and N. Serra, 2016a: The seasonality of submesoscale turbulence deduced from finite time Lyapunov exponents. In preparation.

Mukiibi, D., G. Badin, and N. Serra, 2016b: Three dimensional chaotic advection by mixed layer baroclinic instabilities. *J. Phys. Oceanogr.*, **46**, 1509 – 1529, doi: 10.1175/JPO-D-15-0121.1.

Norgard, G., and P. Bremer, 2012: Second derivative ridges are straight lines and the implications for computing Lagrangian Coherent Structures. *Physica D*, **241**, 1475 – 1476.

Okubo, A., 1970: Horizontal dispersion of floatable trajectories in the vicinity of velocity singularities such as convergences. *Deep-Sea Res.*, **17**, 445 – 454.

Olascoaga, M. J., and G. Haller, 2012: Forecasting sudden changes in environmental pollution patterns. *PNAS*, **109**, 4738 – 4743, doi:10.1073/pnas.1118574109.

Olascoaga, M. J., I. I. Rypina, M. G. Brown, F. J. Beron-Vera, H. Kocak, L. E. Brand, G. R. Halliwell, and L. K. Shay, 2006: Persistent transport barrier on the West Florida Shelf. *Geophys. Res. Lett.*, **33 (L22603)**, doi:10.1029/2006GL027800.

Onu, K., F. Huhn, and G. Haller, 2015: LCS Tool: A computational platform for Lagrangian Coherent Structures. *J. Comput. Sci.*, **7**, 26 – 36.

Ottino, J. M., 1989: *The Kinematics of Mixing: Stretching, chaos, and transport.* 1st ed., No. pp.364, ISBN 0521363357, Cambridge University Press, New York.

Ottino, J. M., 1990a: Mixing, Chaotic Advection and Turbulence. *Ann. Rev. Fluid Mech.*, **22**, 207 – 254.

Ottino, J. M., 1990b: Mixing, Chaotic Advection and Turbulence. *Ann. Rev. Fluid Mech.*, **22**, 207 – 254.

Ouellette, N. T., 2012: On the dynamical role of coherent structures in turbulence. *C. R. Phys.*, **13**, 866 – 877.

Özgökmen, T. M., A. C. Poje, P. Fischer, H. Childs, H. Krishnan, C. Garth, A. C. Haza, and E. Ryan, 2012: On multi-scale dispersion under the influence of surface mixed layer instabilities and deep flows. *Ocean Modelling*, **56**, 16–30.

Peacock, T., G. Froyland, and G. Haller, 2015: Introduction to Focus Issue: Objective Detection of Coherent Structures. *Chaos*, **25 (087201)**.

Peacock, T., and G. Haller, 2013: Lagrangian coherent structures: The hidden skeleton of fluid flows. *Physics Today*, **66**, 41 – 47.

Pedlosky, J., 1970: Finite-amplitude baroclinic waves. *Journal of Atmospheric Sciences*, **27**, 15–30.

Pedlosky, J., 2011: The nonlinear downstream development of baroclinic instability. *Journal of Marine Research*, **69**, 705–722.

Peikert, R., D. Günther, and T. Weinkauf, 2013: Comment on "Second derivative ridges are straight lines and the implications for computing Lagrangian Coherent Structures, Physica D 2012.05.006". *Physica D*, **242**, 65 – 66.

Peikert, R., A. Pobitzer, F. Sadlo, and B. Schindler, 2014: A Comparison of Finite-Time and Finite-Size Lyapunov Exponents. *Topological Methods in Data Analysis and Visualization III*, P.-T. Bremer, I. Hotz, V. Pascucci, and R. Peikert, Eds., Springer, 187–200.

Petersen, M. R., K. Julien, and J. B. weiss, 2006: Vortex cores, strain cells, and filaments in quasigeostrophic turbulence. *Phys. Fluids*, **18 (026601)**.

Pokorny, P., 2012: Geodesics Revisted. Chaotic Modelling and Simulation, 281–298.

Prants, S. V., 2014: Chaotic Lagrangian transport and mixing in the ocean. *The European Physical Journal Special Topics*, **223**, 2723 – 2743.

Pratt, L. J., I. I. Rypina, T. M. Özgökmen, P. Wang, H. Childs, and Y. Bebieva, 2013: Chaotic advection in a steady, three-dimensional, Ekman-driven eddy. *J. Fluid Mech.*, **738**, 143 – 183.

Pratt, L. J., I. I. Rypina, T. M. Özgökmen, P. Wang, H. Childs, and Y. Bebieva, 2014: Chaotic advection in a steady, three-dimensional, Ekman-driven eddy. *J. Fluid Mech.*, **738**, 143 – 183.

Price, J. F., 1981: Upper ocean response to a hurricane. *J. Phys. Oceanogr.*, **11**, 153 – 175.

Provenzale, A., 1999: Transport by coherent barotropic vortices. *Ann Rev. Fluid Mech.*, **31**, 55 – 93.

Qiu, B., and K. A. Kelly, 1993: Upper ocean heat balance in the Kuroshio Extension region. *J. Phys. Oceanogr.*, **23**, 2027 – 2041.

Ragone, F., and G. Badin, 2016: Surface semi-geostrophic turbulence: freely-evolving dynamics. *J. Fluid Mech.*, **792**, 740 – 774.

Richardson, L. F., 1926: Atmospheric diffusion shown on a distance-neighbour graph. *Proc. R. Soc. London A*, **110**, 709–737.

Rutherford, B., G. Dangelmayr, J. Persing, W. H. Schubert, and M. T. Montgomery, 2010: Advective mixing in a nondivergent barotropic hurricane model. *Atmos. Chem. Phys.*, **10**, 475 – 497.

Rypina, I. I., M. G. Brown, F. J. Beron-Vera, H. Koçak, M. J. Olascoaga, and I. A. Udovydchenkov, 2007: On the Lagrangian Dynamics of Atmospheric Zonal Jets and the Permeability of the Stratospheric Polar Vortex. *J. Atmos. Sci.*, **64**, 3595 – 3610.

Rypina, I. I., and L. J. Pratt, 2010: Chaotic Advection in an Archipelago. *J. Phys. Oceanogr.*, **40**, 1988 – 2006.

Rypina, I. I., L. J. Pratt, P. Wang, T. Özgökmen, and I. Mezic, 2015: Resonance phenomena in a time-dependent, three-dimensional model of an idealized eddy. *CHAOS*, **25**, 087 401.

Sadlo, F., and R. Peikert, 2007: Efficient visualization of Lagrangian coherent structures by filtered AMR ridge extraction. *IEEE Trans. Vis. Comput. Graph*, **13**, 1456 – 1463.

Sasaki, H., P. Klein, B. Qiu, and Y. Sasai, 2014: Impact of oceanic-scale interactions on the seasonal modulation of ocean dynamics by the atmosphere. *Nature Communications*, **5 (5636)**, doi:10.1038/ncomms6636.

Schindler, B., R. Peikert, R. Fuchs, and H. Theisel, 2012: Ridge concepts for the visualization of Lagrangian coherent structures. *Topological Methods in Data Analysis and Visualization II*, R. Peikert, H. Hauser, H. Carr, and R. Fuchs, Eds., Berlin: Springer, 221 – 236.

Schroeder, K., A. C. Haza, A. Griffa, T. M. Özgökmen, P. M. Poulain, R. Gerin, G. Peggion, and M. Rixen, 2011: Relative dispersion in the Liguro-Provencal basin: from sub-mesoscale to mesoscale. *Deep-Sea Res. I*, **58**, 209–228.

Schroeder, K., and Coauthors, 2012: Targeted Lagrangian sampling of submesoscale dispersion at a coastal frontal zone. *Geophys. Res. Lett.*, **39**, L11 608.

Schultz, T., H. Theisel, and H. P. seidel, 2010: Crease Surfaces: From Theory to Extraction and Application to Diffusion Tensor MRI. *IEEE Trans. Vis. Comput. Graph*, **16**, 109 – 119.

Sena-Martins, M., N. Serra, and D. Stammer, 2015: Spatial and temporal scales of sea surface salinity variability in the Atlantic Ocean. *J. Geophys. Res. Oceans*, **20**, 4306 – 4323, doi:10.1002/2014JC010649.

Shadden, S. C., F. Lekien, and J. E. Marsden, 2005: Definition and properties of Lagrangian Coherent structures from finite-time Lyapunov exponents in two-dimensional aperiodic flows. *Physica D*, **212**, 271–304.

Shcherbina, A., and Coauthors, 2015: The Latmix Summer Campaign: Submesoscale Stirring in the Upper Ocean. *Bull. Amer. Meteor. Soc.*, **96**, 1257 – 1279, doi:10.1175/BAMS-D-14-00015.1.

Smith, K. S., and R. Ferrari, 2009: The Production and Dissipation of Compensated Thermohaline Variance by Mesoscale Stirring. *J. Phys. Oceanogr.*, **39**, 2477 – 2501.

Smith, W. H. F., and D. T. Sandwell, 1997: Global sea floor topography from satellite altimetry and ship depth soundings. *Sci.*, **277**, 1956 – 1962.

Spall, M. A., 1995: Frontogenesis, subduction, and cross-front exchange at upper ocean fronts. *J. Geophys. Res.*, **100**, 2543 – 2557.

Stommel, H., 1958a: The abyssal circulation. *Deep-Sea Res.*, **5**, 80 – 82.

Stommel, H., 1958b: *The Gulf Stream: A Physical and Dynamical Description*. 1st ed., 202 pp, University of California Press, Berkeley, Cambridge University Press, London.

Stone, P. H., 1966: On Non-Geostrophic Baroclinic Stability. *J. Atmos. Sci.*, **23**, 390 – 400.

Sulman, M. H. M., H. S. Huntley, B. L. L. Jr, and A. D. K. Jr, 2013: Leaving flatland: Diagnostics for Lagrangian coherent structures in three-dimensional flows. *Physica D*, **258**, 77–92.

Szezech, J. D. J., S. R. Lopes, and R. L. Viana, 2005: Finite-time Lyapunov spectrum for chaotic orbits of non-integrable Hamiltonian systems. *Phys Lett. A*, **335**, 394 – 401.

Tandon, A., and C. Garrett, 1994: Mixed Layer Restratification due to a Horizontal Density Gradient. *J. Phys. Oceanogr.*, **24**, 1419 – 1424.

Tandon, A., and C. Garrett, 1995: Geostrophic Adjustment and Restratification of a Mixed Layer with Horizontal Gradients above a Stratified Layer. *J. Phys. Oceanogr.*, **25**, 2229 – 2241.

Taylor, J. R., and R. Ferrari, 2009: On the equillibration of a symmetrically unstable front via a secondary shear instability. *J. Fluid Mech.*, **622**, 103 – 113.

Thomas, L., and C. Lee, 2005: Intensification of ocean fronts by down-front winds. *J. Phys. Oceanogr.*, **35**, 1086 – 1102.

Thomas, L. N., and T. M. Joyce, 2010: Subduction in the northern and southern flanks of the Gulf Stream. *J. Phys. Oceanogr.*, **40**, 429–438.

Thomas, L. N., A. Tandon, and A. Mahadevan, 2008: Submesoscale Processes and Dynamics. *Ocean Modell.*, **177**, 17 –38.

Thomas, L. N., J. R. Taylor, R. Ferrari, and T. M. Joyce, 2013a: Symmetric instability in the Gulf Stream. *Deep-Sea Res. II*, **91**, 96–110.

Thomas, L. N., J. R. Taylor, R. Ferrari, and T. M. Joyce, 2013b: Symmetric instability in the Gulf Stream. *Deep-Sea Res. II*, **91**, 96 – 110.

Thompson, A., A. Lazar, C. Buckingham, A. Naveira-Garabato, G. Damerell, and K. Heywood, 2016: Open-ocean submesoscale motions: A full seasonal cycle of mixed layer instabilities from gliders. *J. Phys. Oceanogr.*, In press, doi:10.1175/JPO-D-15-0170.1.

Truesdell, C., and W. Noll, 2004: *The Non-linear field theories of Mechanics*. NewYork: Springer.

Van Roekel, L. P., B. Fox-Kemper, P. P. Sullivan, P. E. Hamlington, and S. R. Haney, 2012: The form and orientation of langmuir cells for misaligned winds and waves. *J. Geophys. Res.*, **117**, C05 001.

Voth, G. A., G. Haller, and J. P. Gollub, 2002: Experimental Measurements of Stretching Fields in Fluid Mixing. *Phys. Rev. Lett.*, **88**, 254 501.

Waugh, D. W., and E. R. Abraham, 2008: Stirring in the global surface ocean. *Geophys. Res. Lett.*, **35**, L20 605.

Waugh, D. W., S. R. Keating, and M. Chen, 2012: Diagnosing Ocean Stirring: Comaparison of Relative Dispersion and Finite-Time Lyapunov Exponents. *J. Phys. Oceanogr.*, **42**, 1173–1185.

Weiss, J., 1991: The Dynamics of Enstrophy transfer in two-dimensional hydrodynamics. *Physica D*, **48**, 273 – 294.

Wiggins, S., 2005: The Dynamical Systems Approach To Lagrangian Transport in Oceanic Flows. *Ann. Rev. Fluid Mech.*, **37**, 295 – 328.

Young, W. R., 1994: The subinertial mixed layer approximation. *J. Phys. Oceanogr.*, **24**, 1812 – 1826.

Acknowledgments

I am grateful to the Almighty God for the grace He has granted me in the last three years. I have gone through the entire PhD time without any major health problems. Indeed, it has not been by power nor might but by the grace of God. In the moments when I felt down, I was comforted by the assurance that I have in Christ Jesus. What began as a little grasp of hope that I would once again get back to school in 2011, has indeed come to fulfilment. For God who laid the seed in my innerman, am indeed grateful. It is nolonger just a mere scripture but a testimony too, that those who trust in the Lord are like Mount Zion that is never moved but persists forever.

Sincere gratitude to my supervisors: Prof. Dr. Gualtiero Badin and Dr. Nuno Serra who provided academic guidance and support during the course of the PhD. Thanks gentlemen for giving me the opportunity to do my PhD under your supervision. Am also grateful to Prof. Dr. Aicke Beckmann who acted as my PhD panel committee chair, and together with my supervisors constituted my panel committee that ensured that I complete my PhD on schedule. I also acknowledge the University of Hamburg's cluster of excellence, CliSap for financially supporting my PhD and the School of Integrated Climate System Sciences (SICSS) for all the support rendered to ensure an easy completion of this PhD.

I also extend my sincere thanks to my better half Annet Eva who has stood with me through thick and thin. The encouragement you gave me in July 2011 just three weeks after our wedding was quite life changing. I also extend thanks to my family members; Nalongo (my mother), brothers and sisters for the support and encouragement you have rendered to me during the last three years. For sure, your absence was such a huge void so hard to fill. Am grateful to my academic advisor and mentor, Dr. Tumps Winston Ireeta; It's really a pleasure to have met you. Thanks also to my friends in Hamburg who made life interesting and worth celebrating. Sylvia with whom we started at ICTP in Trieste, Angella Cheska - thanks for the support especially when I had just arrived in Hamburg, Jairo segura - a fellow PhD candidate in the SICSS school and Feifei Liu - my officemate from China with whom we shared so many experiences. Thanks also to Dr. Martin Scharffenberg for the regular help and light moments. It is a joy to have met you. Thanks also to members of the theoretical oceanography group: Philipp Jurgenowsky, manita chouksey and all the rest for your regular support and the conducive environment that you offered to me during the course of my PhD.

I wish to thank the directors of the Geophysical Fluid Dynamics (GFD) summer school of 2014 for giving me the opportunity to be one of the fellows that year. From the principle lectures offered by Professors Kerry Emanuel and Geoffrey Vallis to the research project, every moment was remarkable and unforgettable. Noteworthy to highlight is Prof. Gualtiero Badin - my PhD supervisor who informed me about the GFD program and recommended me for it. You provided the pastures in Hamburg and when you felt, there might be some more grass at Woods Hole, you sent me to devour it. Thanks Gualtiero. Thanks to Prof. Joseph Pedlosky of Woods Hole Oceanographic Institution who acted as my advisor during the summer school and also gave the academic direction of the project. The prompt email replies which had to be made at times late in the night or very early in the morning depicted such extremes of commitment and willingness to help me accomplish the project. Thanks a lot Joe.

Finally, I would like to acknowledge the much welcomed assistance and support offered by Professor Glenn Flierl of Massachussetts Institute of Technology who not only provided regular guidance during the course of the project but also helped in providing the numerical code used in the study. Glenn's regular explanations made such a huge impact toward a better understanding of the problem studied and in turn shaped the direction of the study. Equally important was the support and academic guidance given by Stephen Meacham throughout the study. Thanks so much for your effort in seeing this project come to its completion.

List of Publications and Submissions

Aus dieser Dissertation hervorgegangene Vorveröffentlichungen und Einsendungen

1. Mukiibi, D., G. Badin, and N. Serra, 2016b: Three dimensional chaotic advection by mixed layer baroclinic instabilities. *J. Phys. Oceanogr.*, **46**, 1509 - 1529, doi:10.1175/ JPO-D-15-0121.1.

2. Mukiibi, D., G. Badin, and N. Serra, 2016a: The seasonality of submesoscale turbu- lence deduced from finite time Lyapunov exponents. In preparation.

3. Mukiibi, D., 2014: A numerical study of the downstream development of a baroclinic instablity. *2014 GFD program*, Woods Hole Oceanographic Institution, Massachusetts,USA., Vol. Climate Physics and Dynamics, URL http://www.whoi.edu/ fileserver.do?id=217704&pt=2&p=224229.

Erklärung/Declaration

Hiermit erkläre ich an Eides statt, dass ich die vorliegende Dissertationsschrift selbst verfasst und keine anderen als die angegebenen Quellen und Hilfsmittel benutz habe.

I hereby declare, on oath, that I have written the present dissertation by my own and have not used other than the acknowledged resources and aids.

July 12, 2016	
....	....
Hamburg, den	Unterschrift